AN OPTIMIZED PLANT FOR A DISTRICT HEATING AND COOLING SYSTEM USING LOW-GRADE GEOTHERMAL FLUIDS

A Dissertation

by

JIAJUN LIAO

Submitted to the Office of Graduate and Professional Studies of
Texas A&M University
in partial fulfillment of the requirements for the degree of

DOCTOR OF PHILOSOPHY

Chair of Committee,	David E. Claridge
Committee Members,	Michael B. Pate
	Charles H. Culp
	Ruud Weijermars
Head of Department,	Andreas A. Polycarpou

December 2019

Major Subject: Mechanical Engineering

ABSTRACT

An optimized plant is developed for a district heating and cooling system using low-grade geothermal fluids from depleted hydrocarbon wells. The optimum geothermal fluid flowrate and temperature supplied to the surface end-use system are determined as 29 gpm and 191°F from inactive wells on the Texas A&M RELLIS Campus. The absorption chiller, the desiccant dehumidification, and geothermal district heating systems are modeled for cooling, dehumidification, and heating and simplified with relationships between the required geothermal fluid temperature and its output at different outside air conditions. The desiccant wheel dedicated outside air system with heat exchanger and condenser water cooling shows the ability to avoid the most cooling coil load and therefore is selected for the surface integrated system.

The surface end-use system modeling is developed by combining these three heat-operated system models with load profiles of typical campus buildings. The inlet temperature requirements and the maximum temperature drops of each system are studied, and possible system arrangements are investigated using the bin method. Both the site energy load to energy ratio (LER) and the cost LER are introduced and calculated. When the building loads are large and the integrated system operates at its full capacity, the optimized arrangement is with the desiccant dehumidification system and the geothermal district heating system operated in parallel. When the outside air temperature is lower than 75°F, the geothermal district heating system is operated; otherwise, the desiccant dehumidification system is operated. Its yearly total energy

output is 8,572 MMBtu with a total LER of 14.08 – 23.76, i.e. it requires 14-24 times fewer electric Btu than the energy output. When the integrated system matches the building loads well, the optimized arrangement is that the absorption chiller system and the geothermal district heating system are in parallel, and then in series with the desiccant dehumidification system. Its yearly total energy output is 3,264 MMBtu with a cooling LER of 4.72 – 7.89 and a heating LER of 4.25 – 7.24. Thus, all the integrated geothermal systems described above would have an operating energy use less than one-fourth that of a traditional heating and cooling plant meeting the same loads.

DEDICATION

I dedicate this work to my research advisor Dr. David E. Claridge for exploring technology development, and to my direct family Shenghu Liao, Juzhen Gu, Lijun Liao, and Zhujun Liao for supporting my engineering career and aspirations.

ACKNOWLEDGEMENTS

I would like to thank my committee chair, Dr. Claridge, and my committee members, Dr. Pate, Dr. Culp, and Dr. Weijermars for their guidance and support throughout the course of this research.

I acknowledge Dr. Ibere Nascentes Alves, Dr. Lihua Zuo, and Mr. Sriniketh Sukumar for the help on the well pumping system analysis, Dr. Juan-Carlos Baltazar, Dr. Xiaoli Li, and Hongxiang (Casper) Fu for providing campus building consumption data and the Emodel tool, Dr. Yintao Wang for the help on the retrofit cost analysis of the multiple pump sizes with VFDs system, Dr. Wang Lei and Dr. Wei-Jen Chen for sharing excellent research ideas, Dr. Joan Carles Bruno Argilaguet for providing the absorption chiller experimental data, Miss. Hala Nemer for providing the cooling tower configurations, and Dr. Ying Li and Ms. Sandy Havens of the Texas A&M University Department of Mechanical Engineering for reviewing my submissions.

Special thanks to Mr. Carlos Yagua for supporting me on my research and lab duties. Thanks also go to everyone in the Energy Systems Laboratory for being helpful and fun.

Finally, thanks to my parents, Shenghu Liao, Juzhen Gu, my sisters, Lijun Liao, Zhujun Liao, and my girlfriend, Xiao Yu, for their encouragement and love.

CONTRIBUTORS AND FUNDING SOURCES

This work was supervised by a dissertation committee consisting of Professors David E. Claridge and Michael B. Pate of the Department of Mechanical Engineering, Professor Charles H. Culp of the Department of Architecture, and Professor Ruud Weijermars of the Department of Petroleum Engineering.

The research on the inactive well on Texas A&M RELLIS Campus introduced in Chapter I was conducted by Ruud Weijermars of the Department of Petroleum Engineering and was published in 2018.

All other work conducted for this dissertation was completed by the student independently.

As a part of the Energy Systems and Services division of the Texas A&M Engineering Experiment Station (TEES), the Energy Systems Laboratory paid for my graduate tuition and fees since 2015 as a graduate research assistantship.

NOMENCLATURE

A	Area
A/C	Air Conditioning
ABS	Absorption Chiller System
AFUE	Annual Fuel Utilization Efficiency
AHU	Air Handling Unit
ANN	Artificial Neural Network
ANSI/HI	The American National Standards Institute / The Hydraulic Institute
ASHRAE	The American Society of Heating, Refrigerating and Air-Conditioning Engineers
Btu	British Thermal Unit
c_P	Isobaric Specific Heat
c_V	Isochoric Specific Heat
CAV	Constant Air Volume
CHW	Chilled Water
COP	Coefficient of Performance
CPD	Cooling Power Density
CW	Condenser Water
CWST	Condenser Water Supply Temperature
DEC	Direct Evaporative Cooler
DEH	Desiccant Wheel Dehumidification System
DW	Desiccant Wheel

E	Energy Input
EA	Exhaust Air
EDE	Energy Delivery Efficiency
EEIB	Energy Efficiency Index for Buildings
EER	Energy Efficiency Ratio
EIA	Energy Information Administration
ERV	Energy Recovery Ventilation
EUI	Energy Use Intensity
g	Acceleration due to Gravity
GDHS	Geothermal District Heating System
GHP	Geothermal Heat Pump
gpm	Gallon per Minute
h	Enthalpy
HHW	Heating Hot Water
HID	Heating Input Density
HSPF	Heating Seasonal Performance Factor
HVAC	Heating, Ventilation, and Air Conditioning
HvacPD	HVAC Power Density
HW	Hot Water
HWRT	Hot Water Return Temperature
HWST	Hot Water Supply Temperature
HX	Heat Exchanger

IEC	Indirect Evaporative Cooler
IPLV	Integrated Part-Load Value
k	Thermal Conductivity
lbm	Pound mass
LDAC	Liquid-Desiccant Air-Conditioning
LER	Load/Energy Ratio
MA	Mixed Air
MBE	Mean Bias Error
MEI	Multizone Efficiency Index
N, #	Number
NPV	Net Present Value
O&M	Operation & Maintenance
OA	Outside Air
OAHU	Outside Air Handling Unit
OAT	Outside Air Temperature
ORC	Organic Rankine Cycle
p	Pressure
p_{ws}	Saturation Pressure
PHE	Plate Heat Exchanger
PLR	Part Load Ratio
psia	Pounds per Square Inch
Q, q	Energy or Load

R	Thermal Resistance
r	Radius
RA	Return Air
RMSE	Root Mean Square Error
SA	Supply Air
SCOP	System Coefficient of Performance
SDVAV	Single Duct Variable Air Volume
SEER	Seasonal Energy Efficiency Rating
SHE	Sensible Heat Exchange
SP	Setpoint
SPR	System Performance Ratio
T	Temperature
t	Time
Texas A&M	Texas Agricultural and Mechanical
T_{wb}	Wet Bulb Temperature
V	Flow Rate
VAV	Variable Air Volume
VFD	Variable Frequency Drive
w	Humidity Ratio
z	Depth
$°F$	Fahrenheit Degree
$°C$	Celsius Degree

η	Efficiency
ε	Effectiveness
ρ	Density
γ_w	Specific Gravity
Σ	Sum

TABLE OF CONTENTS

Page

ABSTRACT ii

DEDICATION iv

ACKNOWLEDGEMENTS v

CONTRIBUTORS AND FUNDING SOURCES vi

NOMENCLATURE vii

TABLE OF CONTENTS xii

LIST OF FIGURES xv

LIST OF TABLES xix

CHAPTER I INTRODUCTION 1

1.1 Research Background on Direct Use of Geothermal Fluid Energy 1
1.2 Initial Assessment on Inactive Wells on Texas A&M RELLIS Campus 3

CHAPTER II PURPOSE AND OBJECTIVES 7

CHAPTER III LITERATURE REVIEW 9

3.1 Geothermal Energy System and Components 9
3.1.1 Geothermal Energy Utilization 9
3.1.2 Absorption Chillers 11
3.1.3 Geothermal Organic Rankine Cycle 13
3.1.4 Geothermal District Heating System 15
3.2 Desiccant Wheel Application and Development 18
3.2.1 Desiccant Wheel 18
3.2.2 Low-Flow Liquid Desiccant 20
3.3 Multiple Pump Sizes with VFDs 21
3.4 HVAC System Load/Energy Ratio 23

CHAPTER IV SYSTEM MODELING AND OPTIMIZATION 30

4.1 Thermal Fluid Properties from the Subsurface System 36

4.1.1 Well Pumping System Analysis 39
4.1.2 Fluid Heat Loss Analysis 43
4.1.3 Energy Performance of the Well Pumping System 50
4.1.4 Geothermal Fluid Flowrate Variation Analysis 52
4.2 Separate Models for Heat-Operated Units 54
4.2.1 Absorption Chiller Model with Hot Water Fired Generator 54
4.2.2 Geothermal District Heating Model 59
4.3 Desiccant Wheel Model Development 61
4.3.1 Desiccant Wheel with Evaporative Cooling 61
4.3.2 Desiccant Wheel with Heat Recovery 68
4.3.3 Desiccant Wheel with CW Cooling 73
4.3.4 Optimized Desiccant Wheel Configuration 79
4.3.5 Case Study – GSC Building 82
4.4 Multiple Pump Sizes with VFDs Analysis 89
4.4.1 Multiple Pump Sizes with VFDs Configuration 89
4.4.2 Case Study – TSC Building 91
4.4.3 Case Study – VA-Brooklyn 100
4.5 System Units Arrangement Optimization 107
4.5.1 System Parameters and Possible Arrangements 107
4.5.2 Simulated Load Profile by Outside Air Temperature 112
4.5.3 System Performance Analysis and Arrangement Optimization 118
4.6 LER Analysis and Comparison 133

CHAPTER V CONCLUSIONS AND DISCUSSION 141

REFERENCES 144

APPENDIX A HOT WATER PIPELINE HEAT LOSS CALCULATION 162

A.1 Pipe Sizing 162
A.2 Pipe Insulation 162
A.3 Trench Thermal Resistance 163
A.4 Distribution Heat Loss 165

APPENDIX B MATLAB CODE 166

B.1 Well Pipeline Heat Transfer 166
B.2 Desiccant Wheel with IEC-DEC 168
B.3 Desiccant Wheel with HX 172
B.3.1 Code for AHU Configuration 172
B.3.2 Code for DOAS Configuration 176
B.4 Desiccant Wheel with CW Cooling 179
B.5 Desiccant Wheel with HX and CW Cooling 182

APPENDIX C ABSORPTION CHILLER OPERATIONAL DATA UNDER DIFFERENT TEMPERATURE CONDITIONS.....187

LIST OF FIGURES

Page

Figure 1. Proximity of peripheral oil wells to RELLIS infrastructure development. Reprinted from Economic appraisal and scoping of geothermal energy extraction projects using depleted hydrocarbon wells, by D. Westphal and R. Weijermars, 2018, Energy Strategy Reviews, Copyright 2018 by Elsevier [4].....3

Figure 2. Schematic of a sample geothermal circulation system and surface facilities. Reprinted from Economic appraisal and scoping of geothermal energy extraction projects using depleted hydrocarbon wells, by D. Westphal and R. Weijermars, 2018, Energy Strategy Reviews, Copyright 2018 by Elsevier [4].....6

Figure 3. Flow schematic of a geothermal organic rankine cycle.....14

Figure 4. Flow schematic of a typical geothermal district heating system. 16

Figure 5. Typical desiccant wheel HVAC applications. 19

Figure 6. Configuration of a desiccant wheel in the Jurinak model.....20

Figure 7. System diagram of a low-flow LDAC. 21

Figure 8. An example of a cascaded flow path with all three systems (see case G in Table 3). Reprinted from Redeveloping depleted hydrocarbon wells in an enhanced geothermal system (EGS) for a university campus: Progress report of a real-asset-based feasibility study, by R. Weijermars, D. Burnett, D. Claridge, S. Noynaert, M. Pate, D. Westphal, W. Yu, L. Zuo, 2018, Energy Strategy Reviews, Copyright 2018 by Elsevier [5].....31

Figure 9. An overview map for well pads on Texas A&M RELLIS Campus. Reprinted from Redeveloping depleted hydrocarbon wells in an enhanced geothermal system (EGS) for a university campus: Progress report of a real-asset-based feasibility study, by R. Weijermars, D. Burnett, D. Claridge, S. Noynaert, M. Pate, D. Westphal, W. Yu, L. Zuo, 2018, Energy Strategy Reviews, Copyright 2018 by Elsevier [5].....37

Figure 10. Development options a-d of Riverside #2 and #5 wells as a geothermal doublet. Reprinted from Redeveloping depleted hydrocarbon wells in an enhanced geothermal system (EGS) for a university campus: Progress report of a real-asset-based feasibility study, by R. Weijermars, D. Burnett,

D. Claridge, S. Noynaert, M. Pate, D. Westphal, W. Yu, L. Zuo, 2018, Energy Strategy Reviews, Copyright 2018 by Elsevier [5]. 38

Figure 11. A site visit on all well pad on Texas A&M RELLIS Campus. 39

Figure 12. Well pumping system diagram for pressure analysis. 40

Figure 13. Conduction through circular well steel tube. 44

Figure 14. The local geothermal gradient for those two inactive wells (Riverside #2 and #5). Reprinted from Redeveloping depleted hydrocarbon wells in an enhanced geothermal system (EGS) for a university campus: Progress report of a real-asset-based feasibility study, by R. Weijermars, D. Burnett, D. Claridge, S. Noynaert, M. Pate, D. Westphal, W. Yu, L. Zuo, 2018, Energy Strategy Reviews, Copyright 2018 by Elsevier [5]. 46

Figure 15. Schematic diagram of heat transfer performance analysis. 47

Figure 16. Thickness of insulation layer versus the geothermal fluid temperature. 50

Figure 17. LER values and geothermal energy outputs at different geothermal fluid flowrate. 53

Figure 18. Flow schematic of an absorption chiller with hot water heat source. 55

Figure 19. COP of case study absorption chiller at different part load ratios. 58

Figure 20. Flow schematic of the GDHS system. 59

Figure 21. GDHS hot water supply temperature reset. 60

Figure 22. Flow schematic of an open loop desiccant cooling system with IEC-DEC. .. 62

Figure 23. Performance example: desiccant wheel cooling system with IEC-DEC 67

Figure 24. Flow schematic of an open loop desiccant cooling system with IEC only. 68

Figure 25. Flow schematic of an open loop desiccant cooling system with heat exchanger and chilled water cooling coil. 69

Figure 26. Flow schematic of an open loop desiccant DOAS with HX. 71

Figure 27. Performance example: desiccant DOAS with HX. 73

Figure 28. Flow schematic of an open loop desiccant DOAS with CW coil. 74

Figure 29. Performance example: desiccant DOAS with CW coil. 78

Figure 30. Flow schematic of an open loop desiccant DOAS with both HX coil and CW coil. 79

Figure 31. Performance example: desiccant DOAS with HX and CW coil. 82

Figure 32. Picture of GSC Building located in College Station, TX. 82

Figure 33. An OAHU schematic diagram from the building automation system. 86

Figure 34. Pump VFD curve of part load power ratio versus flow ratio. 89

Figure 35. Flow schematic of the multiple pump sizes with VFDs configuration. 90

Figure 36. Picture of TSC Building located in College Station, TX. 91

Figure 37. TSC Building CHW pump power hourly pumping power distribution. 95

Figure 38. TSC Building CHW pump power and energy distribution statistical analysis. 96

Figure 39. TSC Building HHW pump power hourly value distribution. 96

Figure 40. TSC Building HHW pump power distribution statistical analysis. 97

Figure 41. Multiple HHW pump sizes with VFD that can cover lower flows. 98

Figure 42. Picture of VA-Brooklyn Building in New York City, NY. 101

Figure 43. VA-Brooklyn Building CHW pump power hourly pumping power distribution. 103

Figure 44. VA-Brooklyn Building CHW pump power and energy distribution statistical analysis. 104

Figure 45. VA-Brooklyn Building HHW pump power hourly value distribution. 104

Figure 46. VA-Brooklyn Building HHW pump power distribution statistical analysis. 105

Figure 47. Simplified DEH system diagram. 108

Figure 48. Case F - a typical arrangement of a cascaded flow path with all three systems. 112

Figure 49. 4P model for daily CHW consumption of the GSC Building cooling load. . 115

Figure 50. 4P model for daily HHW consumption of the GSC Building heating load..115

Figure 51. Optimized arrangement of a cascaded flow path when systems run at their full capacity. 125

Figure 52. The cascaded flow path of case E arrangement. 126

Figure 53. The cascaded flow path of case G arrangement.....132

Figure 54. Two pipes in buried trenches. 164

LIST OF TABLES

Page

Table 1. Consumption of thermal energy for heating and cooling for three building types. Reprinted from Redeveloping depleted hydrocarbon wells in an enhanced geothermal system (EGS) for a university campus: Progress report of a real-asset-based feasibility study, by R. Weijermars, D. Burnett, D. Claridge, S. Noynaert, M. Pate, D. Westphal, W. Yu, L. Zuo, 2018, Energy Strategy Reviews, Copyright 2018 by Elsevier [5]. 4

Table 2. Space conditioning capacity estimates. Reprinted from Redeveloping depleted hydrocarbon wells in an enhanced geothermal system (EGS) for a university campus: Progress report of a real-asset-based feasibility study, by R. Weijermars, D. Burnett, D. Claridge, S. Noynaert, M. Pate, D. Westphal, W. Yu, L. Zuo, 2018, Energy Strategy Reviews, Copyright 2018 by Elsevier [5]. 5

Table 3. Combinations of series cascade and parallel arrangements for heat-operated systems. Reprinted from Redeveloping depleted hydrocarbon wells in an enhanced geothermal system (EGS) for a university campus: Progress report of a real-asset-based feasibility study, by R. Weijermars, D. Burnett, D. Claridge, S. Noynaert, M. Pate, D. Westphal, W. Yu, L. Zuo, 2018, Energy Strategy Reviews, Copyright 2018 by Elsevier [5]. 34

Table 4. Heat transfer performance by various insulation layer thicknesses. 49

Table 5. LER values at different geothermal fluid flowrate. 53

Table 6. MATLAB results for the desiccant wheel with IEC-DEC. 66

Table 7. MATLAB results for the desiccant wheel with heat recovery. 70

Table 8. MATLAB results for DOAS system with desiccant wheel and heat recovery. . 72

Table 9. Cooling tower operating data from Texas A&M chiller plant. 75

Table 10. MATLAB results for the desiccant wheel with CW cooling coil. 77

Table 11. MATLAB results for the desiccant wheel with HX and CW coil. 81

Table 12. Energy rates from TAMU Utilities and Energy Services website for TSC Building. 84

Table 13. Measured heating, cooling, and electrical energy used by GSC Building. 85

Table 14. Monthly energy consumption and comparison based on the hourly analysis results. 87

Table 15. TSC Building HVAC equipment summary. 92

Table 16. Number of hours when pumps are running at minimum power in TSC Building. 94

Table 17. Energy and cost saving results for the multiple pump size system in TSC Building. 98

Table 18. Total installation cost of a 1.5 hp CHW pump and 1 hp HHW pump in TSC Building. 99

Table 19. Simple payback periods for multiple pump size system upgrades in TSC Building. 100

Table 20. Electricity rate for VA-Brooklyn Building. 101

Table 21. VA-Brooklyn Building HVAC equipment summary. 102

Table 22. Number of hours when pumps are running at minimum power in VA-Brooklyn Building. 102

Table 23. Energy and cost saving results for the multiple pump size system in VA-Brooklyn Building. 105

Table 24. Simple payback periods for multiple pump size system upgrades in VA-Brooklyn Building. 106

Table 25. Geothermal fluid supply temperature requirements by each system. 110

Table 26. Systems PLR and COP under different outside air conditions. 117

Table 27. Geothermal fluid temperature difference between supply and return in the DEH system. 121

Table 28. Geothermal fluid temperature difference between supply and return in the GDHS system. 122

Table 29. Geothermal fluid temperature analysis when the integrated system runs at full capacity. 124

Table 30. Bin analysis on ratios of the cooling load avoided by the DEH system to the cooling load remaining. 127

Table 31. Geothermal fluid temperature analysis for case E with variable geothermal flowrate to each system. 130

Table 32. The DEH system capacity comparison between case F and case G. 133

Table 33. LER values for buildings served by the integrated geothermal system and traditional plants. 139

Table 34. Summary of the operation for absorption chiller Pink chilli 12 under different temperature conditions. 187

CHAPTER I

INTRODUCTION

There are approximately 300,000 inactive oil and gas wells in the US, which may be reused to produce a significant amount of hot water suitable for geothermal direct use systems [1]. The largest hurdle for any geothermal project, the cost of drilling the well, would be significantly reduced when reusing existing wells. Drilling costs account for 43% to 95% of a total enhanced geothermal system power plant cost [2]. Since the only capital cost for these wells is the cost of refurbishing the well, geothermal projects using these wells could be very economically feasible. The reuse of these inactive hydrocarbon wells could provide the benefits of extending well life, delaying abandonment cost for the well owner, and turning the wells into green geothermal energy supply sources that reduce the carbon footprint [3].

1.1 Research Background on Direct Use of Geothermal Fluid Energy

Current research on geothermal fluid energy for direct use in building applications mainly focuses on space heating or district heating systems. We here evaluate an integrated system which can provide both cooling and heating to cover building loads comprehensively. In the system evaluated, the hot fluid from inactive wells is used via an intermediate loop with a separate fluid system to:

1. Cool buildings with an absorption chiller system (ABS),

2. Dehumidify outdoor air with a desiccant wheel dehumidification system (DEH),
3. Produce electrical/mechanical power with an organic rankine cycle (ORC),
4. Operate a geothermal district heating system (GDHS).

The individual units (pumps, absorption chillers, desiccant wheels, etc.) represent examples of currently available technology. However, a direct use system powered with low-temperature geothermal energy has not been previously optimized in terms of both energy efficiency and an economic objective function.

This integrated system is analyzed for the Texas A&M RELLIS Campus with six inactive wells as a case study, as shown in Figure 1. The whole analysis process is based on modeling and simulation since no funding is currently available for field measurements and experiments.

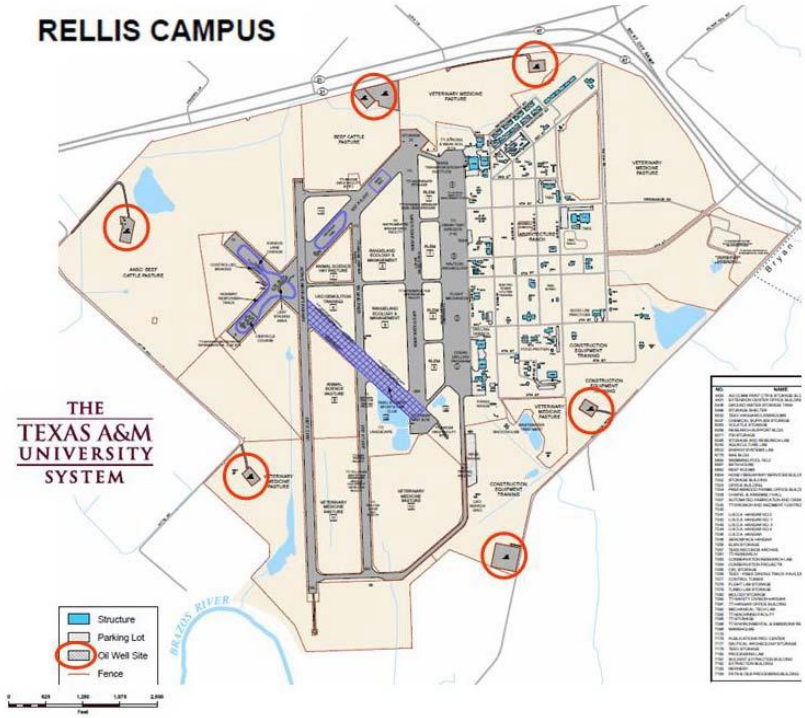

Figure 1. Proximity of peripheral oil wells to RELLIS infrastructure development. Reprinted from Economic appraisal and scoping of geothermal energy extraction projects using depleted hydrocarbon wells, by D. Westphal and R. Weijermars, 2018, Energy Strategy Reviews, Copyright 2018 by Elsevier [4].

1.2 Initial Assessment on Inactive Wells on Texas A&M RELLIS Campus

An initial assessment suggests that the six wells are able to sustain a large-scale space conditioning end-use system [5]. Table 1 lists the thermal energy consumed by groups of Texas A&M Campus laboratory buildings, classrooms, and offices as measured by the campus Utilities and Energy Services Department.

Table 1. Consumption of thermal energy for heating and cooling for three building types. Reprinted from Redeveloping depleted hydrocarbon wells in an enhanced geothermal system (EGS) for a university campus: Progress report of a real-asset-based feasibility study, by R. Weijermars, D. Burnett, D. Claridge, S. Noynaert, M. Pate, D. Westphal, W. Yu, L. Zuo, 2018, Energy Strategy Reviews, Copyright 2018 by Elsevier [5].

Building Type	**# of Buildings**	**Total Area (ft^2)**	**Cooling ($kBtu/ft^2 \cdot year$)**	**Heating ($kBtu/ft^2 \cdot year$)**
Laboratories	10	1,251,645	241.1	104.5
Classroom	7	1,058,274	74.4	24.3
Office	7	537,683	50.6	15.6

An initial evaluation assumed that thermal energy from the wells is converted to cooling with an average efficiency of 0.6 and that heat from the wells is used directly to meet the heating needs of the buildings. The initial pair of wells with an average flow of 1,000 bbl/day (29.17 gpm) of hot water at 200°F could then supply the heating and cooling needs for the space specified in Table 2, using the amounts of thermal energy listed in Table 1. Table 2 includes the amount of space conditioned with water returned to the well at 150°F and 100°F. Based on these estimates, it appears that promoting the wider use of thousands of inactive US oil and gas wells for our proposed system can result in a significant amount of energy savings and emission reductions.

Table 2. Space conditioning capacity estimates. Reprinted from Redeveloping depleted hydrocarbon wells in an enhanced geothermal system (EGS) for a university campus: Progress report of a real-asset-based feasibility study, by R. Weijermars, D. Burnett, D. Claridge, S. Noynaert, M. Pate, D. Westphal, W. Yu, L. Zuo, 2018, Energy Strategy Reviews, Copyright 2018 by Elsevier [5].

Building Type	Area Supplied w/Return at 150°F (ft^2)	Area Supplied w/Return at 100°F (ft^2)
Laboratory	12,000	24,000
Classroom	41,000	82,000
Office	61,000	122,000

To meet the heating and cooling loads of buildings at Texas A&M RELLIS Campus, the configurations of both the components and the system will be modeled and optimized. A sample geothermal circulation system is shown in Figure 2. To evaluate its energy saving potential, the energy savings will be calculated by comparing this system to a traditional district cooling and heating system. In addition, economic analysis will be conducted to investigate its prospects for commercial application [4].

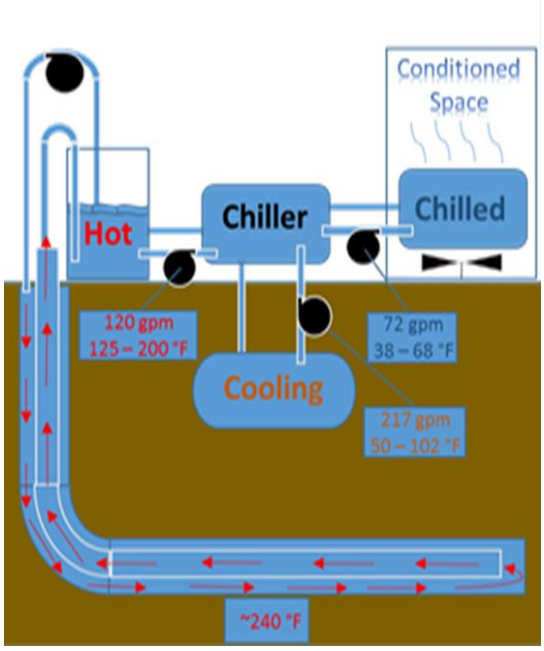

Figure 2. Schematic of a sample geothermal circulation system and surface facilities. Reprinted from Economic appraisal and scoping of geothermal energy extraction projects using depleted hydrocarbon wells, by D. Westphal and R. Weijermars, 2018, Energy Strategy Reviews, Copyright 2018 by Elsevier [4].

CHAPTER II

PURPOSE AND OBJECTIVES

The purpose of the research is to develop an economically optimum plant configuration for a district heating and cooling system using low-grade geothermal fluids. Specifically, we will investigate the energy and economic efficiency of an integrated and self-sufficient plant system that will optimize the use of low-grade geothermal energy from inactive oil and gas wells in providing heating and air conditioning to campuses by replacing the traditional chiller and boiler plant. This will be accomplished by tasks including (1) modeling separate units and the plant system, (2) analyzing the subsurface well pumping system, (3) optimizing the configuration and arrangement of the proposed system to meet a typical campus building cooling/heating load profile, (4) evaluating various applications of desiccant wheels in an air conditioning system, (5) applying multiple pump sizes system with VFDs in the building pumping system, (6) Comparing the new geothermal conditioning system with traditional plants using Load/Energy Ratio (LER) metrics.

The objectives of the proposed research are to:

1. Model the subsurface well pumping system and determine the geothermal fluid supplied flowrate and temperature.
2. Develop separate detailed models for absorption chillers, desiccant wheel systems, and a geothermal district heating system and then combine them to meet the typical campus building load profile;

3. Analyze the energy performance for possible unit arrangements and compare the system Load/Energy Ratio (LER) with traditional systems.

CHAPTER III

LITERATURE REVIEW*

The following literature review is organized into four separate areas of interest based on the various aspects of the research conducted:

1. Geothermal energy system and components;
2. Desiccant wheel application and development;
3. Multiple pump sizes with VFDs application;
4. HVAC system Load/Energy ratio.

3.1 Geothermal Energy System and Components

3.1.1 Geothermal Energy Utilization

Energy consumption has increased tremendously since the industrial revolution and will likely continue rising [6]. Consuming energy brings human beings serious problems like environmental harm and climate change [7]. Since the energy crisis, both academia and industry have dedicated great effort to searching for more reliable and clean energy sources and improving energy efficiency, especially renewable energy and energy-efficient technologies in building applications [8, 9]. Sustainable energy is essential and beneficial due to the positive impacts on the environment in comparison to

* Section 3.4 in this chapter is reprinted with permission from "Analysis of Whole-Building HVAC System Energy Efficiency" by J. Liao, D. Claridge, L. Wang, ASHRAE Transactions 124 (2018) 72-87, Copyright [2018] by ASHRAE. This paper was published in ASHRAE Transactions 124 (2018) Copyright 2018 ASHRAE. This paper may not be copied and/or distributed electronically or in paper form without permission of ASHRAE. For more information about ASHRAE Transactions, visit www.ashrae.org.

burning fossil fuels [10]. The Energy Information Administration (EIA) Monthly Energy Review indicates that U.S. renewables consumption in 2015 was 9.432 quadrillion Btu. Geothermal alone provided 0.226 quadrillion Btu, equivalent to the amount of energy in 10 million tons of coal and 2.39% of the total renewables consumption [11]. Geothermal has been widely applied as a sustainable solution since it is environmentally friendly, has reliable and secure availability, and is inexpensive compared to coal and natural gas [12].

The main uses of geothermal energy are for electric power generation, direct use, and the geothermal heat pumps (GHP) [13, 14]. GHP serves as one of the most efficient heating systems today using low-grade geothermal energy around 60°F [15, 16] while high-grade geothermal energy is harnessed to generate electricity by enhanced geothermal systems or binary cycle technologies [17, 18]. Various research projects and case studies demonstrate that direct use of geothermal energy is a versatile energy form with a wide range of applications, including agriculture, industry, buildings, etc. [19, 20] Especially in building applications, space heating usage in areas with cold climates accounts for more than 10% of all installed geothermal capacity in the world [19-22]. In addition, geothermal energy utilization impacts the environment much less than using conventional energy sources since the geothermal fluids used are reinjected underneath the ground [23].

Drilling cost has restricted geothermal exploitation and energy applications [24]. Meanwhile, thousands of gas and oil wells quit producing and are then abandoned; they are treated as a threat to the surrounding environment [25]. Thus, utilizing the inactive

gas and oil wells may both save energy and protect the environment if the feasibility of using geothermal low-temperature energy can be shown to be economically feasible [26-29].

3.1.2 Absorption Chillers

Conventional compression chillers are used in the vast majority of building cooling systems today. However, absorption chillers are used in a significant number of applications due to their ability to use waste heat and solar thermal energy [30]. They use heat sources including solar energy, direct-fired natural gas, industrial waste heat, and heat from the combined heat and power generation. Instead of using environmentally harmful fluids, they use a solution of lithium bromide–water or ammonia-water. Equipment on the market demonstrates that the electricity consumption of an absorption chiller can be less than 1% of its cooling capacity while conventional chillers consume a large amount of electricity to drive the compressors [31-33]. Wide utilization of absorption chillers with geothermal or solar energy may result in substantial electricity consumption decreases [34].

Performing an energy analysis of absorption chillers requires a numerical model to determine performance. Models are divided into two general categories: (1) physical thermodynamic models with complete input parameters [33, 35, 36]; and (2) empirical models with limited external parameters [37, 38]. An artificial neural network (ANN) model has also been proposed to predict the absorption chiller's performance [39, 40]. An ANN model for a solar-assisted air-conditioning system with hot water driven absorption chiller was built and a case study of estimated chiller capacity of 0 - 80 kW

was applied to demonstrate the model validity [41]. Although detailed models of indirect absorption chillers are available in the EnergyPlus engineering reference [42], this dissertation is not performing massive simulations where every property of every component is analyzed in great detail, and every possible absorption chiller performance variable is generated. Instead, it is attempting to capture the key performance features, e.g. the chiller COP and CHW output versus the external arithmetic mean temperature at major components [43]. The empirical model is adopted in this research since it requires fewer parameters and simpler computation. Kuhn and Ziegler's model [44] defines the adapted characteristic temperature difference model ($\Delta\Delta t'$) by the following arbitrary characteristic temperature function in Equation (1).

$$\Delta\Delta t' = t_{gen} - a \cdot t_{ac} + e \cdot t_{eva} \tag{1}$$

The linear characteristic equation for each energy component transferred is defined in Equation (2).

$$\dot{Q}_k = s' \cdot \Delta\Delta t' + r \tag{2}$$

Substituting the $\Delta\Delta t'$ expression into Equation (2), a simple linear model, shown in Equation (3), is obtained where the component thermal performance is a function of the external arithmetic mean temperature of the generator (t_{gen}), the absorber condenser (t_{ac}), and the evaporator (t_{eva}). The four coefficients a, e, s, and r are based on multiple linear regression fits which utilize experimental data or manufacturers' operational parameters.

$$\dot{Q}_k = s' \cdot t_{gen} - s' \cdot a \cdot t_{ac} + s' \cdot e \cdot t_{eva} + r \tag{3}$$

Based on a comparative evaluation of major absorption chiller models, $\Delta\Delta t'$ has similar performance prediction accuracy to ANN models but requires fewer inputs and less computational complexity [45]. The model coefficients are found using reliable experimental data from an absorption chiller with a capacity of 12 kW. Generally, the model is also reliable on larger capacity absorption chillers [46]. $\Delta\Delta t'$ model coefficients for different capacity levels are given for hot water fired H_2O/LiBr absorption chillers [46, 47].

3.1.3 Geothermal Organic Rankine Cycle

The Organic Rankine Cycle (ORC), also known as the Binary Rankine Cycle, enables the use of heat from low-temperature resources ranging from 170°F (76°C) to 240°F (115°C) to provide work. In this general process, geothermal fluid flows through a heat exchanger and heats the low boiling point working fluid. Then, the working fluid is vaporized and passed through a turbine to generate electricity. To complete the cycle, the working fluid is condensed and recycled to the evaporator [48], as shown in Figure 3. Among traditional geothermal power plants, ORC, as state-of-the-art technology, enables the utilization of low-temperature energy sources to produce electricity [49]. Along with the commercialization of the low-temperature ORC systems [50], various research studies demonstrated the successful application of ORC systems integrated with turbines [51-54] or large screw expanders [55-57] utilizing waste heat. Industrial market deployment has been found feasible and provided promise for large capacity geothermal ORC power generation [58]. The average heat-to-electricity energetic conversion efficiency for ORC grows approximately linearly from 0.06 to 0.09 when the geothermal

temperature increases from 185℉ (85℃) to 240℉ (116℃) [58, 59]. Small-scale ORCs have limited applications due to high initial cost and low electric efficiencies. Three detailed cases studies have been conducted to assess economic feasibility [60]. Results show that the internal rate of return is as low as 7% when the hot water flow is 120 GPM. The application of an ORC with an electric generation efficiency of 7% would require a chiller COP of 9 and a condenser temperature too low to meet building heating needs.

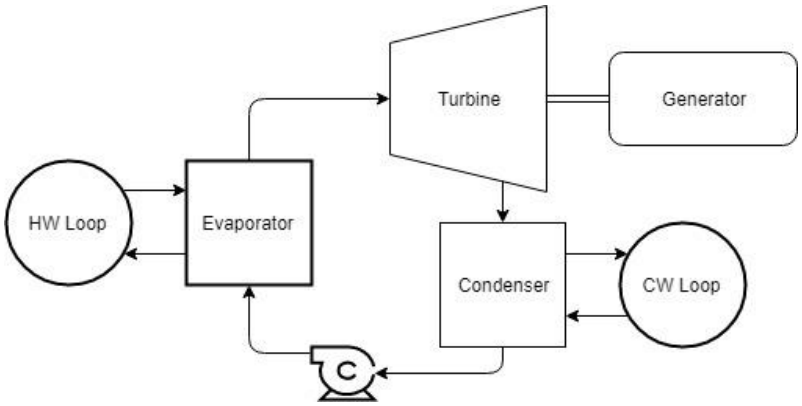

Figure 3. Flow schematic of a geothermal organic rankine cycle.

Also, a simple calculation is attached to demonstrate the exclusion of the ORC system. An ElectraTherm Power+ Generator 6500 is taken as an example [61]. The nominal rating is up to 110 kW and the design life is 20 years. The manufacturer's suggested retail price is $409,159 and the installation fee, including shipping, hookup, commissioning, and startup, etc., is $66,490. The O&M cost is around 2/3 of the total cost, i.e. two times the capital cost. It is assumed that the lifetime running hour

percentage is 90% and the lifetime average operating efficiency is 70%. Note that the hot water inlet temperature ranges from 170 to 252°F and the hot water flow range is 100 to 350 gpm for this equipment. Thus, the maximum lifetime electricity production = 110kW * 24hr * 365day/year * 20year * 90% * 70% = 12,141,360 kWh; total cost = capital cost + O&M cost = ($409,159 + $66,409) * (1+2) = $1,426,704; and the total cost per kWh per lifetime = $1,426,704 / 12,141,360 kWh = $0.118/kWh, which is significantly higher than the Texas A&M University Campus electricity rates of $0.082 / kW [62]. This rate has assumed a 0% discount rate and zero cost for recovery of the geothermal fluid. If a discount rate of 10% were added, the Net Present Value (NPV) of expenditures for 20 years of electricity purchase at current campus rate is $423,800 which is less than the installed cost of the ORC unit. The net present value of costs for the installed ORC unit plus the 20 years of maintenance is $880,400 which is more than two times the NPV of purchased electricity. At the same time, the maximum thermal input is 5.4 MMBtu/hr and the overall efficiency, the ratio of kW output to thermal input, is 110 kW / 5.4 MMBtu/hr = 0.0695, which is poor utilization of the geothermal energy compared to other applications evaluated in this dissertation. Hence the ORC application will not be considered further in the analysis of the integrated system.

3.1.4 Geothermal District Heating System

District heating systems have become popular in many countries over the past decades. For example, 46% of the net heat demand in Denmark is met by district heating systems [63]. Research has focused on every possible aspect to facilitate its applications in the real world, including implementation strategies to minimize the operational costs

[64-66], maximize the distance a district heating network can cover economically [67, 68], and exergy analysis of the system performance [69].

On the other hand, about 20% of geothermal energy is used for space heating in the world, of which 77% is for district heating [70]. A flow schematic of the simplified geothermal district heating system (GDHS) is illustrated in Figure 4. In a typical GDHS, the geothermal fluid (process 1-2) heats the distributed hot water (process 3-4) through a central heat exchanger, and then the distributed hot water heats the building hot water (process 5-6) for space heating and cooling through a substation heat exchanger.

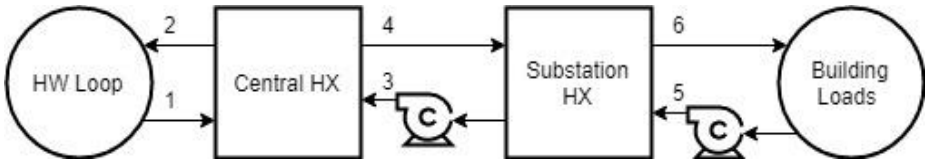

Figure 4. Flow schematic of a typical geothermal district heating system.

Today, the exergy-based method is often used to improve thermodynamic efficiency and reduce energy consumption and greenhouse gas emissions [71, 72]. The goal of this study is to maximize the energy utilization of the geothermal fluids given a flowrate. Thus, GDHS energy efficiency is one of the key parameters. The energy efficiency of the GDHS system (η_{GDHS}) can be defined, in Equation (4), as the ratio of the total energy output (the useful part) to the total energy input, where energy inputs include geothermal energy and pumping system. Considering the pipeline heat loss and heat exchanger efficiency, various case studies show the GDHS energy efficiency is between 0.4 and 0.55 with a reference outside air temperature of 39°F (4°C) [73]. Higher

ambient temperature (T_a) means less pipeline heat loss and higher energy efficiency. An empirical equation between η_{GDHS} and T_a is shown in Equation (5) for a demonstration [73]. However, this efficiency is calculated based on a distribution distance of 4.4 miles (7 km) and a total length of 16.7 miles (27 km) for both first and second distribution lines. In this analysis, the whole Texas A&M RELLIS Campus can be covered by a distribution distance of 1 mile (1.6 km) or less and the thermal efficiency would actually be much higher as shown subsequently.

$$\eta_{\mathrm{GDHS}} = \frac{\mathrm{E}_{\mathrm{output,\ useful}}}{\mathrm{E}_{\mathrm{input}}} \tag{4}$$

$$\eta_{\mathrm{GDHS}} = 2.1^{-5}\mathrm{T}_{\mathrm{a}}^{3} - 0.0029\mathrm{T}_{\mathrm{a}}^{2} + 0.3228\mathrm{T}_{\mathrm{a}} + 38.27 \tag{5}$$

According to the distribution system heat loss calculation in the 2016 ASHRAE Handbook – HVAC Systems and Equipment [74], the total heat loss is around 10 - 20 $\mathrm{Btu/hr \cdot ft}$ with polyurethane insulation and supply and return district heating hot water of 200°F and 160°F. The distribution heat loss would be around 50 - 100 kBtu/hr (see Appendix A), which takes less than 10% of the total thermal energy input. Since the total distribution heat loss depends on the two hot water temperatures, pipeline length, and many other factors, an average total distribution heat loss of 5% is assumed for the sake of simplicity based on the Texas A&M Campus plant operation experience.

Regarding the plate heat exchanger (PHE), the thermal efficiency can be 95% or higher since plates stacked on the top of each other allow virtually no room for any heat loss [75]. An average PHE energy efficiency of 97% is assumed across the analysis. The capacity of a PHE is determined by the heat transfer surface area, heat transfer

coefficient, and the mean temperature difference between the heat exchanger streams. The system will be optimized to meet the campus load.

3.2 Desiccant Wheel Application and Development

3.2.1 Desiccant Wheel

In traditional air handling units, the air dehumidification is accomplished by setting a low cooling coil leaving air temperature setpoint, which often causes a large amount of reheat energy consumption in terminal boxes and makes the whole HVAC system inefficient [76]. Desiccant wheels have been widely applied due to three main advantages [77]. First, they reduce reheat energy consumption. Secondly, they reduce the presence of microorganisms since the amount of condensed water from cooling coils is reduced or eliminated. Finally, they also reduce the required system cooling capacity.

There are two typical HVAC applications for desiccant wheels: (1) a desiccant wheel is located upstream of the cooling coil for dedicated outdoor air system application, (2) the desiccant wheel is located downstream of the cooling coil for space requirements of a low humidity level, as shown in Figure 5. Combining the use of a desiccant wheel with the utilization of geothermal hot water, the first application is selected for detailed analyses.

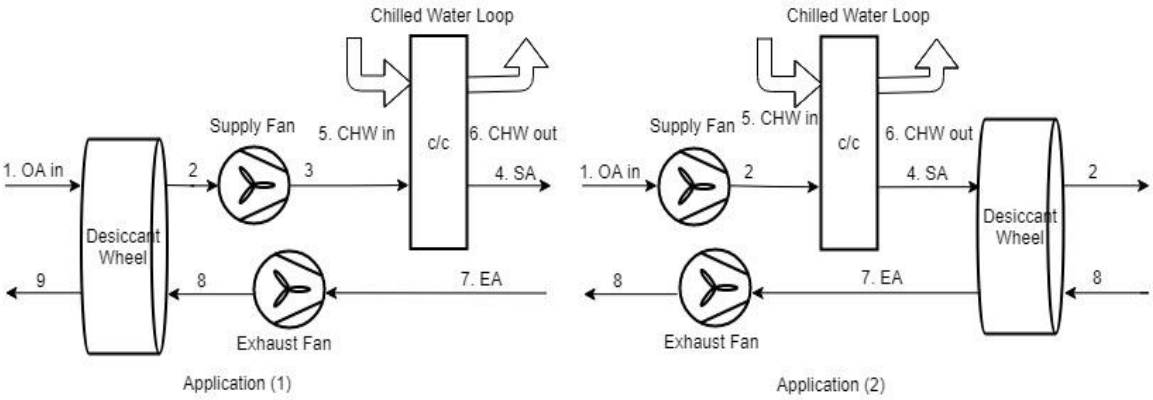

Figure 5. Typical desiccant wheel HVAC applications.

Performing an energy analysis of the desiccant wheel requires a complex modeling and simulation process. Some of the analyses assume a one-dimensional transient heat and mass transfer model, and this involves complicated partial differential equations for dynamic processes in the wheel [78, 79]. Other analyses adopt simplified empirical models with the steady-state assumption [80-82]. The transient-state models are comprehensive but too complex and difficult to solve. The steady-state models are simple and sufficient for the analysis purpose of our study. The Jurinak model [83] is selected and summarized as follows in Equations (6) to (9):

$$\eta_{f1} = \frac{f_{1so} - f_{1si}}{f_{1ei} - f_{1si}} \tag{6}$$

$$\eta_{f2} = \frac{f_{2so} - f_{2si}}{f_{2ei} - f_{2si}} \tag{7}$$

$$f_{1j} = -2865 T_j^{-1.49} + 4.344 \omega_j^{0.8624} \tag{8}$$

$$f_{2j} = T_j^{1.49}/6360 - 1.127 \omega_j^{0.07969} \tag{9}$$

The variables η_{f1} and $\eta_{f2}$are correlations based on a desiccant wheel's specifications, subscripts "s" and "e" denote supply and exhaust states, and "i" and "o" denote inlet and outlet states, as shown in Figure 6 below. T is temperature in K and ω is humidity ratio in kg water vapor/kg per dry air or lb water vapor/lb per dry air. At the optimum rotary speed, the effectiveness constants are $\eta_{f1} = 0.30$ and $\eta_{f2} = 0.85$.

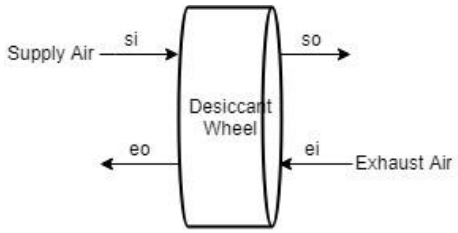

Figure 6. Configuration of a desiccant wheel in the Jurinak model.

Generally, the regeneration process of the desiccant wheel requires a temperature range of 113°F (45°C) to 194°F (90°C) [84]. Several studies confirm that operational experiences recommend a required temperature range of 140°F (60°C) to 158°F (70°C) [79, 82, 85, 86].

3.2.2 Low-Flow Liquid Desiccant

The liquid-desiccant air-conditioning (LDAC) system has been applied to remove both large latent loads from process air and various pollutants [87, 88]. The three main components of the LDAC system are the regenerator, the conditioner, and the interchange heat exchanger, shown in Figure 7. Although the low-flow LDAC is a new technology with several developed applications [89], the core principle is similar to the

desiccant wheel: desiccant in the conditioner absorbs the humidity in the processed air and then the humidity is extracted from the desiccant in the regenerator. However, a three-dimensional model, accounting for air flow, liquid desiccant, and coolant water, makes the dehumidification performance analysis even more complicated than the desiccant wheel models [90]. Studies have focused on mathematical simulation models to predict the dynamic flow parameters within the dehumidifier [90, 91]. In this study, we focus on desiccant wheel applications.

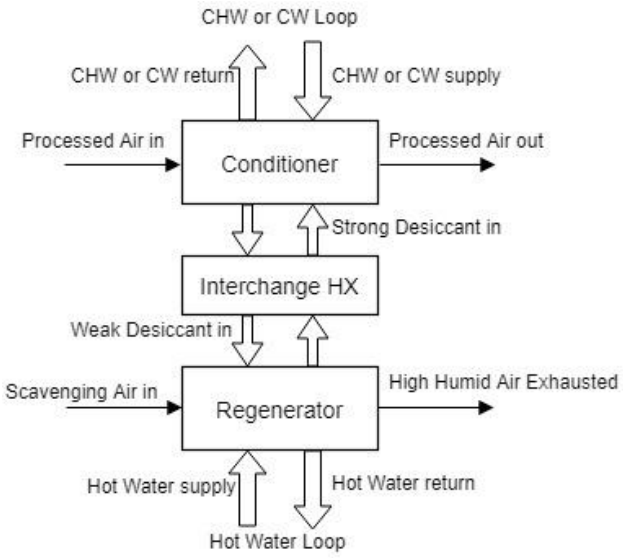

Figure 7. System diagram of a low-flow LDAC.

3.3 Multiple Pump Sizes with VFDs

Since electric motor-driven systems and components consume 24% of total commercial energy [92], even a small energy efficiency improvement may lead to significant energy savings [93]. In recent years, an increasing number of HVAC systems

use Variable Frequency Drives (VFDs), because the constant volume air system is extremely energy inefficient and consumes a large amount of reheat energy. Yao's case studies indicate the HVAC energy-saving rates of variable air volume systems range from 17% to 37.6% compared to a constant air volume system [94]. Similar energy savings are also demonstrated by other case studies [95]. Moreover, variable speed pump operation can save 20% to 50% of the pumping energy consumed, compared to a fixed-speed pump with control valves [96-98]. Installing a VFD on an existing constant speed pump has been a common practice as a building energy conservation measure [6]. Recently, studies have focused more on the design, regulation, and control optimization of pumps with a VFD in building HVAC systems [99-103].

However, limitations exist on pumps and VFDs, which make pumps with VFDs less efficient than expected. Although most standard motors can provide full torque output from 3 to 60 Hz, motors running at 30% or less of rated speed will often overheat and require supplemental cooling [104]. Pumps running at low speed also result in potential flow temperature rise, unstable operation, or flow recirculation within the impeller [104]. On the other hand, no published standards list precise limits for minimum flow in pumps, but "ANSI/HI 9.6.3 – 1997 Centrifugal and Vertical Pumps for Allowable Operating Region" recommends a preferred operating region with a minimum flow rate of 20% to 30% of the best efficiency point [105].

For buildings operating continuously with a significant variation of zone loads, a significant percentage of hours have low zone loads, especially at nights and on weekends. Chiller plants commonly install multiple chillers [106, 107] so that zones

with low loads are covered by a smaller chiller with higher efficiency. Since identical pumps with a VFD can only provide a chilled water (CHW)/heating hot water (HHW) flow rate down to about 30% of the rated pump flow rate, a similar approach can be applied with pumps. Pump energy can be saved if pumps run at lower power. It is worth pointing out that the simultaneous cooling and heating caused by pump minimum flow rate may be avoided by three-way valves at the coils or bypass valves in the pumping loop [108].

3.4 HVAC System Load/Energy Ratio

There are a number of efficiency measures related to building HVAC systems. Each measure has its own value for different users, which leads to different strengths and weaknesses. Common energy efficiency indexes such as Energy Efficiency Ratio (EER) [109], Seasonal Energy Efficiency Rating (SEER) [110], Integrated Part-Load Value (IPLV) [111], Annual Fuel Utilization Efficiency (AFUE) [112], and Heating Seasonal Performance Factor (HSPF) [113] are based on testing in a laboratory, which is different from normal operating conditions. The Coefficient of Performance (COP) [111] may incorporate all important system components in a small split-system air conditioner but is generally applied only to the chiller in a large building. Energy Use Intensity (EUI), being expressed as $kBtu/ft^2 \cdot year$ [$kWh/m^2 \cdot year$], is the preferred unit of analysis for commercial end-use demand forecasting to reflect the annual energy use and work as a type of energy benchmark to be widely used in building energy analysis. A whole building EUI can indicate the overall level of total building energy consumption, but it is

inadequate to understand the individual effect of building subsystems [114] and gives no indication of HVAC system efficiency.

For a geothermal space conditioning system, the system energy efficiency metric must include all the energy inputs, including all pumping work on the primary and secondary loop and the equipment electricity consumption. It should also reflect the advantage of the "free" geothermal energy and how well the integrated system meets the campus load profile. Thus, the whole-building cooling and heating efficiency measure, called the building systems load/energy ratio (LER) [115], will be used here. It has been expressed in terms of the different sources of energy (EBS) required to meet the corresponding positive or negative loads (QBSL) of the entire building as in Equation (10). Specifically, the building systems total load is composed of the envelope load, the load from internal gains, and the ventilation load on the secondary systems. The total energy input includes that to chillers, boilers, pumps, and fans on both the air-side and the water-side. LER makes the energy efficiency comparison possible for different complete HVAC systems along with different energy sources. Thus, the LER for the integrated system with a geothermal plant will be calculated and compared with traditional district heating and cooling system metrics.

$$\mathrm{LER} = \mathrm{Q_{BSL}}/\mathrm{E_{BS}} \tag{10}$$

Although traditional HVAC system energy efficiency indices focus on an air-side system or a single HVAC component, several system efficiency measures are found in the literature, some of which come relatively close to meeting the objectives of LER are described below.

HVAC Power Density (HvacPD) [116] is expressed in terms of power input per unit floor area for the entire HVAC system. The development process of HvacPD begins by computing the required design cooling (q_c) and heating (q_h) loads for a specific building. These values are divided by the system energy efficiency ratio (EER) for cooling called the cooling power density (CPD) and the thermal efficiency values for fossil fuel equipment (η_t) for heating called the heating input density (HID) to arrive at HvacPD values. The CPD presents the electrical demand requirement per unit area, including the input for all HVAC system components including the chillers, fans, and pumps as expressed in Equation (11).

$$\mathrm{CPD}[{}^{W_e}/_{ft^2}] = \frac{q_c}{A}[{}^{Btu}/_{h \cdot ft^2}] \div \mathrm{EER}[{}^{Btu}/_{W \cdot h}] \tag{11}$$

The HID expresses the heating requirement per unit floor area as expressed in Equation (12).

$$\mathrm{HID}[{}^{Btu}/_{h \cdot ft^2}] = \frac{q_h}{A} \div \eta_t \tag{12}$$

Once the building type and climate type are identified, HvacPD can be applied as an index to measure the HVAC system's peak energy demand for a complex building. It directly identifies the impact of all system components on the net energy efficiency of the building HVAC system at design conditions. However, since HvacPD is based on peak load, the impact of system controls, part load operation and similar factors are not reflected in this measure.

The System Performance Ratio (SPR) [117] is defined as the ratio of annual system load to the annual system energy consumption, similar to a whole system COP.

The cooling system performance ratio (C-SPR), heating system performance ratio (H-SPR), and total system performance ratio (T-SPR) are separately calculated to provide an independent evaluation of the cooling, heating and integrated HVAC systems. SPR provides a single evaluation criterion to address all of the HVAC system's components in a building, which includes mechanical ventilation, equipment full- and part-load performance and distribution system effectiveness.

$$\mathrm{SPR_{Heating}} = \frac{\text{Ideal annual heating load}}{\mathrm{E_{Heating}} + \mathrm{E_{Fan,Heating}} + \mathrm{E_{Pump,Heating}}} \tag{13}$$

$$\mathrm{SPR_{Cooling}} = \frac{\text{Ideal annual cooling load}}{\mathrm{E_{Cooling}} + \mathrm{E_{Fan,Cooling}} + \mathrm{E_{Pump,Cooling}} + \mathrm{E_{Heat,Rejection}}} \tag{14}$$

$$\mathrm{SPR_{Total}} = \frac{\text{Ideal annual heating load} + \text{Ideal annual cooling load}}{\mathrm{E_{Heating}} + \mathrm{E_{Cooling}} + \mathrm{E_{Fan}} + \mathrm{E_{Pump}} + \mathrm{E_{Heat,Rejection}}} \tag{15}$$

where the $\mathrm{E_{Heating}}$ is the heating coil energy use, $\mathrm{E_{Fan,Heating}}$ is the fan energy use during the heating mode, $\mathrm{E_{Pump,Heating}}$ is the pump energy use in the case of hydronic systems, $\mathrm{E_{Cooling}}$ is the cooling coil energy use, $\mathrm{E_{Fan,Cooling}}$ is the fan energy use during the cooling mode, $\mathrm{E_{Pump,Cooling}}$ is the pump energy use in the case of hydronic systems, and $\mathrm{E_{Heat,Rejection}}$ is the energy use for heat rejection in the cooling tower, 'Ideal annual heating load' and 'Ideal annual cooling load' are calculated using the special HVAC system type available in EnergyPlus called the Ideal Loads system. The SPR comes closer to meeting the objectives of LER than the HvacPD values but is defined only as a single annual average value. It also attributes all heating energy used to the heating load, even if there is no heating load present when the heat is actually

being used to avoid overcooling. Finally, it does not offer the option of treating the impact of different fuels on system efficiency in multiple ways.

The Multizone Efficiency Index (MEI) is calculated separately for heating and cooling: heating MEI is the ratio of the annual heating energy required by an ideal one-zone system to the observed annual heating energy, and cooling MEI is the ratio of the annual cooling energy required by an ideal one-zone system to the observed annual cooling energy. MEI focuses on the inefficiency caused by the simultaneous heating and cooling in different zones [118], but again uses an annual measure that attributes all heat to the heating load and cooling to the cooling load. The Energy Efficiency Index for Buildings (EEIB) is calculated as a ratio of the performance (in terms of energy consumption) of the actual building (AB) under certification or study, and that of a reference building (RB). Both RB and AB should belong to the same type of building and have the same floor space since the energy use of a building is significantly dependent on the function (residential, hospital, education, office). The energy consumption of the RB must represent a reference based on the energy use of the whole set of buildings of the same type. Thus, EEIB cannot present an absolute building systems efficiency value since it relies on the consumption of the reference building [119]. The EDE (Energy Delivery Efficiency) is calculated as the absolute value of measured thermodynamic minimum energy use (the difference between measured heating and cooling energy) divided by actual energy use. The EDE methodology pointed out that the one-zone model is an upper limit, and that the efficiency of a two-zone model, would constitute a more realistic energy standard to evaluate the efficiency

of actual HVAC systems. This mathematical treatment considered only sensible heat flows, but was expanded to cover supply air latent effects as well as the influence of economizer operation [120]. The EDE approach is intended for use as a diagnostic tool to evaluate HVAC retrofit performance and operation and maintenance measures. The EDE comes close to meeting the objectives of LER, but it includes only the thermal efficiency of the airside sub-system while the energy use of the water-side and the plant must also be considered in a measure of complete HVAC system efficiency [121].

Yan et al [122] proposed the system coefficient of performance (SCOP), which is an indicator to assess the overall energy efficiency of an HVAC system. SCOP is defined as the ratio between the total refrigerating loads to the total consumption of the HVAC system. And SCOP is also developed to cover the energy efficiency of both the HVAC system and individual components [123]. However, SCOP does not consider the heating system, and heating energy use impacts the efficiency of the entire HVAC system. Besides, the SCOP does not handle buildings with multiple energy sources.

LER is normally calculated using the entire building load and total energy input for each building. However, the campus buildings used for the case studies in this study are served by a central plant where it is impossible to separate the plant energy consumption used to supply a specific building. Hence the methodology will be adjusted for use with central plants.

When the building has cooling energy input, the chiller plant cooling energy input for each building will be obtained using the chiller plant average cooling energy/load ratio ($LER_{chiller}$), defined as the ratio of the total Chilled Water (CHW)

energy output to the total energy input in chiller plants shown in Equation (16). Chiller plant total energy input includes chiller ($E_{Chiller}$), cooling tower fan (E_{CTFan}), cooling tower condenser water pump (E_{CTPump}), and chilled water pump ($E_{CHWPump}$). And chiller plant output is CHW supplied to buildings (E_{CHW}).

$$LER_{chiller} = \frac{E_{CHW}}{E_{Chiller} + E_{CTFan} + E_{CTPump} + E_{CHWPump}} \quad (16)$$

When the building has heating energy input or uses reheat, the boiler plant heating energy input for each building will be obtained using the boiler plant average heating efficiency (LER_{Boiler}), defined as the ratio of the total Heating Hot Water (HHW) energy output to the total energy input in boiler plants as expressed in Equation (17). Boiler plant total energy cost input includes boiler (E_{Boiler}) and heating hot water pump ($E_{HHWPump}$). And the boiler plant output is HHW supplied to buildings (E_{HHW}).

$$LER_{Boiler} = \frac{E_{HHW}}{E_{Boiler} + E_{HHWPump}} \quad (17)$$

CHAPTER IV

SYSTEM MODELING AND OPTIMIZATION*

Three system categories (ABS, DEH, and GDHS) are commercially available to various degrees, but within a system category, units differ considerably in their applicability, size, performance, cost, and thermal fluid requirements (temperature), such that a detailed investigation and design analysis needs to be performed to determine their suitability for the project analyzed herein. Of special note is the fact that the three systems for cooling, dehumidification, and heating can be configured in any number of arrangements to optimize their efficiency for utilizing the thermal energy of the well fluid for useful purposes. One such example with all three systems operating in series can be seen in Figure 8, where the first system, namely the ABS, utilizes the hot test fluid and the last system shown, namely the GDHS utilizes the fluid containing the least thermal energy. Also, as shown in Figure 8, the intermediate flow loop isolates the end-use systems and equipment from the corrosive well-water. Finally, the major systems, shown in Figure 8, are for cooling and heating by means of water coils.

* The introduction part before section 4.1 is reprinted with permission from "Redeveloping depleted hydrocarbon wells in an enhanced geothermal system (EGS) for a university campus: Progress report of a real-asset-based feasibility study" by R. Weijermars, D. Burnett, D. Claridge, S. Noynaert, M. Pate, D. Westphal, W. Yu, L. Zuo, 208, Energy Strategy Reviews, 21 (2018) 191-203, Copyright [2018] by Elsevier. DOI: 10.1016/j.esr.2018.05.005

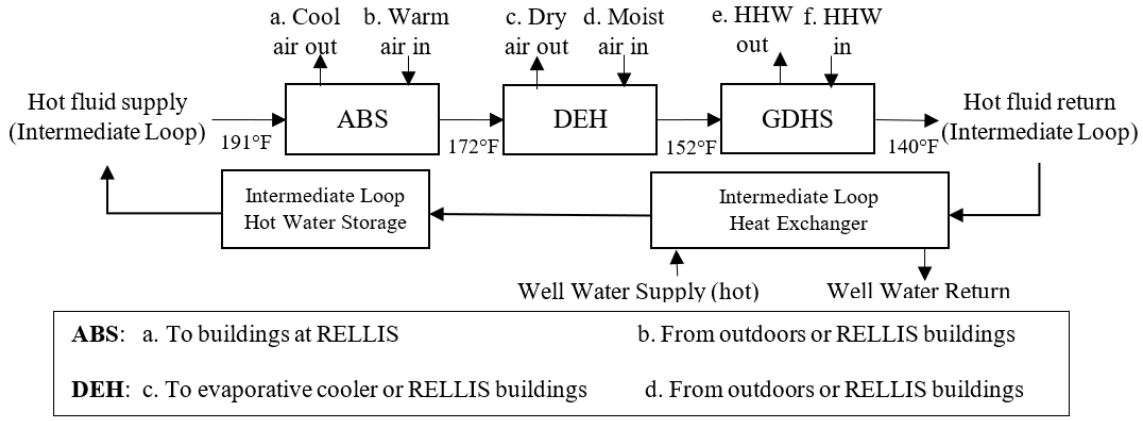

Figure 8. An example of a cascaded flow path with all three systems (see case G in Table 3). Reprinted from Redeveloping depleted hydrocarbon wells in an enhanced geothermal system (EGS) for a university campus: Progress report of a real-asset-based feasibility study, by R. Weijermars, D. Burnett, D. Claridge, S. Noynaert, M. Pate, D. Westphal, W. Yu, L. Zuo, 2018, Energy Strategy Reviews, Copyright 2018 by Elsevier [5].

As a first step in the surface-system design, a detailed survey of commercially available heat-operated units for each of three system categories is performed by focusing on applicability and the degree to which equipment specifications are given. This is essential for evaluating the systems suitable for our specialized application. Units that meet this criterion are categorized and classified according to their size, cost, and thermal fluid requirements.

The commercially available heat-operated systems are in most cases designed for specific applications and for use with specific types of energy sources, such as fossil-fuel combustion with natural gas. Therefore, identified units are further studied and evaluated to determine if they can be used “as is” or after being modified. Commercial units that show promise are evaluated in greater detail with a specific focus on performance as a

function of the heat source temperature, and fluid flow rate. This evaluation requires interpreting and verifying specification sheets and performance data.

The intermediate flow loop must be designed, sized, and then operated so that the three major systems, along with other systems and equipment that interface with Texas A&M RELLIS Campus buildings can be shielded from the corrosive well water. This intermediate flow loop will use water as the working fluid, and the loop will be designed to minimize the temperature difference between the hot well-water and the three major heat-operated systems by using an efficient counter-flow heat exchanger. In addition, downstream of the heat exchanger will be an intermediate loop hot-water storage tank that modulates thermal loads and creates a thermal capacity. The tank supplies hot water to the various systems located throughout RELLIS which in addition to the three major system types could also be hot water coils to meet the heating loads of Texas A&M RELLIS Campus buildings. The intermediate loop as described is modeled and analytically evaluated to optimize its design and component arrangements to maximize energy transfer to the end-use systems.

In conjunction with the intermediate loop being modeled and designed, the three major heat-operated systems (absorption cooling, desiccant wheel dehumidification, and geothermal district heating system) are also modeled for energy transfer and performance. Verification of the three models is performed by comparisons with the real-world systems, and then the models will be used to predict system performance and temperature limits for the intermediate loop supply and return water.

An overall surface-system simulation is developed by combining the three heat-operated system models and the intermediate flow loop model, along with well-known building models used for determining heating/cooling loads. This overall simulation is used to size and select component systems and to determine the optimum arrangement of the three major systems to maximize the usage of well-water thermal energy. The different series and parallel arrangements that are investigated in this optimization are identified in Table 3, and, as shown in the table, they can number as many as 17 different possibilities. The objective function in this arrangement optimization procedure is to maximize the temperature difference between the geothermal fluid supply and return with a given flow rate.

Table 3. Combinations of series cascade and parallel arrangements for heat-operated systems. Reprinted from Redeveloping depleted hydrocarbon wells in an enhanced geothermal system (EGS) for a university campus: Progress report of a real-asset-based feasibility study, by R. Weijermars, D. Burnett, D. Claridge, S. Noynaert, M. Pate, D. Westphal, W. Yu, L. Zuo, 2018, Energy Strategy Reviews, Copyright 2018 by Elsevier [5].

Possible cases for 3 systems in series				**Possible cases for 3 systems in two loops**			
Case	Position 1 (highest temperature supply fluid)	Position 2 (middle unit)	Position 3 (lowest temperature return fluid)	Case	Loop 1 (single unit)	Loop 2 (2 units in series)	
					Position 1 (inlet is supply fluid)	Position 1 (inlet is supply fluid)	Position 2 (outlet is return flow)
F.	ABS	GDHS	DEH	L.	ABS	GDHS	DEH
G.	ABS	DEH	GDHS	M.	ABS	DEH	GDHS
H.	GDHS	ABS	DEH	N.	GDHS	ABS	DEH
I.	GDHS	DEH	ABS	O.	GDHS	DEH	ABS
J.	DEH	ABS	GDHS	P.	DEH	ABS	GDHS
K.	DEH	GDHS	ABS	Q.	DEH	GDHS	ABS

Note: ABS – Absorption Cooling System, DEH – Dehumidification System, GDHS – Geothermal District Heating System

- Case A is Conventional A/C System
- Case B is 3 loops—each system is supplied individually and directly from the heat source
- Case C is ABS only; Case D is ABS and DEH only; Case E is ABS and GDHS only

In addition to the optimization of the system configuration and arrangements, multiple pump sizes with VFDs, similar to the multi-chiller system, are analyzed and applied to CHW/HHW system since many campus buildings are running 24/7 with large load variations. A control schedule for this multiple pump size system is developed and energy savings obtained are compared.

Using the results of the overall system simulation and optimization investigation, an economic analysis of the surface system will be performed for cooling and heating actual buildings located on Texas A&M RELLIS Campus. This economic analysis will focus on minimizing costs, both capital and operating, while maximizing the use of subsurface thermal energy for cooling and heating of buildings, along with electrical and mechanical power production from the GDHS. Note that this research is to design a geothermal plant to replace the traditional chiller and boiler plant. The cost of pipelines for a district heating and cooling system remains the same.

Besides the economic analysis, an energy efficiency measure is conducted on this integrated system. Since the low-temperature hot water is “free” with considerable pump power consumption, traditional energy efficiency indices do not work well. The whole building cooling/heating efficiency measure called the Building Systems Load/Energy

Ratio (LER) and discussed in Section 3.4 is applied so that the integrated system can be directly compared to traditional systems.

4.1 Thermal Fluid Properties from the Subsurface System

Exponent Energy, an Oklahoma-based oil and gas company, currently operates six wells on the Texas A&M RELLIS Campus, where two inactive wells (Riverside #2 and #5) are ideally placed to develop solutions for geothermal circulation, as shown in Figure 9 [5]. Note that the wellbores are structurally competent and able to withstand the anticipated stresses from the thermal fluid injection and disposal processes. These two subparallel horizontal wells are connected by a horizontal fracture channel, using the injected hot fluid as the working fluid, as shown in Figure 10. These wells could be connected by a single longitudinal fractured system (option a) or by a series of transverse vertical fractures (option b). Option b is selected here for the well pumping system analysis due to its reasonable pressure losses.

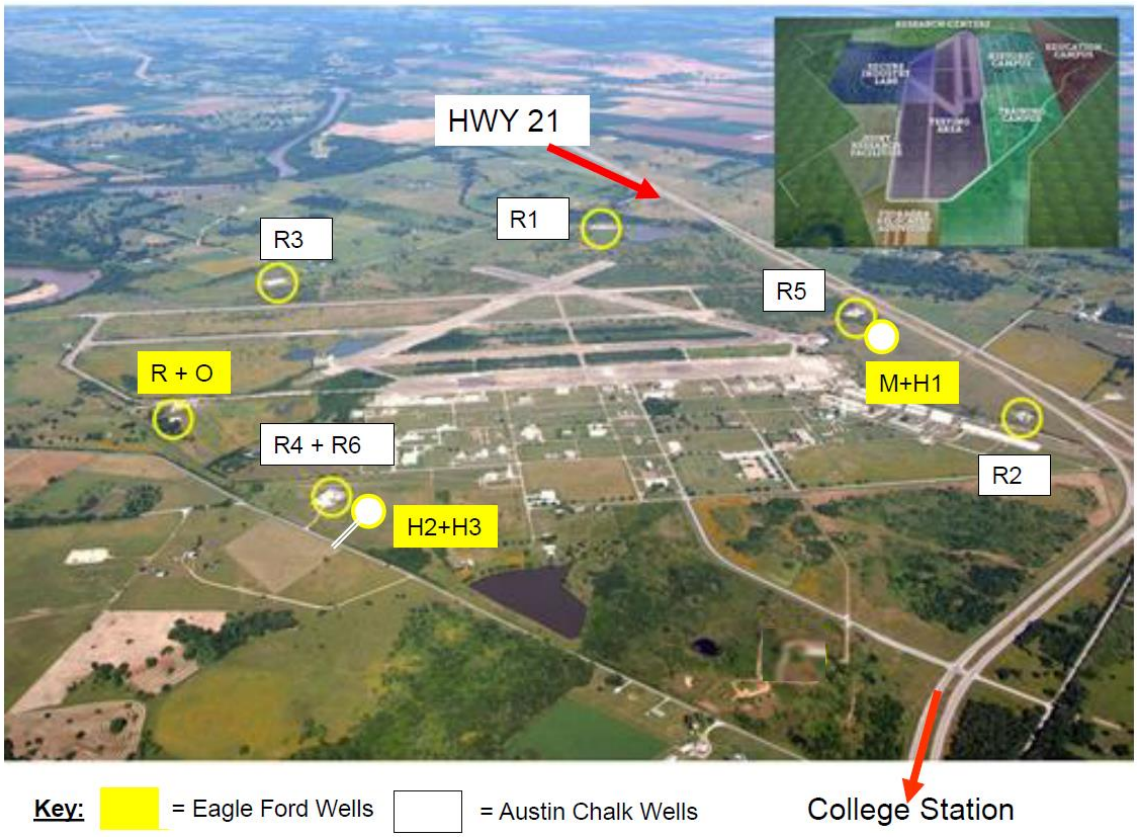

Figure 9. An overview map for well pads on Texas A&M RELLIS Campus. Reprinted from Redeveloping depleted hydrocarbon wells in an enhanced geothermal system (EGS) for a university campus: Progress report of a real-asset-based feasibility study, by R. Weijermars, D. Burnett, D. Claridge, S. Noynaert, M. Pate, D. Westphal, W. Yu, L. Zuo, 2018, Energy Strategy Reviews, Copyright 2018 by Elsevier [5].

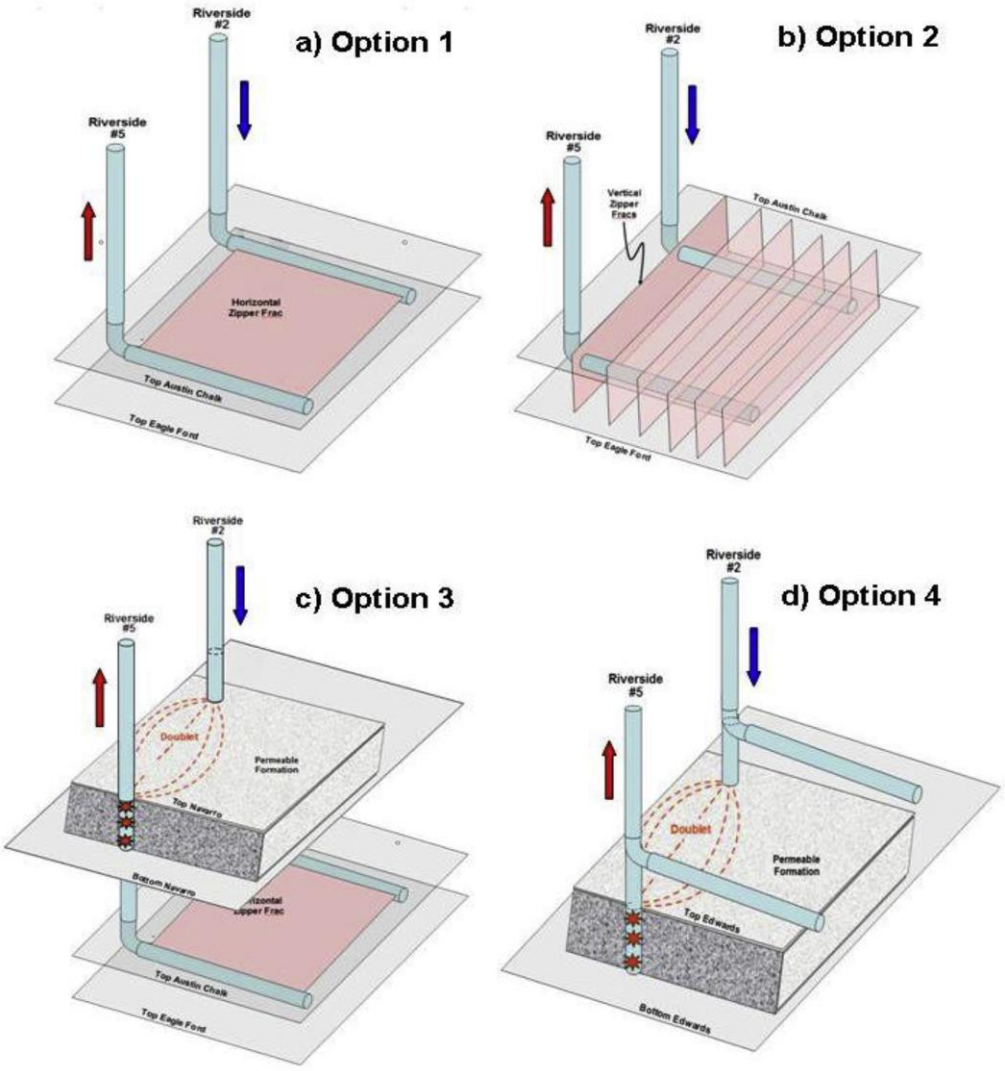

Figure 10. Development options a-d of Riverside #2 and #5 wells as a geothermal doublet. Reprinted from Redeveloping depleted hydrocarbon wells in an enhanced geothermal system (EGS) for a university campus: Progress report of a real-asset-based feasibility study, by R. Weijermars, D. Burnett, D. Claridge, S. Noynaert, M. Pate, D. Westphal, W. Yu, L. Zuo, 2018, Energy Strategy Reviews, Copyright 2018 by Elsevier [5].

A trip is made to visit all the well pads on the Texas A&M RELLIS Campus on March 4th, 2019. Figure 11 shows that a research group was visiting Riverside #4 and #6.

Riverside #2 and #5 were plugged in 2018 after the research proposal was written. And currently, Riverside #1 and #3 are available. The geothermal pumping model is still adopted for a general analysis.

Figure 11. A site visit on all well pad on Texas A&M RELLIS Campus.

4.1.1 Well Pumping System Analysis

In the well pumping system, the hot water is pumped into Riverside #2, then pushed through a horizontal fracture channel, and pumped out of Riverside #5, as shown in Figure 12. P_1, P_2, P_3, and P_4 are the flow pressures at the entrance of Riverside #2, the bottom of Riverside #2, the bottom of Riverside #5, and the entrance of Riverside #5. ΔP_{f1}, ΔP_{f2}, and ΔP_{f4} are the friction pressure drops of Riverside #2, the fracture channel,

and Riverside #5. ΔP_{pe1}, ΔP_{pe2}, and ΔP_{pe3} are the hydraulic pressure drops of Riverside #2, the fracture channel, and Riverside #5. ΔP_{ke1}, ΔP_{ke2}, and ΔP_{ke3} are the kinetic pressure drops of Riverside #2, the fracture channel, and Riverside #5.

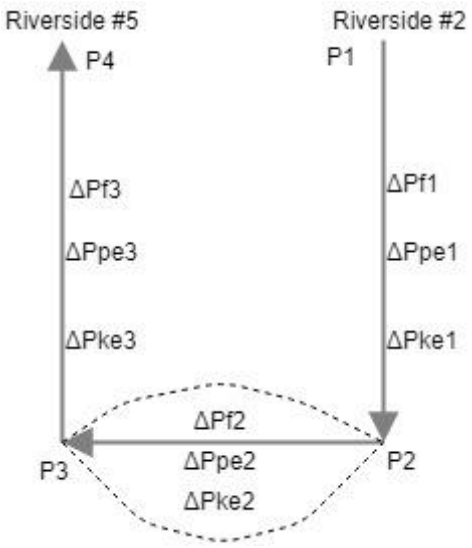

Figure 12. Well pumping system diagram for pressure analysis.

The pressure drop over a distance, L, of single-phase flow in a pipe can be obtained by solving the mechanical energy balance equation. If the fluid is incompressible (ρ = constant), and there is no shaft work device in the pipeline (a pump, compressor, turbine, etc.). The three terms on the right-hand side are the potential energy, kinetic energy, and frictional contributions to the overall pressure drop [124].

$$\Delta P = \frac{g}{g_c}\rho\Delta z + \frac{\rho}{2g_c}\Delta(u^2) + \frac{2f_f\rho u^2 L}{g_c D} = \Delta P_{pe} + \Delta P_{ke} + \Delta P_f \qquad (18)$$

For geothermal hot water in this application with 200°F (fluid density $\rho = 60.53\ \mathrm{lb_m/ft^3}$), the potential energy pressure drop ΔP_{pe} in psia per foot of vertical distance is

$$\Delta P_{pe} = \frac{g}{g_c}\rho = \gamma_w \frac{1\ \mathrm{lb_f}}{\mathrm{lb_m}} 60.53 \frac{\mathrm{lb_m}}{\mathrm{ft^3}} \frac{1\ \mathrm{ft^2}}{144\ \mathrm{in.^2}} = 0.42\gamma_w \Delta z \tag{19}$$

where γ_w is the specific gravity of the thermal fluid, defined as $\gamma_w = \frac{g}{g_c}$.

Since both wells have the same depth and the same working fluid, we have

$$\Delta P_{pe1} = \Delta P_{pe3} \tag{20}$$

$$\Delta P_{pe2} = 0 \tag{21}$$

ΔP_{ke} is the pressure drop resulting from a change in the velocity of the fluid between two positions. It will be zero for an incompressible fluid unless the cross-sectional area of the pipe is different at the two positions of interest.

$$\Delta P_{ke} = \frac{\rho}{2g_c}\Delta(u^2) \tag{22}$$

For ΔP_{f1} and ΔP_{f1} in wellbore pipelines in Riverside #2 and #5, we have

$$\Delta P_f = \frac{2f_f \rho u^2 L}{g_c D} \tag{23}$$

where f_f is the relative roughness with a value of 0.0637 in this case [125], ρ is the geothermal fluid density, u is the fluid velocity, L is the length of the pipeline, g_c is the standard gravitational constant, and D is the inner diameter of the well steel tube.

For ΔP_{f2} in the fracture channel connecting Riverside #2 and #5,

$$\Delta P_{f2} = \frac{q\mu_w L}{k_w A} \tag{24}$$

where q is the geothermal flow rate, $q = A \cdot u$, μ_w is the viscosity of the geothermal fluid, k_w is the water permeability, determined by the product of permeability k and the relative permeability of water k_{rw}, $k_w = k \cdot k_{rw}$, A is the sectional area, determined by the product of the channel height h and the channel width W, $A = h \cdot W$.

Assuming the geothermal hot water to be incompressible, then the kinetic energy pressure drop is 0.

$$\Delta P_{ke1} = \Delta P_{ke2} = \Delta P_{ke3} = 0 \tag{25}$$

Applying the overall pressure drop equation to both wells and the fracture channel, we have

$$P_1 - P_2 = \Delta P_{pe1} + \Delta P_{ke1} + \Delta P_{f1} \tag{26}$$

$$P_3 - P_2 = \Delta P_{pe2} + \Delta P_{ke2} + \Delta P_{f2} \tag{27}$$

$$P_4 - P_3 = \Delta P_{pe3} + \Delta P_{ke3} + \Delta P_{f3} \tag{28}$$

Combining these equations,

$$P_4 - P_1 = \Delta P_{f1} + \Delta P_{f2} + \Delta P_{f3} \tag{29}$$

Substituting all values, we have

$$P_4 - P_1 = 2 \cdot \frac{2f_f \rho u^2 L}{g_c D} + \frac{q\mu_w L}{k_w A} \tag{30}$$

$$= 2 \cdot \frac{2 \cdot 0.0637 \cdot 60.53 \frac{\mathrm{lb_m}}{\mathrm{ft^3}} \cdot \left(1.1347 \ \frac{\mathrm{ft}}{\mathrm{s}}\right)^2 \cdot 7{,}800 \ \mathrm{ft}}{32.17 \frac{\mathrm{ft} \cdot \mathrm{lb_m}}{\mathrm{lb_f} \cdot \mathrm{s^2}} \cdot 0.5 \ \mathrm{ft}} \cdot \frac{\mathrm{ft^2}}{144 \ \mathrm{in.^2}}$$

$$+ \frac{1000 \frac{\mathrm{bbl}}{\mathrm{day}} \cdot 0.31 \ \mathrm{cp} \cdot 5000 \ \mathrm{ft}}{8.2 \mathrm{md} \cdot 0.2 \cdot 200 \ \mathrm{ft} \cdot 3000 \ \mathrm{ft} \cdot 0.0.1}$$

$$= 224.4 \ \mathrm{psia}$$

4.1.2 Fluid Heat Loss Analysis

Heat loss happens when there are temperature differences between the geothermal fluid and the ground. According to the heat transfer theory [126], the basic formula to calculate heat loss induced by the heat transfer between ground and pipeline geothermal fluid is

$$q = \frac{T_w - T_g}{R_{tot}} \tag{31}$$

where q is heat loss of a unit length pipeline in unit time; R_{tot} is the heat resistance of a unit length pipeline; T_w is the geothermal fluid temperature as a function of the depth; and T_g is the ground temperature as a function of the depth.

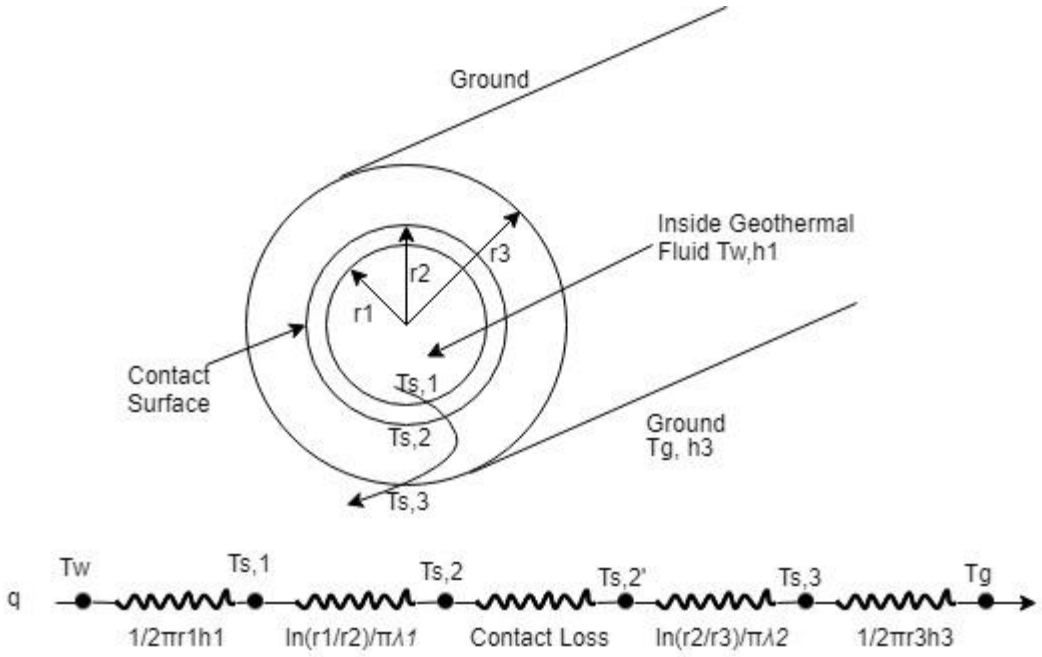

Figure 13. Conduction through circular well steel tube.

Figure 13 shows conduction through circular steel tube and insulation; the total heat resistance becomes

$$R_{tot} = \frac{1}{2\pi r_1 h_1} + \frac{1}{2\pi k_1}\ln\frac{r_2}{r_1} + \frac{R''_{tc}}{2\pi r_2} + \frac{1}{2\pi k_2}\ln\frac{r_3}{r_2} + \frac{1}{2\pi r_3 h_3} \quad (32)$$

where r_1 is the inner radius of the steel tube; r_2 is the external radius of the steel tube; r_3 is the external radius of the thermal insulation layer; k_1 is coefficient of heat conductivity of steel tube; k_2 is coefficient of heat conductivity of heat insulation layer; h_1 is convective heat transfer coefficient of hot water and the inner wall of steel tube; h_2 is the heat transfer coefficient of the outside wall of the pipeline; R''_{tc} is the contact loss efficient between the steel tube and the and its value depends on contact material surface roughness and contact pressure. For the sake of simplicity, R''_{tc} is assumed as 0.

Figure 14 shows the local geothermal gradient [5] and it is assumed in this dissertation that the geothermal temperature, T_g, increases linearly as the depth, z, increases. For the Riverside wells studied in this dissertation, the average depth of wells is 7800 ft, and the bottom temperature is 220°F. Note that the well bottom temperature will slowly decrease after years.

$$T_g = \frac{T_{bottom} - 145}{7800 - 4000} \cdot (z - 4000) + 145 \tag{33}$$

where T_{bottom} is the geothermal fluid temperature at the well bottom at a depth of 7,800 ft, which is assumed constant at 220°F. Then T_g (℃) is simplified as a linear function of the depth z (ft).

$$T_g = 0.021 \cdot z + 60.79 \tag{34}$$

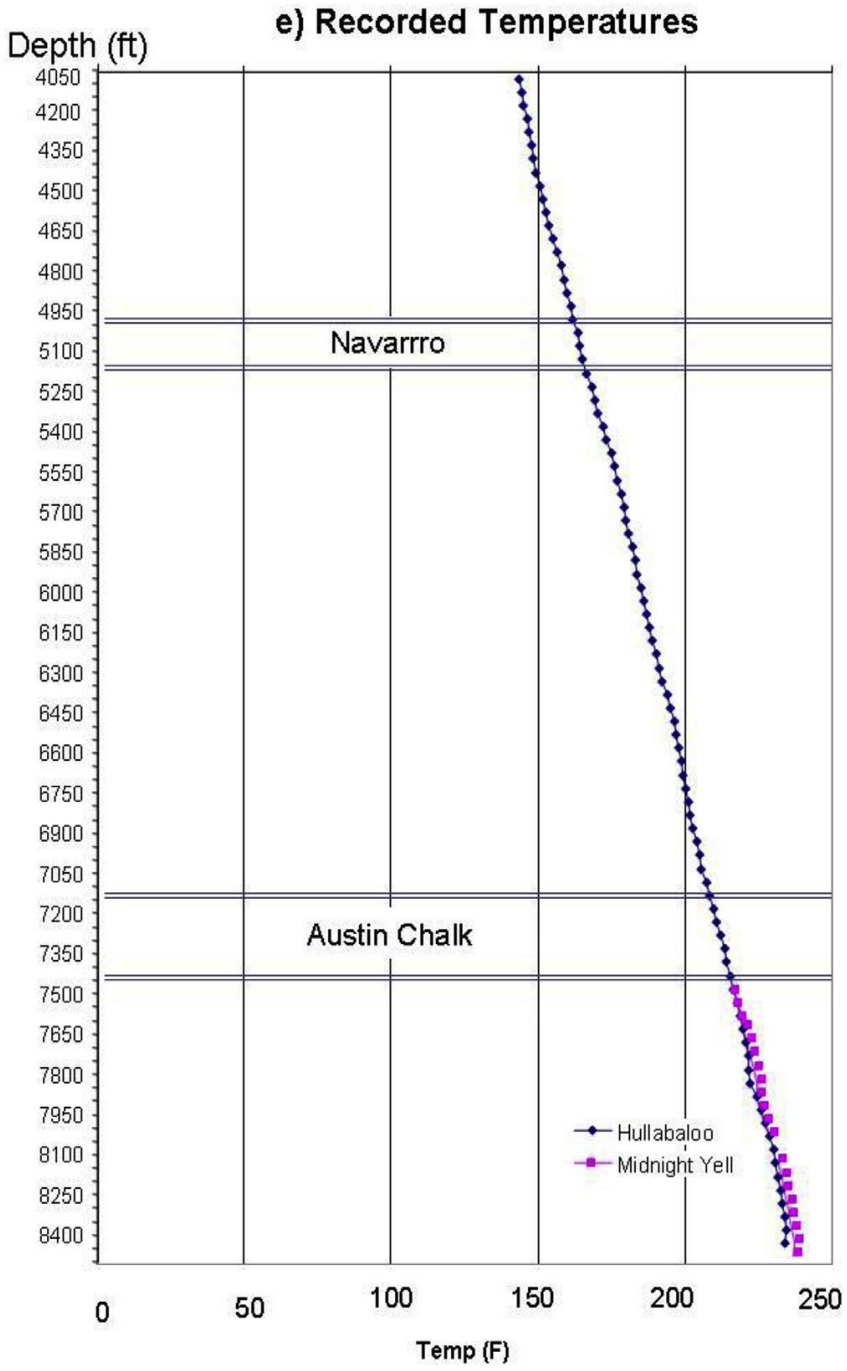

Figure 14. The local geothermal gradient for those two inactive wells (Riverside #2 and #5). Reprinted from Redeveloping depleted hydrocarbon wells in an enhanced geothermal system (EGS) for a university campus: Progress report of a real-asset-based feasibility study, by R. Weijermars, D. Burnett, D. Claridge, S. Noynaert, M. Pate, D. Westphal, W. Yu, L. Zuo, 2018, Energy Strategy Reviews, Copyright 2018 by Elsevier [5].

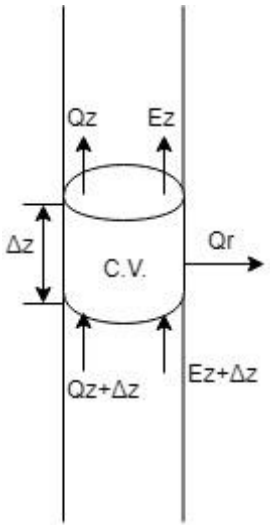

Figure 15. Schematic diagram of heat transfer performance analysis.

Figure 15 shows a control volume analysis for geothermal hot water heat transfer performance. Based on the energy balance, we have

$$(Q_{z+\Delta z} - Q_z) + (E_{z+\Delta z} - E_z) + Q_r = 0 \tag{35}$$

where Q_z is the heat conduction through geothermal fluids to and from the control volume, E is the mass internal energy flowing in and out of the control volume, and Q_r is the heat transfer from the geothermal fluid to the ground.

$$Q_z = A \cdot k \cdot T_w'(z) \tag{36}$$

$$E_z = A \cdot \rho \cdot u \cdot e(z) = A \cdot \rho \cdot u \cdot c_v \cdot T_w(z) \tag{37}$$

$$Q_r = A_s \cdot h \cdot (T_w - T_g) \tag{38}$$

$$A = \pi r_1^2 \tag{39}$$

$$A_s = 2\pi r_1 \cdot \Delta z \tag{40}$$

Substituting all these, we have

$$A \cdot k \cdot \left(T_w'(z+\Delta z) - T_w'(z)\right) + A \cdot \rho \cdot u \cdot c_v \cdot \left(T_w(z+\Delta z) - T_w(z)\right) + A_s \cdot \frac{\left(T_w - T_g\right)}{R_{tot}} = 0 \quad (41)$$

$$\pi r_1^2 \cdot k \cdot T_w''(z) \cdot \Delta z + \pi r_1^2 \cdot \rho \cdot u \cdot c_v \cdot T_w'(z) \cdot \Delta z + 2\pi r_1 \cdot \Delta z \cdot \frac{\left(T_w - T_g\right)}{R_{tot}} = 0 \quad (42)$$

The above equation can be simplified as

$$r_1 \cdot k \cdot T_w''(z) + r_1 \cdot \rho \cdot u \cdot c_v \cdot T_w'(z) + \frac{2T_w(z)}{R_{tot}} - \frac{0.042 \cdot z}{R_{tot}} - \frac{121.58}{R_{tot}} = 0 \quad (43)$$

It is a second-order linear ordinary differential equation for $T_w(z)$. The two boundary conditions are:

$$T_w(7800) = 220 \quad (44)$$

$$T_w'(7800) = 0 \quad (45)$$

Equation inputs are listed below:

$$r_1 = 3 \text{ in. } (0.0762 \text{ m});\ r_2 = 3.5 \text{ in. } (0.0889 \text{ m});\ r_3 = 5.5 \text{ in. } (0.1389 \text{ m});$$

$$h_1 = 7.07\ \frac{\text{Btu}}{\text{h} \cdot \text{ft}^2 \cdot {}^\circ\text{F}}\left(40\ \frac{\text{W}}{\text{m}^2 \cdot \text{K}}\right); h_3 = 3.536\ \frac{\text{Btu}}{\text{h} \cdot \text{ft}^2 \cdot {}^\circ\text{F}}\left(20\ \frac{\text{W}}{\text{m}^2 \cdot \text{K}}\right);$$

$$k_1 = 17.4\ \frac{\text{Btu}}{\text{h} \cdot \text{ft} \cdot {}^\circ\text{F}}\left(30\frac{\text{W}}{\text{m} \cdot \text{K}}\right);\ k_2 = 0.174\ \frac{\text{Btu}}{\text{h} \cdot \text{ft} \cdot {}^\circ\text{F}}\left(0.3\frac{\text{W}}{\text{m} \cdot \text{K}}\right);$$

$$k = 0.389\frac{\text{Btu}}{\text{h} \cdot \text{ft} \cdot {}^\circ\text{F}}\left(0.67\frac{\text{W}}{\text{m} \cdot \text{K}}\right); \quad (46)$$

$$\rho = 59.93\ \frac{\text{lb}}{\text{ft}^3}\left(960\ \frac{\text{Kg}}{\text{m}^3}\right), u = 1.1348\frac{\text{ft}}{\text{s}}\left(0.3459\frac{\text{m}}{\text{s}}\right);$$

$$c_v = 0.86\ \frac{\text{Btu (IT)}}{\text{lb} \cdot {}^\circ\text{F}}(3.6\ \frac{\text{KJ}}{\text{Kg} \cdot \text{K}})$$

Thus,

$$R_{tot} = 0.598\ \frac{h \cdot ft \cdot °F}{Btu}\ (0.347\ \frac{m \cdot K}{W}) \tag{47}$$

$T_w(z)$ can be solved as

$$T_w(z) = 0.012588 \cdot z + 281.11 \cdot e^{-0.000062958 \cdot z} - 192.81 \tag{48}$$

Let $z = 0$, and the temperature of geothermal fluid pumped to the surface for end use is

$$T_w(0) = 191°F\ (88.3℃) \tag{49}$$

Note that, if no insulation is installed, then

$$R_{tot} = \frac{1}{2\pi r_1 h_1} + \frac{1}{2\pi k_1} \ln\frac{r_2}{r_1} + \frac{1}{2\pi r_2 h_3} = 0.2457\ \frac{h \cdot ft \cdot °F}{Btu}\ (0.1425\ \frac{m \cdot K}{W}) \tag{50}$$

$$T_w(z) = 0.012588 \cdot z + 281.11 \cdot e^{-0.000062958 \cdot z} - 192.81 \tag{51}$$

$$T_w(0) = 160°F\ (71.1℃) \tag{52}$$

Similarly, as the thickness of the insulation layer is varied from 1.18 in. (30 mm) to 3.54 in. (90mm), the corresponding results are those listed in Table 4.

Table 4. Heat transfer performance by various insulation layer thicknesses.

Insulation Thickness (mm)	30	50	70	90	110	130	…	300
$\mathbf{R_{tot}\ (\frac{m \cdot K}{W})}$	0.2742	0.3470	0.4112	0.4685	0.5203	0.5674	…	0.8564
$\mathbf{T_w(0)}$	84.8°C 184.7°F	88.3°C 191°F	90.4°C 194.7°F	91.8°C 197.3°F	92.8°C 199.1°F	93.6°C 200.5°F	…	96.6°C 205.8°F

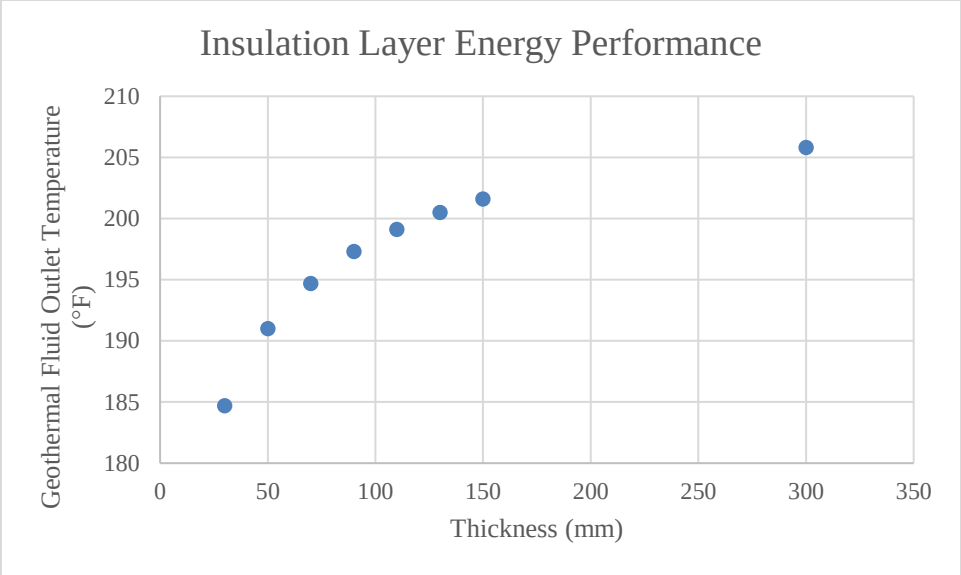

Figure 16. Thickness of insulation layer versus the geothermal fluid temperature.

Figure 16 shows the relationship between the thickness of the insulation layer and the geothermal fluid temperature. As the thickness increases, the geothermal fluid outlet temperature increases and the increasing rate decreases. Thus, there should be a trade-off between the insulation installation cost and the extracted geothermal energy output. While modern lateral wells have varying thickness and interior diameter based on the section of the wellbore, the older wells completed in the 1990s will typically allow an insulation thickness of 50mm [127].

4.1.3 Energy Performance of the Well Pumping System

The required pressure drop for the well pump is determined in section 4.1.1. The pumping power would be

$$P_w = \frac{(P_4 - P_1) \cdot q_w}{1714 \cdot \eta} \cdot \frac{0.7457\ \text{kW}}{\text{hp}} \tag{53}$$

where q_w is geothermal fluid flowrate in gpm and η is the pump efficiency.

A steady-state extraction of geothermal energy cannot be achieved over a longer time scales due to the rapid decline in the heat transfer rate at the fracture channel [128], and the geothermal fluid can be daily recovered at an estimated maximum output flowrate of 1,000 bbl/day (42,000 gallons/day) based on the evaluation by Weijermars et al. in 2017 [129]. Thus, the pump operating hours are

$$N = \frac{42{,}000\ \frac{\text{gallon}}{\text{day}}}{q_w \cdot 60\frac{\text{min}}{\text{hr}}} \tag{54}$$

Thus, the daily pump power consumption is

$$W_w = P_w \cdot N = \frac{(P_4 - P_1) \cdot q_w}{1714 \cdot \eta}\frac{0.7457\ \text{kW}}{\text{hp}} \cdot \frac{42{,}000\ \frac{\text{gallon}}{\text{day}}}{q_w \cdot 60\frac{\text{min}}{\text{hr}}} \tag{55}$$

Substituting all values, we have

$$W_w = \frac{224.4\ \text{psia} \cdot 0.7457\frac{\text{kW}}{\text{hp}} \cdot 42{,}000\text{gallon/day}}{1714 \cdot 0.8 \cdot 60\ \text{min/hr}} = 85.34\ \text{kWh/day} \tag{56}$$

Assuming the surface supply and return temperature difference is $50°F$, the energy output from the geothermal well would then be

$$\begin{aligned} Q_w &= c_v \cdot \rho \cdot V \cdot \Delta T \\ &= 1\frac{\text{Btu}}{\text{lb} \cdot °\text{F}} \cdot 60.53\frac{\text{lb}}{\text{ft}^3} \cdot \frac{\text{ft}^3}{7.48\ \text{gallon}} \cdot 42{,}000\frac{\text{gallon}}{\text{day}} \cdot 50°\text{F} \\ &\cdot \frac{\text{MMBtu}}{1{,}000{,}000\ \text{Btu}} = 16.99\frac{\text{MMBtu}}{\text{day}} \end{aligned} \tag{57}$$

where V is the daily output volume of the geothermal fluid.

Using the thermal energy supplied as calculated above and the calculated pumping power, the load to energy ratio (LER) [130] of the well pumping system is obtained. Note that 1 refrigeration ton = 3.52 $\mathrm{kWh_{thermal}}$ and 1 MMBtu = 1.055 GJ.

$$\mathrm{LER_{HW}} = \frac{\sum \mathrm{Q_{HW}}}{\sum \mathrm{P_{well\ pump}}} = \frac{16.99\ \mathrm{MMBtu/day}}{85.34\ \mathrm{kWh/day}} = \frac{4980\ \mathrm{kWh_{thermal}/day}}{85.34\ \mathrm{kWh/day}} = 58.4\ \ (0.06\ \mathrm{kW/ton}) \tag{58}$$

4.1.4 Geothermal Fluid Flowrate Variation Analysis

Although the geothermal energy output has a linear relationship with the fluid flowrate, the fluid flowrate variation influences the heat loss and the surface supplied geothermal fluid temperature. Furthermore, the pumping energy consumption is related to fluid flowrate in a complicated way. In this section, the geothermal fluid flowrate is varied to obtain optimal values of $\mathrm{LER_{HW}}$ and geothermal energy output.

The calculation process in sections 4.1.1 – 4.1.3 is repeated for different sets of geothermal fluid flowrates and the results are listed in Table 5 and Figure 17. The geothermal fluid flowrate is varied from 400 to 1,400 bbl/day with an increment of 200 bbl/day. Given that the pipeline size and the insulation layer thickness in existing wells are fixed in this analysis, the velocity increases as the fluid flowrate increases. Thus, the friction pressure losses increase as the fluid velocity increases, as well as the pump power required to circulate the geothermal fluid. As the fluid flowrate increases, while the heat loss rate to the ground remains the same, the surface supplied temperature increases, as well as the fluid return and supply temperature differences. Thus, the geothermal output increases. Overall, the $\mathrm{LER_{HW}}$ value increases when the fluid

flowrate is lower than 1,000 bbl/day and then starts to decreases a little bit since the increasing pump power compensates the extra geothermal energy output.

Table 5. LER values at different geothermal fluid flowrate.

Flowrate	**Velocity**	$\mathbf{P_4 - P_1}$	$\mathbf{T_w(0)}$	$\mathbf{\sum Q_{HW}}$	$\mathbf{\sum P_{well\ pump}}$	$\mathbf{LER_{HW}}$
bbl/day	ft/s	psia	°F	MMBtu/day	kWh/day	-
400	0.4539	168.2	156.0	2.0	25.6	23.4
600	0.6809	181.6	174.4	6.8	41.5	48.2
800	0.9078	200.3	184.6	11.8	61.0	56.9
1,000	1.1348	224.4	190.9	17.0	85.4	58.2
1,200	1.3618	253.8	195.4	22.2	116.0	56.0
1,400	1.5887	288.6	198.6	27.4	153.8	52.2

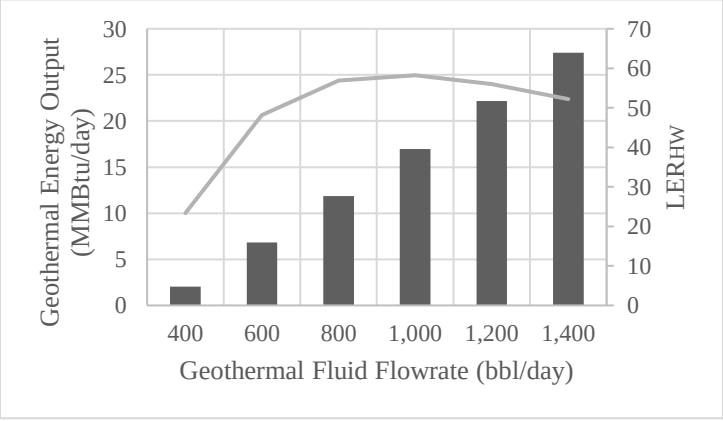

Figure 17. LER values and geothermal energy outputs at different geothermal fluid flowrate.

From the perspective of extracting a maximum amount of geothermal energy from the inactive wells, a higher fluid flow rate should always be considered. A fluid flowrate of 1,000 bbl/day is used and analyzed throughout this dissertation as the estimated maximum fluid flowrate. If the research goal is to achieve the highest utilization efficiency, then a fluid flowrate of 1,000 bbl/day should be selected based on the current existing well configurations.

4.2 Separate Models for Heat-Operated Units

4.2.1 Absorption Chiller Model with Hot Water Fired Generator

Figure 18 shows the flow schematic for an absorption chiller with a hot water heat source. It consists of four major components: Condenser, Evaporator, Generator, and Absorber. The absorbent solution is heated in the generator to generate the high-pressure refrigerant vapor, and the liquid refrigerant is vaporized in the evaporator to produce chilled water. Processes 1-6 are the absorbent solution cycle. The hot concentrated solution from the generator passes through the heat exchanger (process 4-5) and preheats the dilute solution from the absorber (process 2-3). Meanwhile, the concentrated solution is cooled, which increases the overall efficiency of the absorption chiller. Processes 7-10 are the refrigerant cycle. The refrigerant vapors from the generator are condensed in the condenser (process 7-8) and the liquid refrigerant at a lower pressure then evaporates taking away the heat in the evaporator (process 9-10). An absorption chiller requires a larger cooling tower compared to that needed for conventional compression chillers since the COP for an absorption chiller is typically

0.65-1 while that of compression chillers may be 3.5 or higher. Thus, the cooling tower consumptions are included in the energy performance analysis [43].

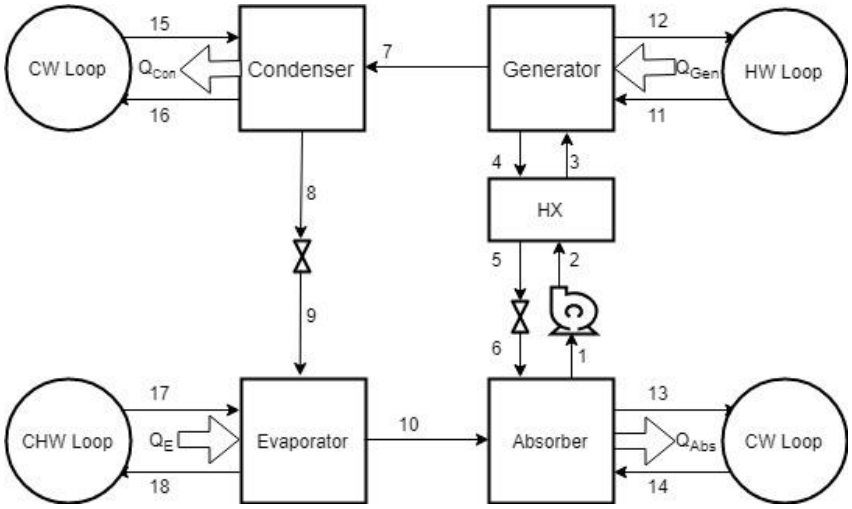

Figure 18. Flow schematic of an absorption chiller with hot water heat source.

The assumed design conditions for the absorption chiller model are listed as follows:

$$T_{13} = T_{15} = 85°F;\ \ T_{14} = T_{16} = 90°F;$$
$$T_{11} = 200°F;\ \ T_{17} = 53°F;\ \ T_{18} = 45°F \tag{59}$$

The adapted characteristic temperature difference model is adopted here. Reliable experimental data are required to solve the coefficients in the model. A 12kW cooling capacity single-effect ammonia-water absorption chiller prototype was developed by Joanneum Research in cooperation with the company Pink GmbH in Austria and a comprehensive set of operational data were recorded in Dr. Jerko Labus's dissertation [131]. The detailed data sets are listed Table 34. Studies demonstrate that

this model is also reliable on larger capacity absorption chillers [46]. ΔΔt′model coefficients for different capacity levels are given for hot water fired H2O/LiBr absorption chillers in the equations below with $\dot{Q}$ in kW and T in °C [45]. For the desired capacity, the heat transferred in each component can be obtained by proportional scaling estimation.

$$\dot{Q}_{eva} = \frac{\dot{m}_{eva}}{\dot{m}_{eva,rated}}(0.6288 \cdot T_{gen} - 1.2711 \cdot T_{ac} + 0.3801 \cdot T_{eva} + 1.6396) \quad (60)$$

$$\dot{Q}_{ac} = \frac{\dot{m}_{ac}}{\dot{m}_{ac,rated}}(1.2698 \cdot T_{gen} - 2.3951 \cdot T_{ac} + 1.0347 \cdot T_{eva}) \quad (61)$$

$$\dot{Q}_{gen} = \frac{\dot{m}_{gen}}{\dot{m}_{gen,rated}}(0.5662 \cdot T_{gen} - 1.3066 \cdot T_{ac} + 0.5947 \cdot T_{eva}) \quad (62)$$

where $\dot{Q}_{eva}, \dot{Q}_{ac}, \text{and } \dot{Q}_{gen}$ are heat transferred to the generator, the absorber-condenser, and the evaporator, with operating ranges of (40 - 54°F), (80 - 95°F), (175 - 212°F), correspondingly. Note that $T_{gen}, T_{ac}, \text{and } T_{eva}$ are external arithmetic mean temperatures of the generator, the absorber-condenser, and the evaporator which are determined in the equations below.

$$T_{eva} = \frac{T_{eva,in} + T_{eva,out}}{2} \quad (63)$$

$$T_{ac} = \frac{T_{ac,in} + T_{ac,out}}{2} \quad (64)$$

$$T_{gen} = \frac{T_{gen,in} + T_{gen,out}}{2} \quad (65)$$

For the sake of simplicity, the absorption performance curve remains the same and the heat transfer in each component shares the same scaling factor. Thus, we have

$$\frac{\dot{m}_{eva}}{\dot{m}_{eva,rated}} = \frac{\dot{m}_{ac}}{\dot{m}_{ac,rated}} = \frac{\dot{m}_{gen}}{\dot{m}_{gen,rated}} \tag{66}$$

Assuming the external flow rates are constant, when the hot water loop inlet condition is specified, the outlet condition is calculated below.

$$T_{GHW,R} = T_{GHW,S} - \frac{\dot{Q}_{gen}}{\rho \cdot V_{HW} \cdot C_{p,w}} \tag{67}$$

The absorption chiller COP is defined as below and the rated COP is assumed as 0.76 [45].

$$COP_{rated} = \frac{\dot{Q}_{eva}}{\dot{Q}_{gen}} = 0.76 \tag{68}$$

Since the generator operating temperature ranges from 175°F to 212°F and the designed geothermal fluid supply temperature is 191°F, the maximum temperature drop of the geothermal fluid would be 32°F. Thus, the maximum absorption chiller output would be

$$\begin{aligned} \dot{Q}_{gen,max}(MMBtu/hr) &= c_{pw}\rho V_{HW}(T_{GHW,S} - T_{GHW,R}) \\ &= \frac{1Btu}{lb \cdot °F} \cdot \frac{62.34lb}{ft^3} \cdot \frac{ft^3}{7.48gal} \cdot \frac{60min}{hr} \cdot \frac{MMBtu}{10^6 Btu} \cdot V_{HW}(gpm) \cdot \Delta T(°F) \\ &= \frac{V_{HW}(gpm) \cdot \Delta T(°F)}{2{,}000} = \frac{29.17\ gpm \cdot 32\ °F}{2{,}000} = 0.4667\ MMBtu/hr \end{aligned} \tag{69}$$

$$\begin{aligned} \dot{Q}_{eva,max} &= COP_{rated} \cdot \dot{Q}_{gen,max} = 0.76 \cdot 0.4667 \frac{MMBtu}{hr} \\ &= 0.3547 \frac{MMBtu}{hr}\ (29.56\ tons) \end{aligned} \tag{70}$$

$$\frac{\dot{m}_{gen}}{\dot{m}_{gen,rated}} = \frac{\dot{Q}_{gen}}{\dot{Q}_{gen,rated}} = \frac{0.4667\ MMBtu/hr}{24.04\ kW \cdot \frac{0.003412\ MMBtu/hr}{1\ kW}} = 5.69 \tag{71}$$

Fixing values at $T_{ac} = 87.5°F$ (30.83℃), $T_{eva} = 49°F$ (9.4℃), and $T_{GHW,S} = 191°F$ (88.33℃), combining Equations (62) and (69). Then, solve and find $T_{GHW,R} = 172.2°F$ (77.9℃). Thus, a typical design geothermal fluid temperature difference between supply and return is $191°F - 172°F = 19°F$.

Then, based on Equation (60), the absorption chiller output (tons) would be expressed as a function of geothermal fluid supply temperature (°F), which is simplified as below:

$$\dot{Q}_{eva} = 0.56517 \cdot T_{GHW,S} - 78.398 \quad (72)$$

Base on the experimental data, a simulated COP curve versus part load ratio (PLR) is obtained in Figure 19 and Equation (73) to cover the calculation on part load operations.

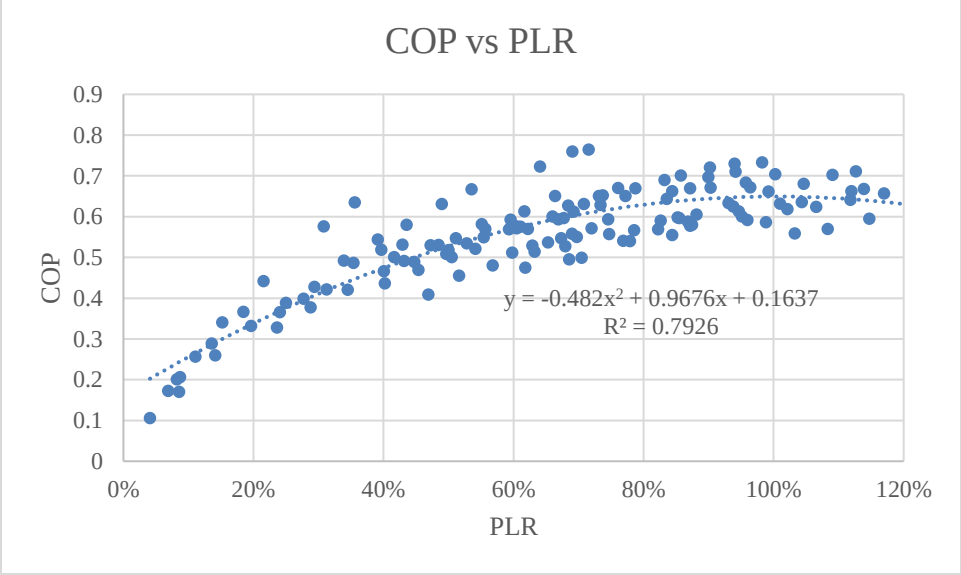

Figure 19. COP of case study absorption chiller at different part load ratios.

$$\mathrm{COP_{ABS}} = -0.482 \cdot \mathrm{PLR}^2 + 0.9676 \cdot \mathrm{PLR} + 0.1637 \quad (73)$$

4.2.2 Geothermal District Heating Model

As stated in section 3.1.4, a PHE energy efficiency (η_{PHE}) of 0.87 is assumed and the total distribution heat loss is 5%. Since the distribution system will be a closed loop with no high-rise buildings at the end, the substation heat exchanger is removed to avoid the unnecessary distribution pressure loss and heat loss. The GDHS system flow schematic is shown in Figure 20. Besides the GDHS energy efficiency, the hot water inlet temperature and the flowrate are also included as key factors influencing the overall energy efficiency. It is desired that the system extract as much energy as possible from each unit of geothermal fluid since electricity is required to pump the fluid from the well.

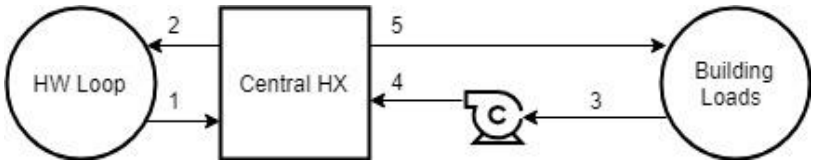

Figure 20. Flow schematic of the GDHS system.

Typical HVAC heating hot water temperature is 180°F (82°C) supply and 160°F (71°C) return. At these temperatures, it is difficult to integrate the low-temperature geothermal fluid to both absorption chiller and GDHS in a series configuration. However, as the temperature of the hot water drops, additional hot-water coil surface is

required to heat the supply air to the temperature required for space heating. For an existing heating system, it is impossible to increase coil surface, so an alternative solution to increase efficiency is to reset hot water supply temperature (HWST) during partial load based on outside air temperature as shown in Figure 21 [65] and Equations (74) - (75).

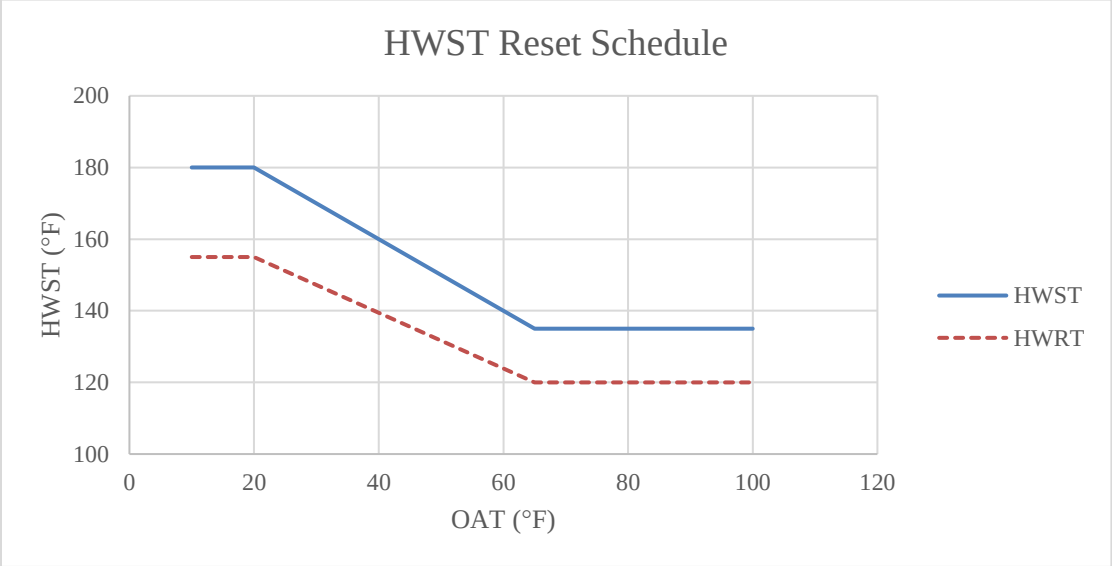

Figure 21. GDHS hot water supply temperature reset.

$$\mathrm{HWST} = \begin{cases} 180°\mathrm{F}, \mathrm{T_{OA}} \leq 20°\mathrm{F} \\ -\mathrm{T_{OA}} + 200°\mathrm{F}, 20°\mathrm{F} < \mathrm{T_{OA}} < 65°\mathrm{F} \\ 135°\mathrm{F}, \mathrm{T_{OA}} \geq 65°\mathrm{F} \end{cases} \quad (74)$$

$$\mathrm{HWRT} = \begin{cases} 155°\mathrm{F}, \mathrm{T_{OA}} \leq 20°\mathrm{F} \\ \dfrac{-7\mathrm{T_{OA}} + 1535°\mathrm{F}}{9}, 20°\mathrm{F} < \mathrm{T_{OA}} < 65°\mathrm{F} \\ 120°\mathrm{F}, \mathrm{T_{OA}} \geq 65°\mathrm{F} \end{cases} \quad (75)$$

4.3 Desiccant Wheel Model Development

4.3.1 Desiccant Wheel with Evaporative Cooling

Figure 22 shows the flow schematic of a typical desiccant cooling system with indirect evaporative cooling. Outdoor air for space cooling is drawn by a supply fan through a desiccant wheel, which dries and heats the air (process 1-2). Then the air passes through the indirect evaporative cooler (IEC) and mixes with the return air, where it is cooled by a heat exchanger (process 4-5). At the same time, the exhaust air, as a secondary air stream, travels through the IEC to be cooled (process 6-7). To maintain high efficiency of the desiccant wheel, an equivalent amount of scavenging air is heated separately, goes through the regenerator, and takes the humidity in the desiccant away (process 9-12). Other similar desiccant cooling systems have also been proposed by researchers. System parameters are studied to optimize thermal energy performance [86]. These include regeneration temperature, supply and regeneration air flow ratio, and indirect evaporative cooler secondary/primary air flow ratio. Based on the building load conditions and air conditioning requirements, a direct evaporative cooler may be added right before the supply air is delivered into zones [132].

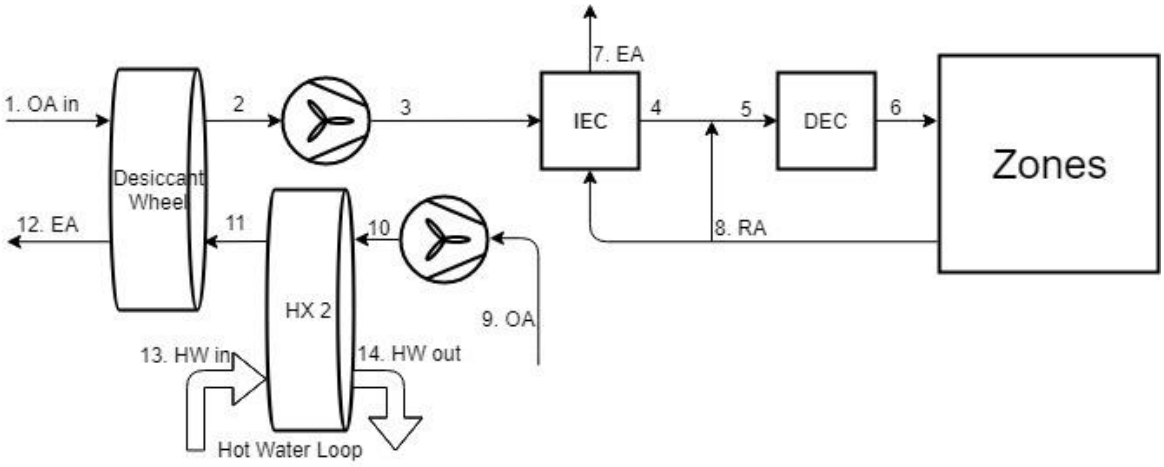

Figure 22. Flow schematic of an open loop desiccant cooling system with IEC-DEC.

Geothermal hot water heats a separate air flow using a heat exchanger, and then the hot air is used to regenerate the desiccant wheel. For two thermal flows across the heat exchanger, the enthalpy equality between the inlet and outlet is applied in Equation (76) with the assumption of a well-insulated wall for the heat exchanger. Regardless of this heat exchanger effectiveness, the scavenging air should be heated up to 140°F (60°C) as this is the most efficient inlet temperature for regeneration [79]. To maintain the maximum efficiency of the desiccant wheel, the scavenging air temperature is designed to be maintained near 140°F (60°C) by varying the hot water flowrate and the hot water temperature difference between supply and return.

$$h_{11} - h_{10} = h_{13} - h_{14} \tag{76}$$

where h_i is the air enthalpy at point i.

Along with the Jurinak model, we have the moisture balance in Equation (77) and energy balance in Equation (78). Note that the air flowrates through the desiccant wheel are the same for the best operating efficiency.

$$V_1 w_1 - V_2 w_2 = V_{11} w_{11} - V_{12} w_{12} \tag{77}$$

$$V_1 h_1 - V_2 h_2 = V_{11} h_{11} - V_{12} h_{12} \tag{78}$$

Where V_i, w_i is the air flowrate and humidity ratio at point i.

The enthalpy is calculated using Equation (79) from Chapter 6 of the 2001 ASHRAE Handbook of Fundamentals [133].

$$h_i = 0.24 \cdot T_i + (w_i \cdot (1061 + 0.444 \cdot T_i) \tag{79}$$

For the mixed air of outside air and return air, enthalpy balance (Equation (80)) and moisture balance (Equation (81)) are applied to find the mixed air temperature and humidity ratio. OA flowrate percentage is given a typical operation value of 15%, based on observation of typical campus buildings. Consequently, the return air flowrate percentage becomes 85%.

$$V_5 h_5 = V_4 h_4 + V_8 h_8 \tag{80}$$

$$V_5 w_5 = V_4 w_4 + V_8 w_8 \tag{81}$$

According to the EnergyPlus Engineering manual [42], the effectiveness of the indirect evaporative cooling, i.e., dry operation of the deactivated direct evaporative cooling unit, is calculated by Equation (82). A product of the sensible heat exchange (SHE) effectiveness and the direct evaporative cooling (DEC) effectiveness determines the effectiveness of IEC. A conventional SHE effectiveness is assumed to be 70% and the DEC effectiveness to be 90%. Thus, the IEC effectiveness in Equation (83) is a

constant of 63% [134]. Other parameters, like IEC pad size and air flowrate, are not considered in this simplified model. This model is selected because IEC is only simulated to compare with other configurations for demonstration.

$$\varepsilon_{IEC} = \frac{T_3 - T_4}{T_3 - T_7} \times 100\% \tag{82}$$

$$\varepsilon_{IEC} = \varepsilon_{SHE} \cdot \varepsilon_{DEC} \tag{83}$$

The IEC transfers no moisture to the primary system air from the secondary system air, so the humidity ratio remains the same.

$$w_3 = w_4 \tag{84}$$

The DEC effectiveness is defined in Equation (85). The web bulb temperature of the DEC inlet air is determined by the total mixture pressure of dry air and water vapor, dry bulb temperature, and the humidity ratio [133]. Note that the saturation pressure over liquid water for the temperature range of 32 to 392°F given in Equation (88).

$$\varepsilon_{DEC} = \frac{T_5 - T_6}{T_5 - T_{wb5}} \tag{85}$$

$$w_5 = \frac{(1093 - 0.556T_{wb5}) \cdot w_{wb5s} - 0.24 * (T_5 - T_{wb5})}{1093 + 0.444T_5 - T_{wb5}} \tag{86}$$

$$w_{wb5s} = 0.62198 \cdot \frac{p_{ws}}{p - p_{ws}} \tag{87}$$

$$\begin{aligned} \ln(p_{ws}) = &-\frac{10440.397}{T_{wb5}} - 11.29465 - 0.027022355 \cdot T_{wb5} \\ &+1.289036 \cdot 10^{-5} \cdot T_{wb5}^2 - 2.4780681 \cdot 10^{-9} \cdot T_{wb5}^3 \\ &+6.5459673 \cdot \ln(T_{wb5}) \end{aligned} \tag{88}$$

where p is the vapor pressure in psia, p_{ws} is the saturation vapor pressure, T_{wb5} is the wet-bulb temperature in °F at state 5, and T_{wb5s} is the thermodynamic wet-bulb temperature at state 5.

The indoor air temperature is assumed a constant 75°F. The latent load per occupant is 150 Btu/hr and the occupant density is five per 1,000 ft^2 [135]. The supply air flowrate is assumed as 1 cfm/ft^2. The moisture added into the return air by occupants is determined by Equation (92).

$$q_{latent} = 150\ \frac{Btu}{hr} \cdot S_{room} \cdot 5/1000 ft^2 \tag{89}$$

$$m_w = \frac{q_{latent}}{h_{fg}} = \frac{0.75 \cdot S_{room} Btu/hr/ft^2}{1050\ Btu/lb_w} \tag{90}$$

$$m_{air} = \rho V_{air} = \frac{S_{room} \cdot 1\ cfm/ft^2 \cdot 60\ min/hr}{13.35 ft^3/lb_{dry\ air} @ 75°F\ std.\ conditions} \tag{91}$$

$$w_{add} = \frac{m_w}{m_{air}} = \frac{0.75 \cdot S_{room}\ lb_w/hr/1050 ft^2}{S_{room} \cdot 60\ hr \cdot lb_{dry\ air}/13.35 ft^2} \approx 0.0002\ lb_w/lb_{dry\ air} \tag{92}$$

We combine Equations (6) to (9), (76) to (88) and solve them by MATLAB whose code is attached in Appendix B. The bin method [136] is applied here for energy calculations. Although it becomes less reliable while accounting for seasonal variations of solar gains, variable occupancy, thermostats setbacks during unoccupied hours, varying HVAC operational schedules, and extreme weather conditions, it is useful to fine-tune the selection and sizing of equipment. In this case, the bin method is used to determine the integrated system capacity. TMY3 hourly weather data for College Station is used to generate the bin data [137].

Table 6 lists the values of temperature (°F) and humidity ratio (lb_w/lb_{air}) for the desiccant wheel and the IEC-DEC. A performance example is given with an outside air condition of 87°F and $0.0161 lb_w/lb_{air}$ in Figure 23.

Table 6. MATLAB results for the desiccant wheel with IEC-DEC.

Weather Bin Data			**Desiccant Wheel**				**IEC**		**DEC**			
N_{bin}	T_1	w_1	T_2	w_2	T_{12}	w_{12}	T_4	w_4	T_5	w_5	T_6	w_6
163	32	0.0025	71.2	0.0003	100.7	0.0047	73.6	0.0003	74.8	0.0085	62.8	0.0113
220	37	0.0033	78.4	0.0005	98.5	0.0062	76.2	0.0005	75.2	0.0086	63.0	0.0114
350	42	0.0042	84.8	0.0008	97.1	0.0075	78.6	0.0008	75.5	0.0086	63.2	0.0115
483	47	0.0050	90.7	0.0012	96.2	0.0088	80.8	0.0012	75.9	0.0087	63.4	0.0116
577	52	0.0059	96.0	0.0018	96.0	0.0099	82.8	0.0018	76.2	0.0088	63.6	0.0117
802	57	0.0073	101.9	0.0027	95.1	0.0119	85.0	0.0027	76.5	0.0089	64.0	0.0118
905	62	0.0088	106.9	0.0039	95.2	0.0136	86.8	0.0039	76.8	0.0091	64.3	0.0120
866	67	0.0111	111.9	0.0059	95.3	0.0163	88.6	0.0059	77.1	0.0094	64.9	0.0122
1197	72	0.0130	115.6	0.0078	96.6	0.0182	90.0	0.0078	77.3	0.0097	65.3	0.0124
1402	77	0.0158	119.2	0.0106	98.0	0.0211	91.3	0.0106	77.5	0.0101	65.9	0.0128
779	82	0.0161	121.2	0.0112	101.0	0.0209	92.1	0.0112	77.6	0.0102	66.1	0.0128
446	87	0.0156	122.8	0.0112	104.3	0.0199	92.7	0.0112	77.6	0.0102	66.1	0.0129
408	92	0.0159	124.7	0.0119	107.4	0.0198	93.4	0.0119	77.8	0.0103	66.3	0.0129
129	97	0.0144	126.0	0.0110	111.1	0.0178	93.9	0.0110	77.8	0.0102	66.2	0.0129
33	102	0.0123	127.1	0.0095	114.9	0.0151	94.3	0.0095	77.9	0.0099	65.9	0.0127

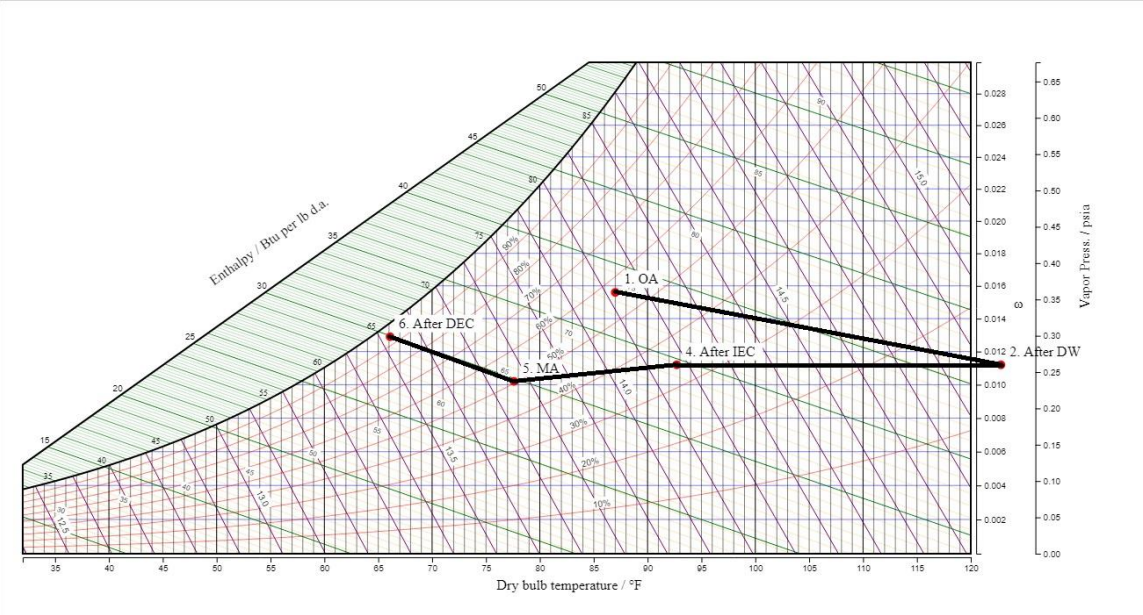

Figure 23. Performance example: desiccant wheel cooling system with IEC-DEC

According to the air properties of the supply air after IEC and DEC, supplemental cooling is required to meet the zone cooling load. Under this circumstance, the DEC only adds moisture to the supply air and slightly increases the air enthalpy when the outside air temperature is greater than 57°F. Hence the DEC component should be removed. On the other hand, the drawback of IEC is that it has no humidity control. The added moisture by occupants will gradually be accumulated until the relative humidity in the room exceeds the comfort zone. Therefore, a cooling coil is required to be installed and the new system diagram is listed in Figure 24. The energy performance of IEC will remain the same since only DEC is removed.

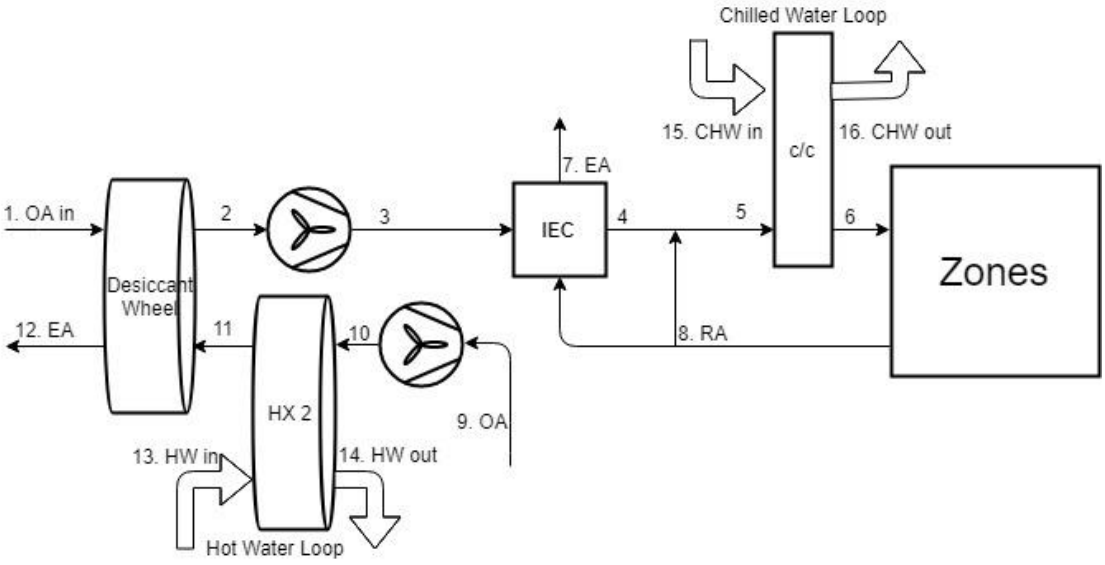

Figure 24. Flow schematic of an open loop desiccant cooling system with IEC only.

By comparing the supply air enthalpy and the outdoor air enthalpy, it is concluded that 100% outside air should be supplied to minimize the cooling load, when the outside air temperature is below 67°F (outside air enthalpy below 33.20 Btu/lb) This matches the building economizer mode shutoff limit of 65°F in hot and humid climate zone required by ASHRAE Standard 90.1 [138].

4.3.2 Desiccant Wheel with Heat Recovery

The heat exchanger (HX) effectiveness, ε_{HX}, is defined as the ratio of the actual heat transfer to the maximum possible heat transfer. When the properties of both thermal fluids are the same, ε_{HX} can be simplified as a function of inlet and outlet temperatures, as shown in Equation (93). In Figure 25, the heat exchanger cools the processed air (process 3-4) and warms the scavenging air (process 10-11), making the system run more efficiently. An IEC will not be able to cool the supply air sufficiently, so a chilled

water cooling coil is included to perform this function (process 5-6). Considering the limitation of counterflow with a finite heat transfer rate and heat exchange area, here ε_{HX} is taken as 0.8.

$$\varepsilon_{HX} = \frac{T_3 - T_4}{T_3 - T_{10}} \tag{93}$$

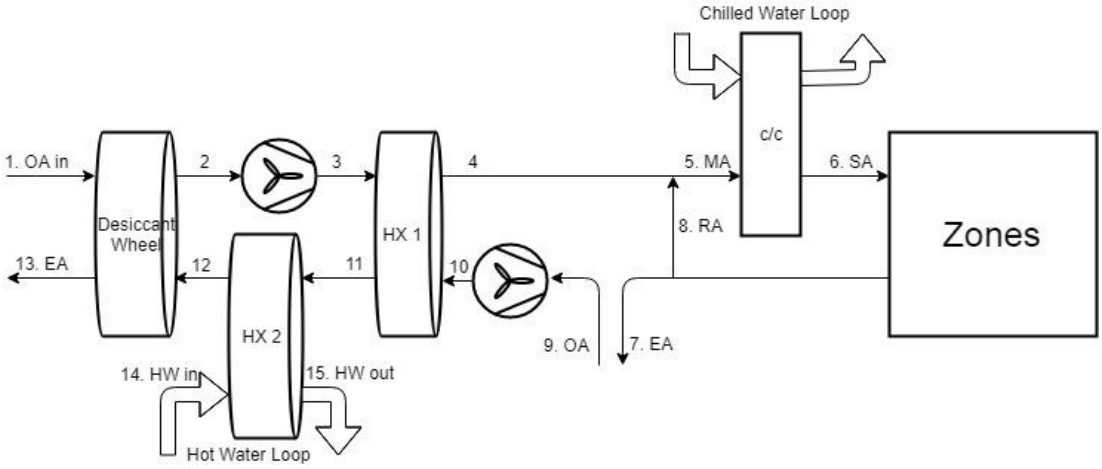

Figure 25. Flow schematic of an open loop desiccant cooling system with heat exchanger and chilled water cooling coil.

We combine Equations (76) to (93) and solve them by MATLAB whose code is attached in Appendix B. Table 7 lists the value of temperature (°F) and humidity ratio (lb_w/lb_{air}) for the desiccant wheel and the heat exchanger.

Table 7. MATLAB results for the desiccant wheel with heat recovery.

Weather Bin Data			Desiccant Wheel				Heat Exchanger			
N_{bin}	T_1	w_1	T_2	w_2	T_{13}	w_{13}	T_4	w_4	T_{11}	w_{11}
163	32	0.0025	71.2	0.0003	100.7	0.0047	39.8	0.0003	63.4	0.0025
220	37	0.0033	78.4	0.0005	98.5	0.0062	45.3	0.0005	70.1	0.0033
350	42	0.0042	84.8	0.0008	97.1	0.0075	50.6	0.0008	76.2	0.0042
483	47	0.0050	90.7	0.0012	96.2	0.0088	55.7	0.0012	82.0	0.0050
577	52	0.0059	96.0	0.0018	96.0	0.0099	60.8	0.0018	87.2	0.0059
802	57	0.0073	101.9	0.0027	95.1	0.0119	66.0	0.0027	92.9	0.0073
905	62	0.0088	106.9	0.0039	95.2	0.0136	71.0	0.0039	97.9	0.0088
866	67	0.0111	111.9	0.0059	95.3	0.0163	76.0	0.0059	102.9	0.0111
1197	72	0.0130	115.6	0.0078	96.6	0.0182	80.7	0.0078	106.8	0.0130
1402	77	0.0158	119.2	0.0106	98.0	0.0211	85.4	0.0106	110.7	0.0158
779	82	0.0161	121.2	0.0112	101.0	0.0209	89.8	0.0112	113.3	0.0161
446	87	0.0156	122.8	0.0112	104.3	0.0199	94.2	0.0112	115.6	0.0156
408	92	0.0159	124.7	0.0119	107.4	0.0198	98.5	0.0119	118.2	0.0159
129	97	0.0144	126.0	0.0110	111.1	0.0178	102.8	0.0110	120.2	0.0144
33	102	0.0123	127.1	0.0095	114.9	0.0151	107.0	0.0095	122.1	0.0123

Taking advantage of the exhaust air for heat exchange would improve the overall system efficiency and avoid the additional fan power consumption. A dedicated outside air system (DOAS) with a desiccant wheel is configured in Figure 26. Similarly, the temperature and humidity ratio values are listed in Table 8. Compared to energy

performance in Table 7, the desiccant DOAS system with HX results in both lower temperature and lower humidity ratio of the processed air when the outside air temperature is higher than 77°F. Therefore, in the following sections, only the DOAS System with the desiccant wheel is analyzed and its energy performance is optimized after studying all individual configurations. A performance example is given with an outside air condition of 87°F and 0.0161 lb_w/lb_{air} in Figure 27.

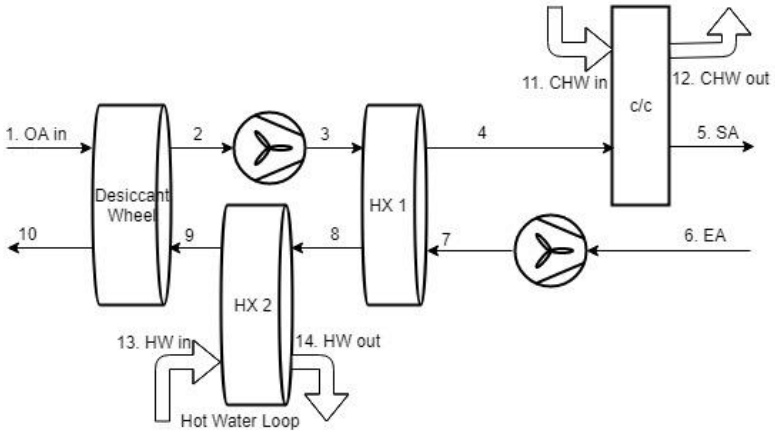

Figure 26. Flow schematic of an open loop desiccant DOAS with HX.

Table 8. MATLAB results for DOAS system with desiccant wheel and heat recovery.

Weather Bin Data			Desiccant Wheel				Heat Exchanger			
N_{bin}	T_1	w_1	T_2	w_2	T_{10}	w_{10}	T_4	w_4	T_8	w_8
163	32	0.0025	75.4	0.0013	97.1	0.0112	75.1	0.0013	75.3	0.01
220	37	0.0033	80.9	0.0016	96.5	0.0117	76.2	0.0016	79.8	0.01
350	42	0.0042	86.1	0.0020	96.3	0.0122	77.2	0.0020	83.9	0.01
483	47	0.0050	91.0	0.0024	96.3	0.0126	78.2	0.0024	87.8	0.01
577	52	0.0059	95.7	0.0029	96.6	0.0130	79.1	0.0029	91.6	0.01
802	57	0.0073	101.2	0.0036	96.0	0.0137	80.2	0.0036	96.0	0.01
905	62	0.0088	106.4	0.0043	95.8	0.0144	81.3	0.0043	100.1	0.01
866	67	0.0111	112.5	0.0055	94.6	0.0156	82.5	0.0055	105.0	0.01
1197	72	0.0130	117.4	0.0066	94.7	0.0164	83.5	0.0066	108.9	0.01
1402	77	0.0158	123.1	0.0082	93.8	0.0177	84.6	0.0082	113.5	0.01
779	82	0.0161	125.5	0.0087	96.5	0.0174	85.1	0.0087	115.4	0.01
446	87	0.0156	126.9	0.0088	100.1	0.0167	85.4	0.0088	116.5	0.01
408	92	0.0159	129.1	0.0094	102.8	0.0165	85.8	0.0094	118.3	0.01
129	97	0.0144	129.5	0.0091	107.5	0.0153	85.9	0.0091	118.6	0.01
33	102	0.0123	129.0	0.0085	113.0	0.0138	85.8	0.0085	118.2	0.01

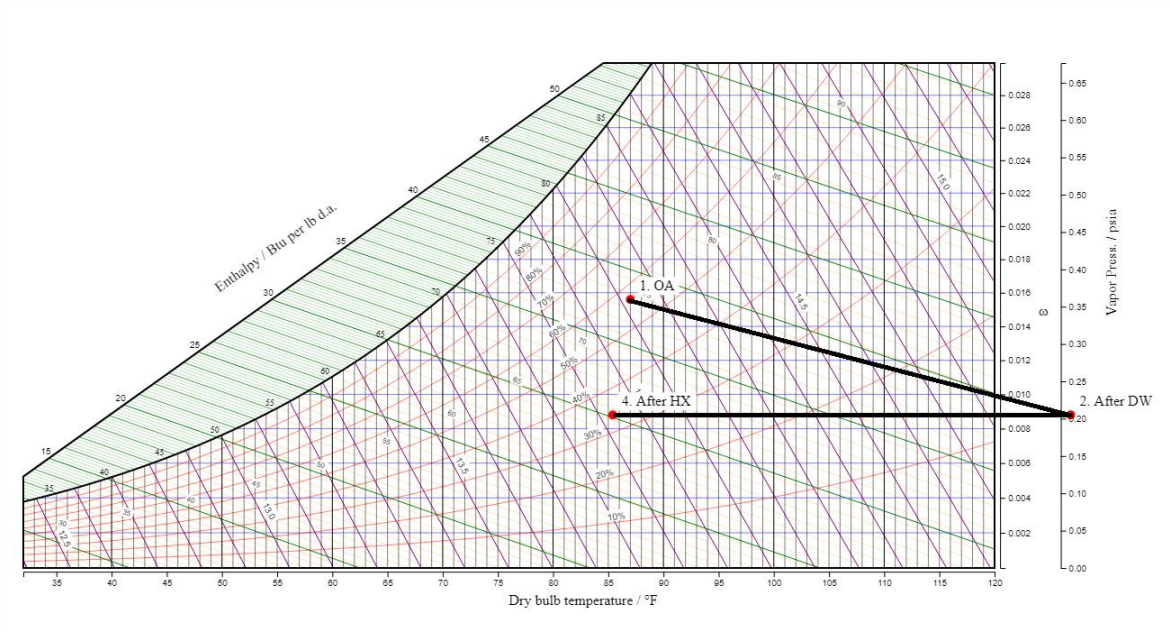

Figure 27. Performance example: desiccant DOAS with HX.

4.3.3 Desiccant Wheel with CW Cooling

As a type of the indirect evaporative cooling, cooling towers use evaporative cooling to reduce the temperature of circulated condenser water (CW), and they are an efficient way to produce condenser water whose temperature is generally lower than the outside air temperature. To distinguish with the CHW coil and CHW cooling, the heat exchanger used here is named as CW coil and CW cooling. A new configuration is proposed and evaluated based on the desiccant cooling system in Figure 28. Instead of using a heat exchanger, a condenser water cooling coil is applied to produce a larger temperature drop of processed air (process 3-4) so that the chilled water cooling coil load can be significantly reduced (process 5-6). It appears promising that the heat

exchanger and the condenser water cooling coil can be integrated to maximize the system energy efficiency, which is studied in the following sections.

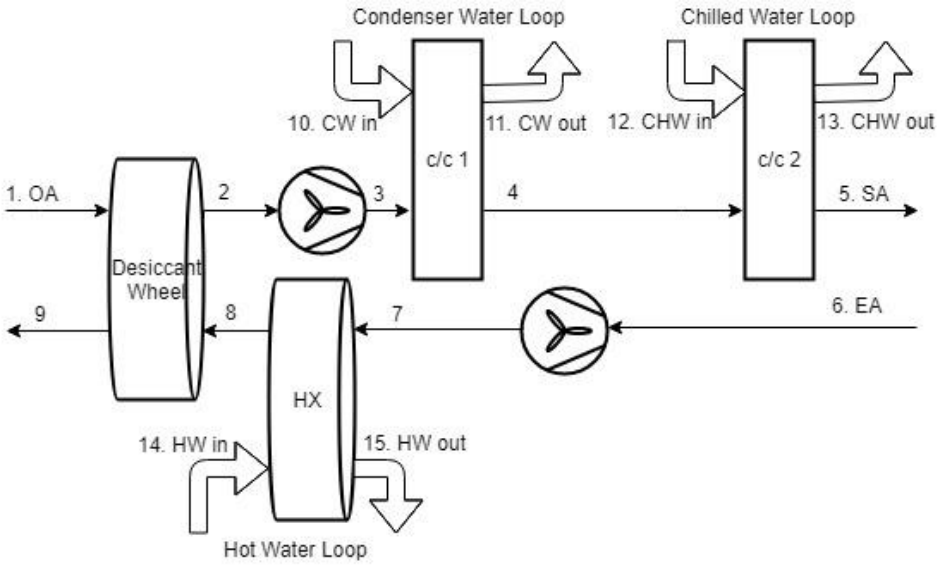

Figure 28. Flow schematic of an open loop desiccant DOAS with CW coil.

Compared to the heat exchanger, the condenser water cooling system involves extra energy inputs including the consumption of cooling tower fans and condenser water pumps. To compare the energy performance of different configurations thoroughly, the energy inputs need to be calculated corresponding to the cooling load removed through the CW coil. Thus, an empirical load to energy ratio (LER) [130] of the cooling tower is obtained based on the operating data of the Texas A&M Campus chiller plant. Available hourly data includes condenser water (CW) flow (V_{CW}), CW entering temperature ($T_{CW,e}$), CW leaving temperature ($T_{CW,l}$), cooling tower fan power ($P_{CT,fan}$), and CW pump power $P_{CW,pump}$. The hourly heat transferred in the CW cooling

coil is calculated by Equation (94), and a uniform LER_{CW} value is calculated by dividing the total heat transferred to the total consumption of cooling tower fans and CW pumps in Equation (95). Table 9 lists the energy transferred and consumption values from September 1st, 2012 to August 31st, 2013. A LER_{CW} value of 28.9 is used in this dissertation for energy consumption in the cooling tower.

$$q_{CW}\left(\frac{\text{MMBtu}}{\text{hr}}\right) = c_{pw}\rho V_{CW}\left(T_{CW,l} - T_{CW,e}\right) = V_{CW}(\text{gpm}) \cdot \Delta T(°\text{F})/2{,}000 \tag{94}$$

$$\begin{aligned} LER_{CW} &= \frac{\sum q_{CW}}{\sum\left(P_{CT,fan} + P_{CW,pump}\right)} \\ &= \frac{695{,}514\text{MMBtu}}{(2{,}043{,}513 + 5{,}019{,}626)\text{kWh}} \cdot \frac{293.3\text{kWh}}{\text{MMBtu}} \\ &= 28.9 \ \ (0.12\ \text{kW/ton}) \end{aligned} \tag{95}$$

Table 9. Cooling tower operating data from Texas A&M chiller plant.

Month	Condenser Water Heat Transferred	Cooling Tower Fan Consumption	Condenser Water Pump Consumption
	MMBtu	*kWh*	*kWh*
Sep-12	72,754	216,486	428,845
Oct-12	50,032	137,238	371,635
Nov-12	34,349	72,787	332,916
Dec-12	30,208	79,710	252,220
Jan-13	33,858	60,690	325,641
Feb-13	23,340	55,264	236,973
Mar-13	44,608	78,827	388,612

Table 9 (Continued).

Month	Condenser Water Heat Transferred	Cooling Tower Fan Consumption	Condenser Water Pump Consumption
	MMBtu	*kWh*	*kWh*
Apr-13	42,126	115,915	373,838
May-13	69,439	223,940	494,546
Jun-13	100,940	337,360	614,034
Jul-13	94,948	355,473	646,524
Aug-13	98,912	309,821	553,842
Total	695,514	2,043,513	5,019,626

Assume that the cooling tower capacity is large enough to cover the maximum cooling load from CW cooling coils so that the hot dry air from the desiccant wheel would be cooled down with an average air to water heat exchanger effectiveness of 0.87. As a common practice, the condenser water supply temperature (CWST) is reset based on the outside air wet bulb temperature [139]. In this dissertation, CWST reset in Equation (97) is applied to simulate the cooling tower performance, and the designed approach is 6°F according to the current on-campus cooling tower configuration. Assume that the cooling tower can maintain the CWST setpoint well and the HX in CW coil is adiabatic. Thus, based on the energy balance, the CW return temperature is obtained from Equations (96) to (98).

$$\varepsilon_{w-a} = \frac{T_3 - T_4}{T_3 - T_{10}} \tag{96}$$

$$\text{CWST SP} = \max(T_{OA,wb} + \text{Approach}, 65) \tag{97}$$

$$c_{pa}\rho_a V_a(T_3 - T_4) = c_{pw}\rho_w V_w(T_{11} - T_{10}) \tag{98}$$

Table 10 lists the values of temperature (°F) and humidity ratio (lb_w/lb_{air}) for the desiccant wheel and the CW cooling coil. A performance example is given with an outside air condition of 87°F and $0.0161 lb_w/lb_{air}$ in Figure 29.

Table 10. MATLAB results for the desiccant wheel with CW cooling coil.

Weather Bin Data			**Desiccant Wheel**				**CW Cooling Tower**		
N_{bin}	T_1	w_1	T_2	w_2	T_9	w_9	T_4	w_4	T_{10}
163	32	0.0025	75.4	0.0013	97.1	0.0112	66.3	0.0013	65
220	37	0.0033	80.9	0.0016	96.5	0.0117	67.1	0.0016	65
350	42	0.0042	86.1	0.0020	96.3	0.0122	67.7	0.0020	65
483	47	0.0050	91.0	0.0024	96.3	0.0126	68.4	0.0024	65
577	52	0.0059	95.7	0.0029	96.6	0.0130	69.0	0.0029	65
802	57	0.0073	101.2	0.0036	96.0	0.0137	69.7	0.0036	65
866	67	0.0111	112.5	0.0055	94.6	0.0156	79.9	0.0055	75.0
1197	72	0.0130	117.4	0.0066	94.7	0.0164	81.3	0.0066	75.9
1402	77	0.0158	123.1	0.0082	93.8	0.0177	86.4	0.0082	80.9
779	82	0.0161	125.5	0.0087	96.5	0.0174	89.1	0.0087	83.6
905	62	0.0088	106.4	0.0043	95.8	0.0144	73.2	0.0043	68.2

Table 10 (Continued).

Weather Bin Data			Desiccant Wheel				CW Cooling Tower		
N_{bin}	T_1	w_1	T_2	w_2	T_9	w_9	T_4	w_4	T_{10}
446	87	0.0156	126.9	0.0088	100.1	0.0167	89.8	0.0088	84.3
408	92	0.0159	129.1	0.0094	102.8	0.0165	89.9	0.0094	84.0
129	97	0.0144	129.5	0.0091	107.5	0.0153	89.4	0.0091	83.5
33	102	0.0123	129.0	0.0085	113.0	0.0138	90.2	0.0085	84.4

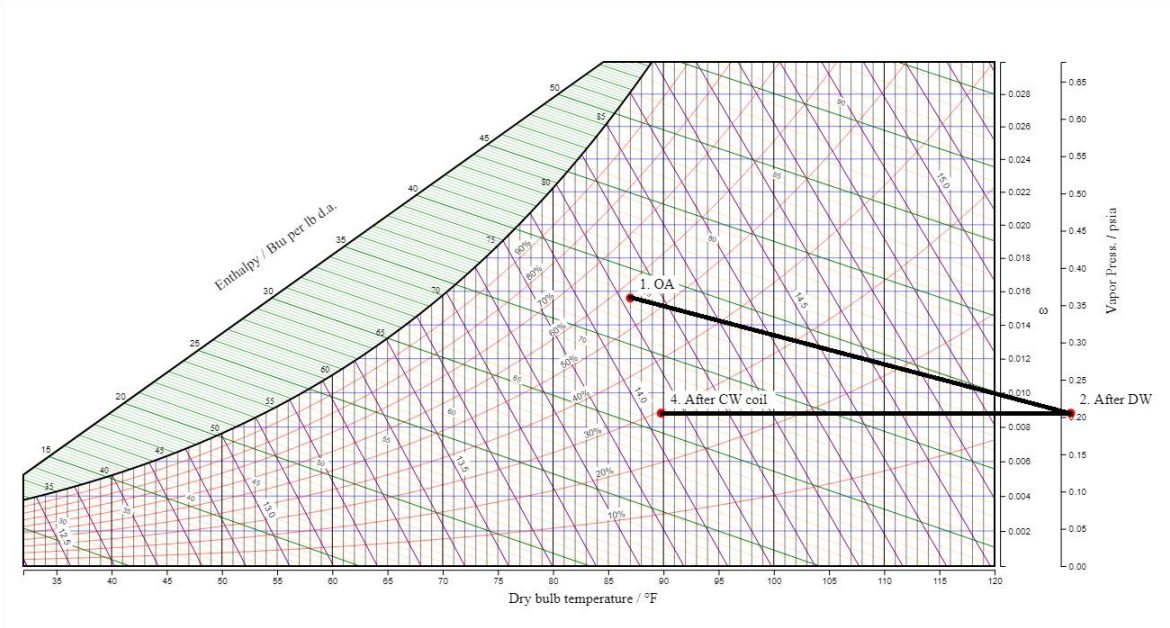

Figure 29. Performance example: desiccant DOAS with CW coil.

Compared to the exiting air from the HX and the CW coil, the HX generates lower supply air temperature when the outside air temperature is above 72°F. Since the HX preheats the regeneration scavenging air and saves the hot water energy input with

no energy cost, and the cooling COP of the cooling tower is way higher than that of a chiller, the CW cooling may be applied first when the supply air temperature after HX is higher than the CWST.

4.3.4 Optimized Desiccant Wheel Configuration

Integrating the heat exchanger (HX), condenser water (CW) cooling, and chilled water (CHW) cooling, an optimized desiccant wheel configuration is obtained and a flow schematic is shown in Figure 30. Outdoor air for space cooling is drawn by a supply fan through a desiccant wheel, which dries and heats the air (process 1-2). The heat exchanger cools the processed air (process 3-4) and warms the scavenging air (process 8-9), making the system run more efficiently. Then, a CW coil is applied to produce an additional temperature drop of processed air (process 4-5) so that the CHW coil load can be significantly reduced (process 5-6).

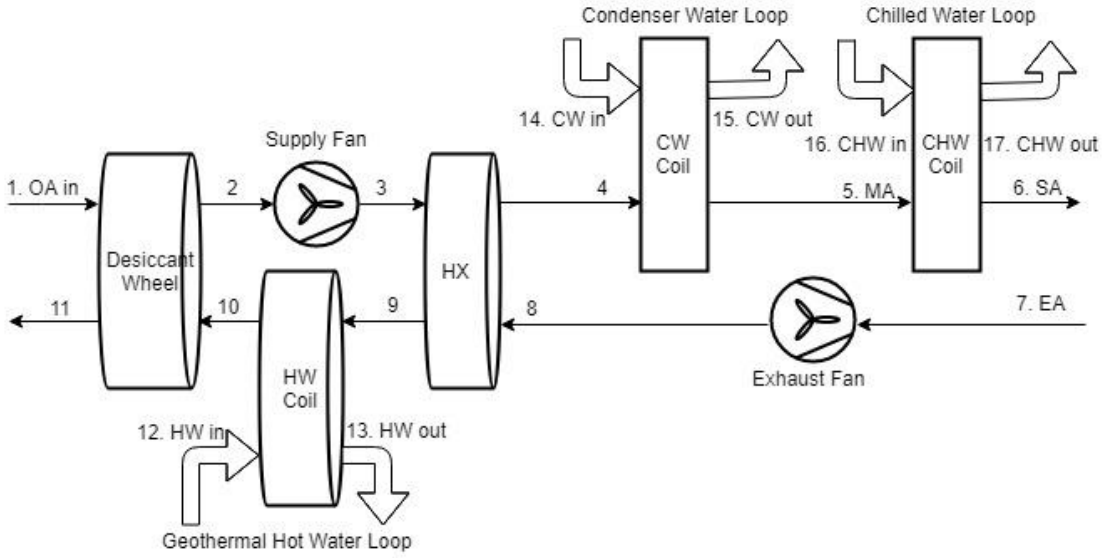

Figure 30. Flow schematic of an open loop desiccant DOAS with both HX coil and CW coil.

Table 11 lists the values of temperature (°F) and humidity ratio (lb_w/lb_{air}) for the desiccant wheel and the CW cooling coil. Also, the equivalent COP of the desiccant wheel is calculated for each bin using Equation (99), where $\dot{m}_{SA} \approx \dot{m}_{EA}$. The weighted COP_{DEH} is calculated as 0.81.

A performance example is given with an outside air condition of 87°F and $0.0161 lb_w/lb_{air}$ in Figure 31. Comparing the cooling load from process of point 1 to point 6 and process of point 5 to point 6, we can tell that the proposed DOAS system eliminates the latent load and even part of the sensible load of the building ventilation. Since the proposed system is designed to remove the latent load, it should be bypassed when the latent load does not exist. For example, during the winter at College Station, the ventilation latent load is very little, and the economizer should be enabled to bypass the desiccant wheel.

$$COP_{DW} = \frac{\text{CHW energy savings}}{\text{HW energy input}} = \frac{\dot{m}_{SA}(h_1 - h_5)}{\dot{m}_{EA}(h_{10} - h_9)} \tag{99}$$

$$COP_{DW,overall} = \frac{\sum N_i COP_{DW,i}}{\sum N_i} \tag{100}$$

Table 11. MATLAB results for the desiccant wheel with HX and CW coil.

Weather Bin Data			Desiccant Wheel		Heat Exchanger		CW Cooling		COP_{DW}
N_{bin}	T_1	w_1	T_2	w_2	T_4	w_4	T_5	w_5	
163	32	0.0025	75.4	0.0013	75.1	0.0013	66.3	0.0013	-
220	37	0.0033	80.9	0.0016	76.2	0.0016	66.5	0.0016	-
350	42	0.0042	86.1	0.0020	77.2	0.0020	66.6	0.0020	-
483	47	0.0050	91.0	0.0024	78.2	0.0024	66.7	0.0024	-
577	52	0.0059	95.7	0.0029	79.1	0.0029	66.8	0.0029	-
802	57	0.0073	101.2	0.0036	80.2	0.0036	67.0	0.0036	-
905	62	0.0088	106.4	0.0043	81.3	0.0043	69.9	0.0043	-
866	67	0.0111	112.5	0.0055	82.5	0.0055	76.0	0.0055	0.459
1197	72	0.0130	117.4	0.0066	83.5	0.0066	76.9	0.0066	0.764
1402	77	0.0158	123.1	0.0082	84.6	0.0082	81.4	0.0082	1.119
779	82	0.0161	125.5	0.0087	85.1	0.0087	83.8	0.0087	1.277
446	87	0.0156	126.9	0.0088	85.4	0.0088	84.4	0.0088	1.412
408	92	0.0159	129.1	0.0094	85.8	0.0094	84.3	0.0094	1.705
129	97	0.0144	129.5	0.0091	85.9	0.0091	83.8	0.0091	1.734
33	102	0.0123	129.0	0.0085	85.8	0.0085	84.6	0.0085	1.585

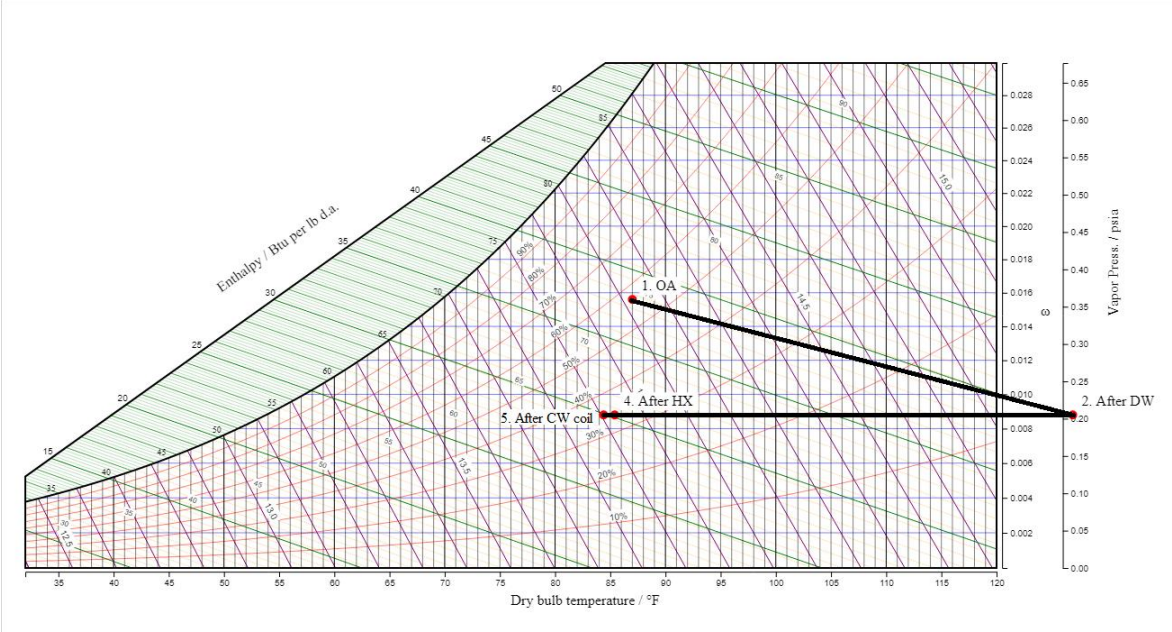

Figure 31. Performance example: desiccant DOAS with HX and CW coil.

4.3.5 Case Study – GSC Building

The desiccant wheel DOAS system with HX and CW cooling is applied to determine the savings potential in the General Service Complex (GSC) Building on the Texas A&M Campus to illustrate the methodology, shown in Figure 32. It is an administrative office building and the detailed building information is listed below:

Figure 32. Picture of GSC Building located in College Station, TX.

- Number of Floors: three on the left portion and two on the right portion of the building
- Building Size: 202,467 ft^2 (18,809 m^2)
- Roof Area: 85,303 ft^2 (7,925 m^2)
- Window to Wall Ratio: 0.16
- Building Operating Schedule: 8 AM to 5 PM on weekdays, 10 AM to 3 PM on weekends
- HVAC Equipment:
- Chilled Water System
    - District chilled water from the central system
- Single Duct VAV AHUs with reheat
    - 2 OAHUs pretreat the outside air
    - 10 AHUs serve the building
- Coils:
    - CHW cooling coil
    - HHW heating coil
- Fans:
    - 2 supply fans (25 HP (18.6 kW), 15 HP (11.2 kW)) on OAHU
    - 2 exhaust fans (15 HP (11.2kW), 10 HP (7.5 kW)) on OAHU
    - 10 supply fans (20HP (14.9 kW)) on AHUs
- Pumps:
    - 2 CHW pumps (30 HP (22.4 kW)) with VFDs
    - 2 HHW pumps (10 HP (7.5 kW)) with VFDs

Data from September 01, 2012 to August 31, 2013, are used for metered building energy consumption and weather inputs. Energy prices obtained from the TAMU Utilities & Energy Service website are listed in Table 12.

Table 12. Energy rates from TAMU Utilities and Energy Services website for TSC Building.

Energy item	Price
Electricity	$0.087/kWh
Chilled Water	$15.264/MMBtu
Heating Hot Water	$14.971/MMBtu

Table 13 lists the measured heating, cooling, and electrical energy usage by the GSC Building. The energy use index of this building is 103 $kBtu/ft^2 \cdot year$ (1.17 $GJ/m^2 \cdot year$). This is slightly lower than the median college/university building site EUI of 130.7 $kBtu/ft^2 \cdot year$ (1.48 $GJ/m^2 \cdot year$) as given in the U.S. EPA Portfolio Manager. If the electricity use is expressed in MMBtu, the total building consumption is 20,964 MMBtu/year (22,103 GJ/year), so the total HHW consumption is less than 3% of the total suggesting that there is very little reheat in this building. The CHW is supplied from a central utility plant with a uniform price of $15.26/MMBtu ($14.48/GJ)[140] and the yearly total CHW consumption of this building is 11,460 MMBtu (12,083 GJ).

Table 13. Measured heating, cooling, and electrical energy used by GSC Building.

Month	Measured ELE Use	Measured CHW Use		Measured HHW Use	
	kWh	MMBtu	GJ	MMBtu	GJ
Sep-12	223,129	1,126	1,187	31	33
Oct-12	229,583	946	997	35	37
Nov-12	209,523	694	732	44	46
Dec-12	201,952	554	584	71	75
Jan-13	217,754	584	616	92	97
Feb-13	199,801	560	590	47	50
Mar-13	219,855	675	712	48	51
Apr-13	218,577	835	880	41	43
May-13	224,027	1,119	1,180	35	37
Jun-13	219,233	1,372	1,447	31	33
Jul-13	232,245	1,485	1,566	33	35
Aug-13	233,826	1,510	1,592	25	26
Annual	2,629,506	11,460	12,083	532	561

The OAHUs provides around 20% of the total supply air and the economizer is enabled when the outside air temperature is lower than 55°F. Meanwhile, the desiccant wheel is bypassed when the OAT is lower than 65°F since the average humidity ratio is below 0.009 lb_w/lb_{air}. Figure 33 shows one of the OAHU schematic diagrams from the

campus building automation system. An excel spreadsheet is utilized to calculate the hourly OAHU cooling coil loads.

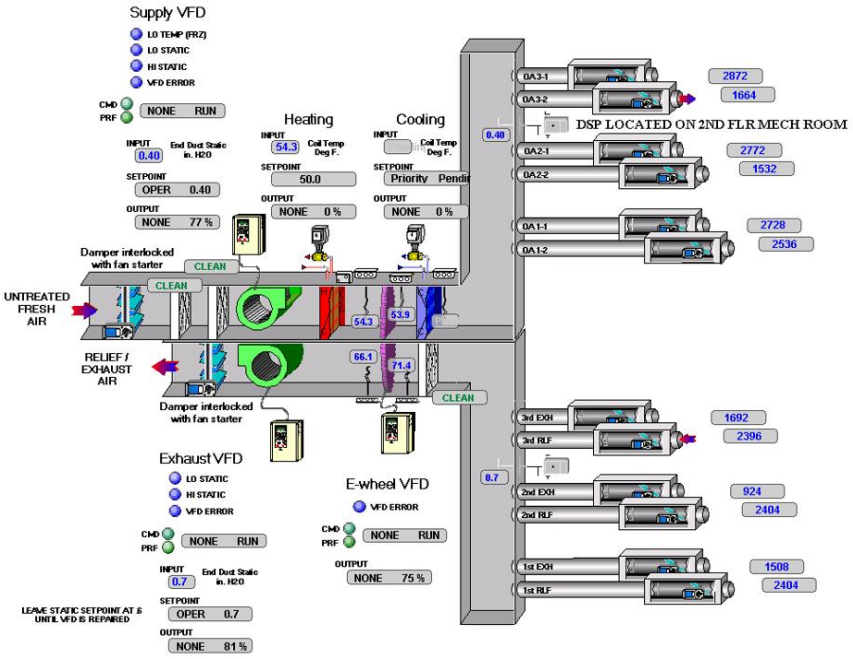

Figure 33. An OAHU schematic diagram from the building automation system.

An hourly analysis is conducted to compute energy savings based on the TMY3 weather data. Table 14 lists the monthly energy consumption and comparison based on the hourly analysis results.

Table 14. Monthly energy consumption and comparison based on the hourly analysis results.

Month	Traditional DOAS		Desiccant wheel DOAS		CW Coil Load		HW energy input	
	MMBtu	GJ	MMBtu	GJ	MMBtu	GJ	MMBtu	GJ
Jan	123	130	106	112	45	47	135	143
Feb	198	209	163	172	81	86	253	267
Mar	164	173	158	166	78	83	229	242
Apr	213	225	189	199	94	99	274	289
May	615	649	308	326	107	113	384	405
Jun	981	1,036	425	449	44	47	315	333
Jul	1,011	1,067	423	447	47	50	315	332
Aug	967	1,021	409	432	55	58	324	342
Sep	671	709	321	339	97	102	377	398
Oct	457	483	263	278	84	89	294	310
Nov	163	172	136	144	34	36	113	119
Dec	89	94	114	121	40	42	112	118
Total	5,652	5,967	3,017	3,185	806	851	3,123	3,298

After replacing the existing OAHUs by the new DOAS, the annual CHW coil load decreases from 5,652 MMBtu (5,967 GJ) to 3,017 MMBtu (3,185 GJ). The annual CW coil load is 806 MMBtu (851 GJ) and the hot water coil load is 3,123 MMBtu (3,298 GJ). The total energy consumption actually increases if energy loads on all coils

are summed. In other words, from the perspective of energy, this desiccant wheel application is not efficient at all. However, the low-grade geothermal hot water is considered a cheap energy source except for certain pumping energy consumption with an $\mathrm{LER_{HW}}$ of 58.9, and the CW cooling is extremely efficient with a $\mathrm{LER_{CW}}$ of 28.9 while the plant chiller has a COP of 4.6 in this case. If the electricity consumed to drive the well pump or the cooling tower is used to produce CHW by traditional chillers, the equivalent CHW consumption would be obtained as

$$\mathrm{Q_{CHW,CW}} = \frac{\mathrm{Q_{CW}}}{\mathrm{LER_{CW}}} \cdot \mathrm{COP_{chiller}} \tag{101}$$

$$\mathrm{Q_{CHW,HW}} = \frac{\mathrm{Q_{HW}}}{\mathrm{LER_{HW}}} \cdot \mathrm{COP_{chiller}} \tag{102}$$

Thus, the equivalent total cooling energy consumption for the new system is

$$\begin{aligned} \mathrm{Q_{tot}} &= \mathrm{Q_{c/c}} + \mathrm{Q_{CHW,CW}} + \mathrm{Q_{CHW,HW}} \\ &= 3{,}017 \ + \ 806/28.9 * 4.6 \ + \ 3{,}123/58.4 * 4.6 \\ &= \ 3{,}391 \text{ MMBtu } (3{,}580 \text{ GJ}) \end{aligned} \tag{103}$$

The cooling energy and cost savings are 2,261 MMBtu (2,385 GJ) and $34,512. The cooling energy to the DOAS is reduced by 40% and the whole building CHW consumption is reduced by 19.7%.

In this case study, ignoring the additional CW energy consumption, 3,123 MMBtu of hot water energy is provided to avoid the cooling coil energy of 5,652 - 3,017 = 2,635 MMBtu. Thus, the overall estimated hot water utilization efficiency of the DOAS system with the desiccant wheel is

$$\mathrm{LER_{DW}} = \frac{\text{CHW energy output}}{\text{HW energy input}} = \frac{2{,}635\ \text{MMBtu}}{3{,}123\ \text{MMBtu}} = 0.80 \tag{104}$$

4.4 Multiple Pump Sizes with VFDs Analysis

4.4.1 Multiple Pump Sizes with VFDs Configuration

The pump VFD curve of part load ratio and power ratio is shown in Equation (105) and Figure 34 below.

$$\text{Pump Power} = \text{Rated Power} \cdot \max((0.00153 + 0.0052 \cdot \text{PLR} + 1.1086 \cdot \text{PLR}^2 - 0.1164 \cdot \text{PLR}^3), 0.1) \tag{105}$$

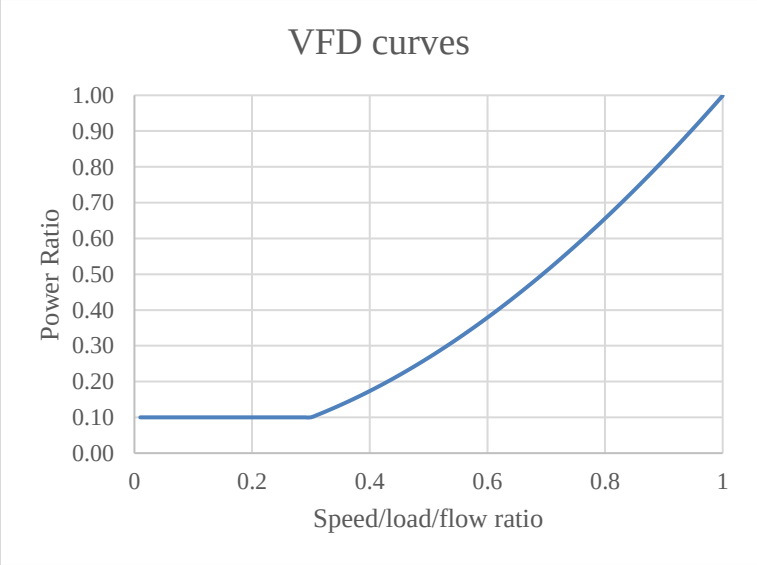

Figure 34. Pump VFD curve of part load power ratio versus flow ratio.

When the flow ratio is below 30% of the rated CHW/HHW flow, the pump power will stay at its minimum value, 10% of the rated power. Thus, the VFD pump works as constant speed and flow rate under 30% design zone load.

For zones with a large variation of loads, VFD pumps save energy compared to constant speed pumps, but they cannot avoid a certain percentage of hours running at the minimum speed for proper pump operations. Under this circumstance, a VFD pump with a lower capacity (Figure 35) can cover the operating hours with lower loads and save pumping power.

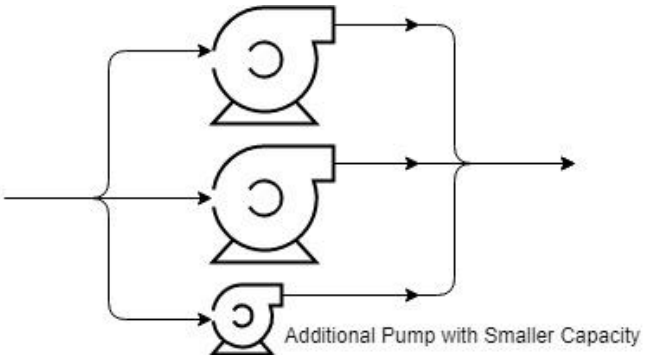

Figure 35. Flow schematic of the multiple pump sizes with VFDs configuration.

For the case studies demonstrating the methodology, the hourly consumption of pump energy, CHW and HHW usage is simulated based on a campus building at Texas A&M University. After this, multiple capacity levels of pumps are applied; the new hourly energy consumption is calculated and compared to the baseline. Energy savings, cost savings, and the simple payback period are analyzed.

The Texas State Chemist Building on the Texas A&M University Campus (subsequently denoted as TSC) and the Brooklyn VA Medical Center Main Hospital in New York (subsequently denoted as VA-Brooklyn) are selected as case study buildings to illustrate the methodology.

4.4.2 Case Study – TSC Building

The Texas State Chemist (TSC) Building is a small building, containing offices and testing laboratories in College Station, TX, as shown in Figure 36, with the basic characteristics listed below and building HVAC equipment summary in Table 15:

- Number of Floors: 1
- Building Size: 19,132 ft^2 (1,777.4 m^2)
- Roof Area: 19,132 ft^2 (1,777.4 m^2)
- Window to Wall Ratio: 0.22
- Building Operating Schedule: the occupancy schedules are mainly 6 AM to 6 PM on weekdays while a/c runs 24/7

Figure 36. Picture of TSC Building located in College Station, TX.

Table 15. TSC Building HVAC equipment summary.

Equipment Category	Detailed Item
CHW/HHW	District CHW/HHW from the central plant
Air Handling Units (AHUs)	One OAHU pretreats outside air Two single duct VAV AHUs with reheat serves office space Both VAV and CAV terminal boxes serve lab space
Coils	CHW cooling coil HHW heating coil
Fans	Two supply fans (25 HP (18.6 kW), 20 HP (14.9 kW)) Two exhaust fans (20 HP (14.9 kW), 15 HP (11.2 kW))
Pumps	Two CHW pumps (10 HP (7.5 kW)) with VFD Two HHW pumps (5 HP (3.7 kW)) with VFD

WinAM software, largely based on the ASHRAE Simplified Energy Analysis Procedure [141], was used to simulate the building energy performance in a typical year but the methodology may be applied using any reliable simulation program. [130]. The program was developed by the authors' laboratory to enable rapid calibration of a simulation to measure building energy consumption. The calibrated simulation is then typically used to estimate the savings from energy conservation measures applied to an existing building. It allows engineers to simulate an existing building's current operation, calibrate the simulation, and then determine the energy and financial savings of applying various energy conservation measures to a building. Unlike most building

energy modeling tools (e.g. EnergyPlus, eQUEST, DOE-2, etc.), the program is designed for the purpose of modeling existing buildings and estimating savings from energy conservation measures. But this energy analysis tool also accounts for the variation of HVAC equipment efficiency with outdoor temperature and part-load conditions in the same way as EnergyPlus.

After detailed site/building information is input, the simulation model is run using measured weather data. Then it is calibrated until its output reasonably matches the energy consumption data measured during the period which the weather data was measured. The calibration process used was a semi-automated version of the "characteristic signatures" process originated by Liu et al. [142] and described in more detail by Claridge [143]. A total error is defined as shown in Equation (106) by combining both Mean Bias Error (MBE) and Root Mean Square Error (RMSE) for calibrating simulations. Key parameters are adjusted to minimize the total error, such as outside air flow percentage, space temperature setpoint, energy recovery ventilation (ERV) efficiency, and cooling coil setpoint. In this case study, the calibrated simulation had a total error of 10%.

$$\begin{aligned} \mathrm{ERROR_{TOT}} &= [\mathrm{RMSE_{TOT}^2} + \mathrm{MBE_{TOT}^2}]^{1/2} \\ &= [(\mathrm{RMSE_{CLG}^2} + \mathrm{RMSE_{HTG}^2}) + (\mathrm{MBE_{CLG}} + \mathrm{MBE_{HTG}})^2]^{1/2} \end{aligned} \tag{106}$$

This calibrated simulation model is used to obtain hourly building loads and consumption. Both the CHW pump and the HHW pump's hourly power/consumption are determined by the total CHW/HHW usage simulated by the simulation's output spreadsheet using Equations (107) - (110) below.

$$PLR_{CHW} = \frac{hourly\ CHW\ usage}{maximum\ hourly\ CHW\ usage} \tag{107}$$

$$P_{CHW\ pump} = P_{CHW\ pump,rated} \cdot \max(0.00153 + 0.0052 \cdot PLR_{CHW} + 1.1086 \cdot {PLR_{CHW}}^2 - 0.1164 \cdot {PLR_{CHW}}^3, 0.1) \tag{108}$$

$$PLR_{HHW} = \frac{hourly\ HHW\ usage}{maximum\ hourly\ HHW\ usage} \tag{109}$$

$$P_{HHW\ pump} = P_{HHW\ pump,rated} \cdot \max(0.00153 + 0.0052 \cdot PLR_{HHW} + 1.1086 \cdot {PLR_{HHW}}^2 - 0.1164 \cdot {PLR_{HHW}}^3, 0.1) \tag{110}$$

When the speed ratio decreases to 0.3, the power ratio reaches its minimum value. Note that when the speed ratio is 0.5, the power ratio is 0.27 which is more than two times the value of 1/8 given by the pump Affinity Laws [144]. The theoretical and practical power ratios are different because the Affinity Law does not consider factors that do not scale with velocity and makes errors on the pump efficiency estimation, especially in the application of smaller pumps [145].

Based on the calculation results, the pump running hours at different power levels are shown in the following figures, and the hours at the minimum pumping power are listed in Table 16.

Table 16. Number of hours when pumps are running at minimum power in TSC Building.

Item	CHW Pump	HHW Pump
Rated Power (kW)	15	8
Operating Hours at minimum power	3,658	5,609
Percent of Hours at minimum power	41.8%	64%

Note: Hours are given for the year from September 1, 2012, to August 31, 2013, and the total number of hours is 8760.

Figure 37 shows a plot of hourly CHW pump power for the period from September 1, 2012, to August 31, 2013. In Figure 38, the left-hand side figure indicates the CHW pump power frequency for every 10% bin of the rated pump power, and the right-hand side figure shows the CHW pump energy consumption percentage versus the pump power bin in kW; both figures share the same vertical axis.

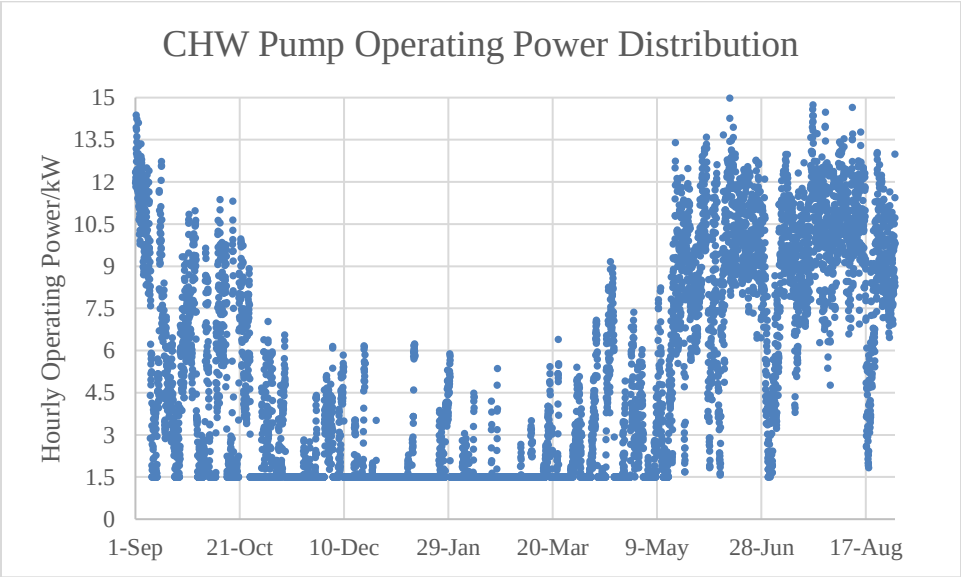

Figure 37. TSC Building CHW pump power hourly pumping power distribution.

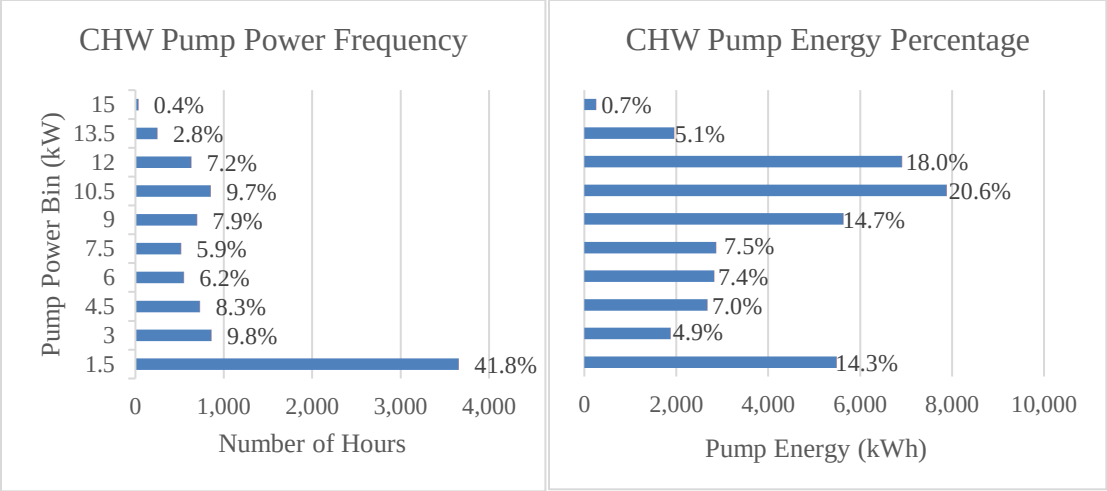

Figure 38. TSC Building CHW pump power and energy distribution statistical analysis.

Similarly, Figure 39 shows hourly HHW pump power for September 01, 2012 to August 31, 2013. Figure 40 shows the HHW pump power frequency and energy consumption percentage in each pump power bin.

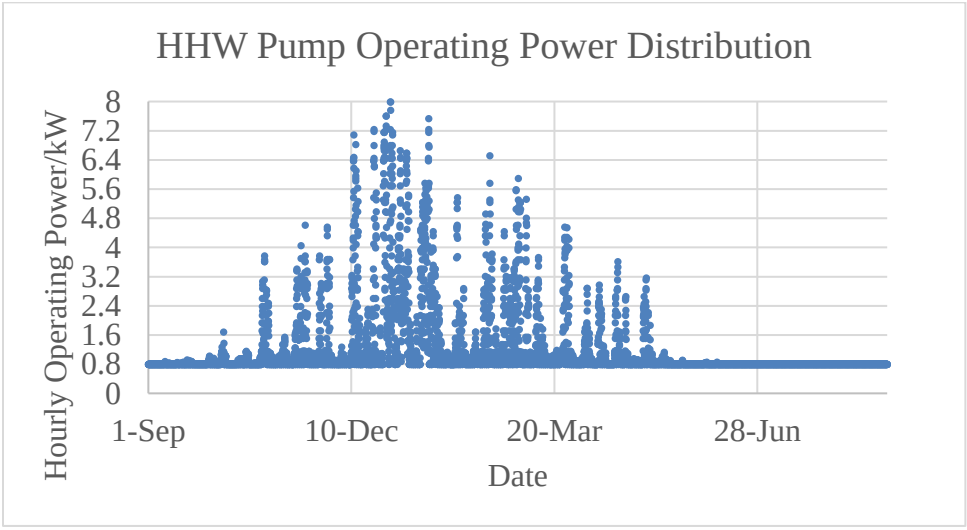

Figure 39. TSC Building HHW pump power hourly value distribution.

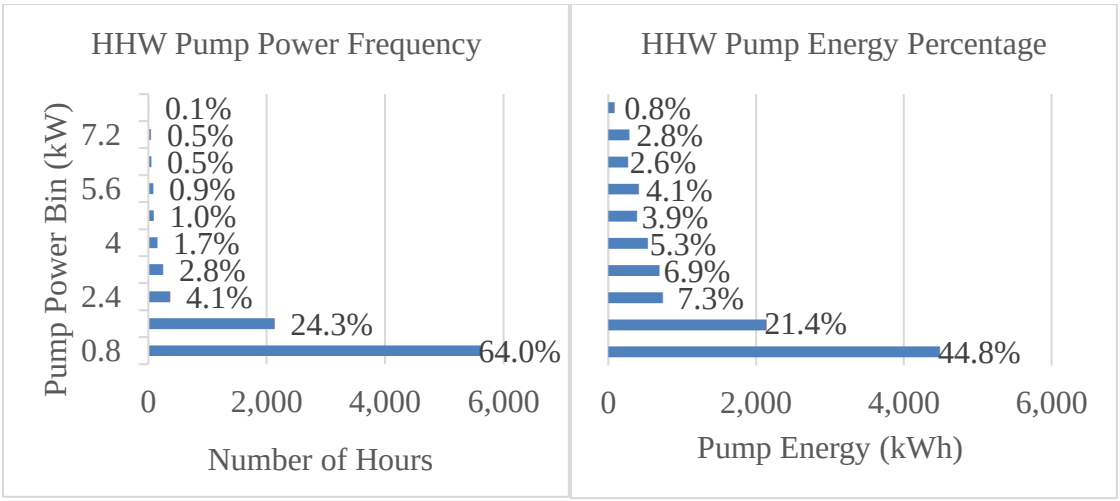

Figure 40. TSC Building HHW pump power distribution statistical analysis.

If two sets of pumps with different capacity are applied, then the lower load ratio hours can be supplied by a smaller pump, resulting in pump energy savings. Take the HHW pump system for example. Another HHW pump with a rated power of 10% of the main pump would be attached to the current pumping system to cover the 64% of HHW pump operating hours running at the minimum condition, as shown in Figure 41. Note that the smaller pump must be capable of maintaining the loop differential pressure. The pumping system will then function well when only the smaller pump is operated at low flows.

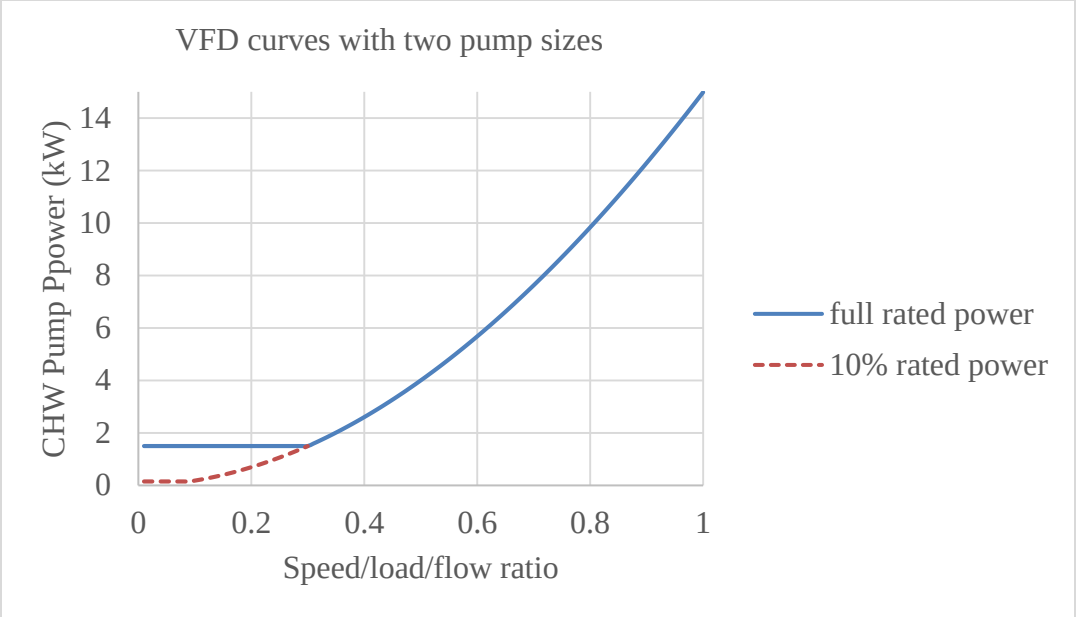

Figure 41. Multiple HHW pump sizes with VFD that can cover lower flows.

After a multiple pump size system is applied, the hourly pump energy consumption is calculated and compared to the consumption data of the original pump system. Energy and cost savings for the multiple pump size system are obtained and shown in Table 17.

Table 17. Energy and cost saving results for the multiple pump size system in TSC Building.

Item	kWh Savings	$ Savings	Baseline annual kWh consumption	Savings percentage
CHW Pump	4,292	$373	41,053	10.5%
HHW Pump	1,556	$135	10,015	15.5%

As an engineering application, the estimated total installation cost of a 1.5 hp CHW pump and a 1 hp HHW pump are analyzed and listed in Table 18. A simple payback analysis is shown in Table 19. The overall simple payback for the HHW pump is seven years and the simple payback of the CHW pump system upgrade is five years.

Table 18. Total installation cost of a 1.5 hp CHW pump and 1 hp HHW pump in TSC Building.

Item	Number	Unit Price [146] ($)	Total Price for CHW Pump ($)	Total Price for HHW Pump ($)
Tee/2''	2	13.32	26.64	26.64
Elbow/2''	4	4.27	17.08	17.08
Pipe/feet	30	2.53	75.9	75.9
Control valve	1	175	175	200
Pump (1.5 hp)	1	500	500	-
Pump (1 hp)	1	400	-	400
Control box	1	150	150	150
VFD	1	200	200	200
Electrical cable/150 feet	1	100	100	100
Installation labor (Estimated)		600	600	600
Total	-	-	1,869.62	1,744.62

Note:

1. Installation fee includes labor fee, pump installation, plumbing, and electrical hookup.
2. Control valve does not include remote control.

Table 19. Simple payback periods for multiple pump size system upgrades in TSC Building.

Pump Installation	Minimum flow rate	Installation Cost	Annual Cost Savings	Simple Pay Back (years)
CHW Pump	30%	$1,869.62	$373	5
HHW Pump	30%	$1,744.62	$135	13
Total	-	$3,614.24	$508	7.1

4.4.3 Case Study – VA-Brooklyn

The VA-Brooklyn Building is a large hospital with patient rooms, treatment rooms, and offices in New York City, NY, with the basic characteristics listed below:

- Number of Floors: 16
- Building Size: 602,208 ft^2 (55,947 m^2)
- Roof Area: 27,228 ft^2 (2,530 m^2)
- Window to Wall Ratio: 0.3

- Building Operating Schedule: 90% of the square footage runs 24/7 and 10% runs only 7 AM to 5 PM on weekdays

A picture of VA-Brooklyn is shown in Figure 42, and the energy rate is listed in Table 20. Table 21 shows the HVAC equipment summary of VA-Brooklyn.

Figure 42. Picture of VA-Brooklyn Building in New York City, NY.

Table 20. Electricity rate for VA-Brooklyn Building.

Energy item	Price
Metering Charges	$149.72/Month
Delivery Charges	$0.0221/kWh
Supply Charges (1/1 - 9/12)	$0.0713/kWh
Supply Charges (9/13 - 12/31)	$0.0709/kWh

Table 21. VA-Brooklyn Building HVAC equipment summary.

Equipment Category	Detailed Items
CHW/HHW	District CHW/HHW from the chiller/boiler plant
AHU	SDVAV, 100% OA with induction units
Coils	CHW cooling coil, HHW heating coil
Pumps	Three CHW pumps (100 HP (74.6 kW)) with VFD Three HHW pumps (40 HP (29.8 kW)) with VFD Three CW pumps ((100 HP (74.6 kW))

Based on the hourly simulation results, the CHW pump and the HHW pump's hourly power/consumption are determined, as shown in Table 22.

Table 22. Number of hours when pumps are running at minimum power in VA-Brooklyn Building.

Item	CHW Pump	HHW Pump
Rated Power (kW)	100	40
Operating Hours at minimum power	3377	5785
Percent of Hours at minimum power	38.6%	66%

Note: Hours given for the year from September 13, 2016, to September 12, 2017, and the total number of hours is 8760.

Figure 43 shows a plot of hourly CHW pump power for the period from September 13, 2016, to September 12, 2017. Figure 44 indicates the CHW pump power frequency and energy consumption percentage for every 10% bin of the rated pump power. When the outside air temperature is lower than 55°F, the CHW valve is closed for free cooling. Therefore, the CHW pump is shut off for 3,342 hours, and the CHW pump yearly total running hours are 5,418.

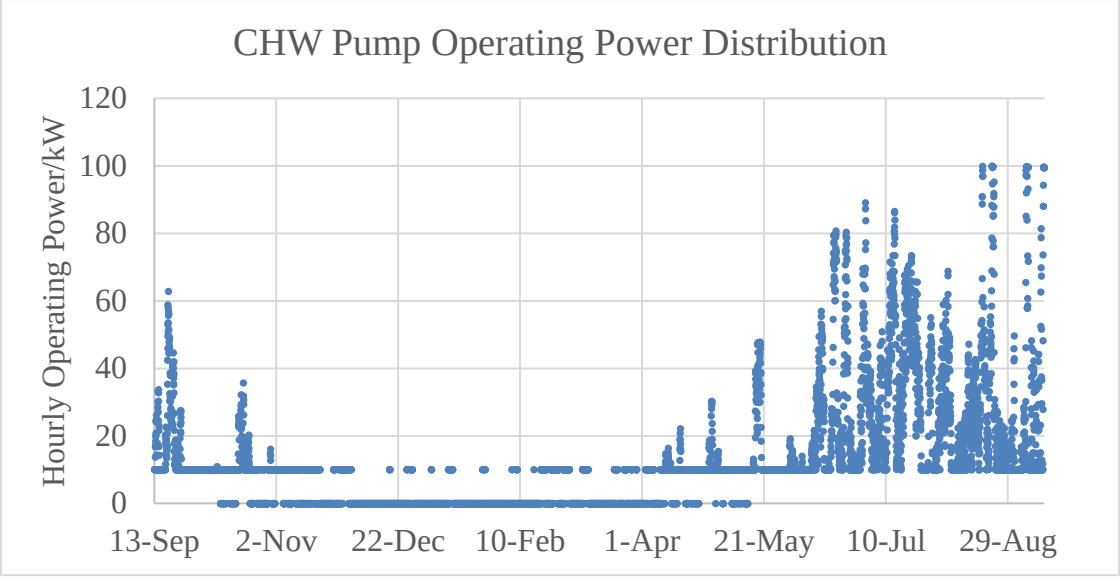

Figure 43. VA-Brooklyn Building CHW pump power hourly pumping power distribution.

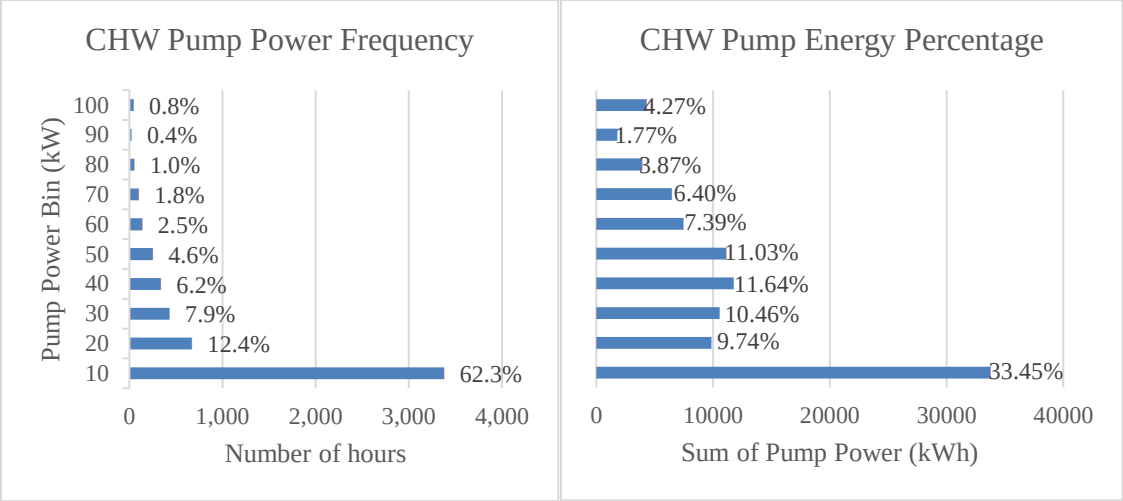

Figure 44. VA-Brooklyn Building CHW pump power and energy distribution statistical analysis.

Similarly, Figure 45 shows hourly HHW pump power from September 13, 2016, to September 12, 2017. Figure 46 shows the HHW pump power frequency and energy consumption percentage in each pump power bin.

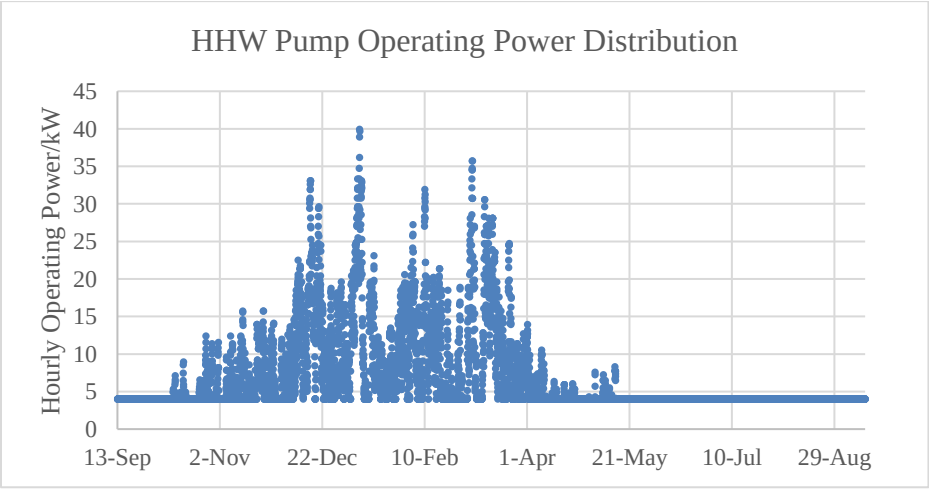

Figure 45. VA-Brooklyn Building HHW pump power hourly value distribution.

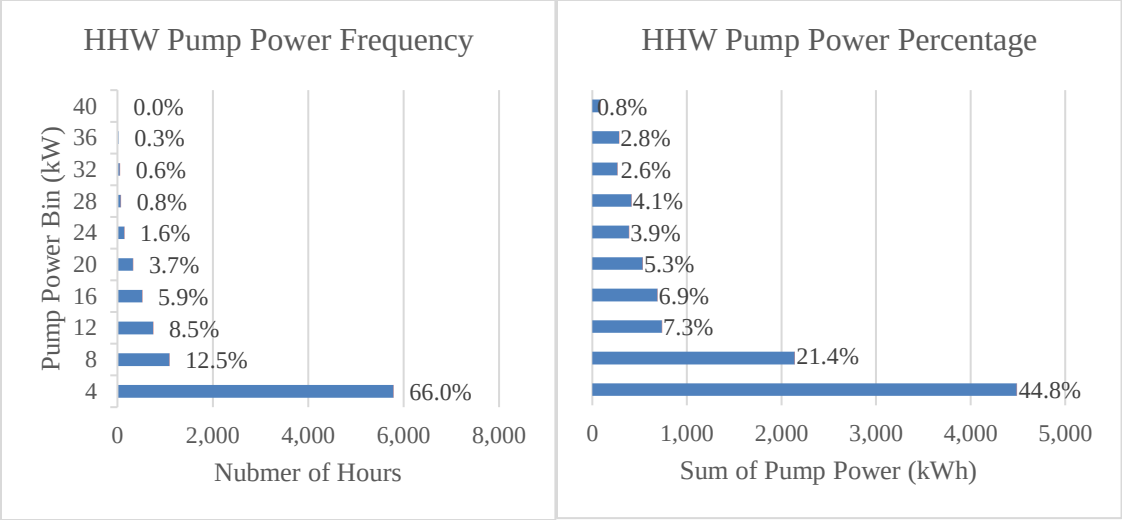

Figure 46. VA-Brooklyn Building HHW pump power distribution statistical analysis.

After a multiple pump size system is applied, the hourly pump energy consumption is calculated and compared to the consumption data of the original pump system. Energy and cost savings for the multiple pump size system are obtained and shown in Table 23.

Table 23. Energy and cost saving results for the multiple pump size system in VA-Brooklyn Building.

Item	kWh Savings	$ Savings	Baseline Annual kWh Consumption	Savings Percentage
CHW Pump	32,483	$3,024	100,971	32.1%
HHW Pump	15,383	$1,432	57,472	26.7%

As an engineering application, the estimated total installation cost of a 10 hp CHW pump and a 4 hp HHW pump are around $3,844.62 and $2,869.62, respectively. A simple payback analysis is shown in Table 24. The overall simple payback is one and a half years. Comparing VA-Brooklyn to TSC, it is more economically feasible when the pumps run more hours on the minimum power rate and have a larger horsepower.

Table 24. Simple payback periods for multiple pump size system upgrades in VA-Brooklyn Building.

Pump Installation	Minimum Flowrate	Installation Cost	Annual Cost Savings	Simple Pay Back (year)
CHW Pump	30%	$3,844.62	$3,024	1.3
HHW Pump	30%	$2,869.62	$1,432	2
Total	-	$6,714.24	$4,456	1.5

The traditional parallel pumping system cannot cover low space loads efficiently due to the minimum pump speed limitation. The multiple pump sizes with a VFD system is proposed to meet system loads with significant variation more efficiently. Two case studies of building level pumping systems show that upgrading to multiple pump sizes with a VFD system can save 10% - 32% of the pumping power per year with a simple payback of 1.5 - 7.1 years. Note that if only the CHW pumping system is upgraded, then the simple payback will be 1.3 - 5 years. The author concludes that upgrading to multiple pump sizes with the VFD system can be a cost-effective building energy conservation

measure in some cases, especially for pumping systems with large horsepower and large load variations.

Two identical parallel pumps are typically configured in the HVAC systems in the interest of system reliability and control/maintenance convenience. The multiple pump sizes with VFD configuration does not affect the system reliability. If the smaller capacity pump is down, the system can always switch back to the mode with two identical pumps. On the control side, the smaller capacity pump works only when the required CHW/HHW flow rate is lower than 20% - 30% of the designed flow rate, which can be controlled independently. Thus, adding an extra pump will not cause additional problems.

A similar approach may apply to a building air conditioning fan system to save fan energy. However, potential savings may be limited by minimum flow requirements in the zones, and the installation of additional ducting may be cost-prohibitive.

4.5 System Units Arrangement Optimization

4.5.1 System Parameters and Possible Arrangements

In this section, all models with specific parameters are integrated and all possible arrangements listed in Table 3 are evaluated to maximize the temperature difference between the geothermal fluid supply and return.

In DEH and GDHS systems, the heat exchanger effectiveness limits the geothermal fluid supply temperature [147]. For a DEH configuration shown in Figure 47, given a liquid to air heat transfer effectiveness ε_{w-a} of 0.87, the required minimum

geothermal fluid supply temperature, T_6, also noted as $T_{DEH,geo,supply}$, is 150°F, which is 10°F higher than the desire scavenging air temperature before it goes to the regenerator.

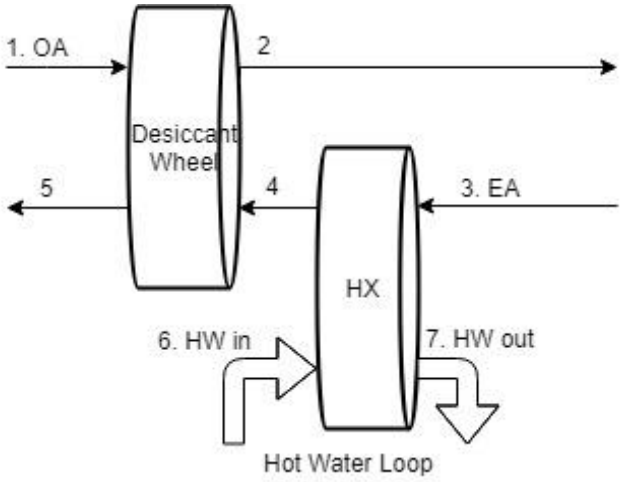

Figure 47. Simplified DEH system diagram.

$$\varepsilon_{w-a} = \frac{T_3 - T_4}{T_3 - T_6} \tag{111}$$

The thermodynamic limitation for the DEH geothermal fluid temperature drop ΔT_{DEH} can be solved as a function of $T_{DEH,geo,supply}$, as shown in Equation (112).

$$\Delta T_{DEH} = \frac{87}{100}(T_{DEH,geo,supply} - T_{DEH,EA,in}) \tag{112}$$

Similarly, for a GDHS configuration shown in Figure 20, given a liquid to liquid heat transfer effectiveness ε_{w-w} of 0.90, the required minimum geothermal fluid supply temperature, $T_{GDHS,geo,supply,min}$, as a function of OAT, is shown in Equation (114).

When the heating load is low, the required geothermal fluid temperature could be as low as 137°F, while it is required to be as high as 183°F with high heating loads.

$$\varepsilon_{w-w} = \frac{HWRT - HWST}{HWRT - T_{geo,supply}} \tag{113}$$

$$T_{GDHS,geo,supply,min} = \begin{cases} 183°F, T_{OA} \leq 20°F \\ \frac{-83 \cdot T_{OA} + 16465}{81}, 20°F < T_{OA} < 65°F \\ 137°F, T_{OA} \geq 65°F \end{cases} \tag{114}$$

The thermodynamic limitation for the geothermal fluid temperature drop ΔT_{GDHS} can be solved as a function of $T_{GDHS,geo,supply}$ and OAT, as shown in Equation (115).

$$\Delta T_{GDHS} = \begin{cases} \frac{9}{10}(T_{GDHS,geo,supply} - 155), T_{OA} \leq 20°F \\ \frac{9}{10}(T_{GDHS,geo,supply} - \frac{-7T_{OA} + 1535°F}{9}), 20°F < T_{OA} < 65°F \\ \frac{9}{10}(T_{GDHS,geo,supply} - 120), T_{OA} \geq 65°F \end{cases} \tag{115}$$

Table 25 lists the geothermal fluid supply temperature requirements and possible temperature drop for each system. Based on the geothermal fluid supply temperature requirements and the possible temperature drop of all these three systems, the ABS system and the GDHS system should be in parallel and the DEH system should be in parallel or in series following the ABS system or the GDHS system.

Table 25. Geothermal fluid supply temperature requirements by each system.

System	Geothermal Fluid Supply Temperature (°F)	Geothermal Fluid Temperature drop (°F)
ABS	175 - 212°F	19°F by design with a range of 5 - 32°F
DEH	>150°F	$\Delta T_{DEH} = \frac{87}{100}(T_{DEH,geo,supply} - T_{DEH,EA,in})$
GDHS	$\begin{cases} 183°F, T_{OA} \leq 20°F \\ \frac{-83 \cdot T_{OA} + 16465}{81}, \\ 20°F < T_{OA} < 65°F \\ 137°F, T_{OA} \geq 65°F \end{cases}$	$\begin{cases} \frac{9}{10}(T_{GDHS,geo,supply} - 155), T_{OA} \leq 20°F \\ \frac{9}{10}\left(T_{GDHS,geo,supply} - \frac{-7T_{OA} + 1535°F}{9}\right), \\ 20°F < T_{OA} < 65°F \\ \frac{9}{10}(T_{GDHS,geo,supply} - 120), T_{OA} \geq 65°F \end{cases}$

Therefore, these three systems cannot be in series and the possible arrangements are cut down to a few options for comparison listed below. A typical arrangement example, option F, is given in Figure 48.

A. ABS only. The weighted COP over a year is calculated as 0.467. The major limitation for ABS only is the maximum temperature drop of 32°F.
B. DEH only. The weighted COP of a DEH system over a year in the GSC case study is around 0.80, which is higher than an ABS system's rated COP of 0.76 and an average COP of 0.467. The geothermal fluid could be dropped below 140°F. Thus, the DEH system only should be more efficient than Case A. However, it can only cover the latent load on the DOAS system, and the geothermal system is not able to be independent.

C. GDHS only. The overall efficiency is as high as 0.97. However, during the peak loads, the maximum temperature drop allowed is less than 36°F. Furthermore, it covers only the heating load while the cooling load constitutes more than 90% of the total loads in College Station.

D. 3 loops—each system is supplied individually and directly from the heat source.

E. 2 loops—ABS is in series with DEH, while in parallel with GDHS.

F. 2 loops—GDHS is in series with DEH, while in parallel with ABS.

G. 1 loop—ABS and GDHS are in parallel, and then in series with DEH.

H. Different arrangements are adopted during peak load and base load. During peak load, option E - H; during base load, 1 loop—DEH and GDHS are in parallel, and then in series with ABS (ABS in front).

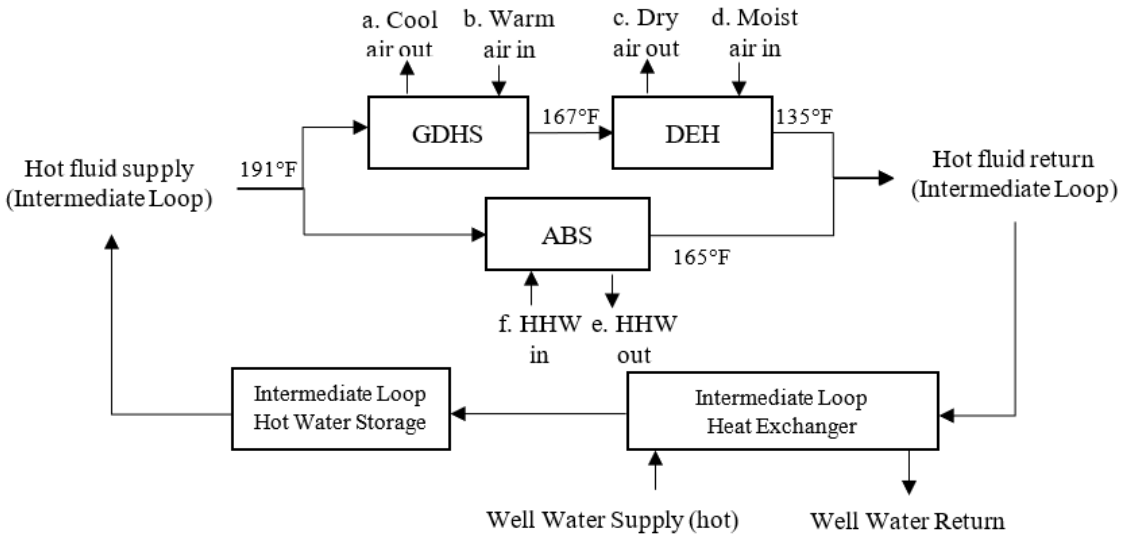

Figure 48. Case F - a typical arrangement of a cascaded flow path with all three systems.

4.5.2 Simulated Load Profile by Outside Air Temperature

The overall system efficiencies of these three systems largely vary by the zone heating/cooling loads and are quite different from each other. Meanwhile, the interior zone loads are fairly constant per space functions and the perimeter zone loads are dominated by the outside air temperature (OAT). Thus, the load profile could be treated as a simplified function of OAT.

Specifically, the ventilation sensible and latent loads for the interior zones are calculated by Equations (116) to (118) [148]. The loads for exterior zones or any other zones share the same set of equations with the subscript 'in' replaced by 'ex' or another appropriate subscript.

$$q_{S,V,in} = c_p \rho \dot{V}_{OA,in}(T_{OA} - T_{RA}) \quad (116)$$

$$q_{L,V,in} = L_{vaporization}\rho\dot{V}_{OA,in}(w_{OA} - w_{RA}) \quad (117)$$

$$q_{V,in} = q_{S,V,in} + q_{L,V,in} \quad (118)$$

where $q_{S,V,in}$ $q_{S,V,in}$ is the interior zone sensible ventilation load per unit area (kW/m^2 or $\frac{MMBtu/hr}{ft^2}$), $q_{L,V,in}$ is the interior zone latent ventilation load per unit area (kW/m^2 or $\frac{MMBtu/hr}{ft^2}$), ρ is the density (kg/m^3 or lb/ft^3), $L_{vaporization}$ is the latent heat (J/kg or Btu/lb), c_p is the specific heat ($J/(kg \cdot ℃)$ or $Btu/(lb \cdot °F)$), $\dot{V}_{OA}$ is the outside air flowrate per unit area ($\frac{m^3/s}{m^2}$ or cfm/ft^2), T is the temperature (℃ or °F), and w is the humidity ratio (kg_w/kg_{air} or lb_w/lb_{air}). Note that units need to be consistent during the numerical calculation.

Based on the definition of the building's total load, the total load for the interior zone ($Q_{BSL,in}$) and the exterior zone ($Q_{BSL,in}$) are presented by Equations (119) and (120).

$$Q_{BSL,in} = (q_{env,in} + q_{gain,in} + q_{V,in})A_{in} \quad (119)$$

$$Q_{BSL,ex} = (q_{env,ex} + q_{gain,ex} + q_{V,ex})A_{ex} \quad (120)$$

where A_{ex} is the exterior zone area, and A_{in} is the interior zone area, $q_{env,in}$ is the interior zone envelope load, $q_{gain,in}$ is the interior zone internal gains, $q_{env,ex}$ is the exterior zone envelope load, and $q_{gain,ex}$ is the exterior zone internal gain. Note that $Q_{BSL,ex}$ represents cooling load when the value is positive, while a negative value means it is heating load.

A four-parameter change-point model is adopted here to express building heating and cooling loads separately as a function of OAT [139, 149]. However, the RELLIS campus consumption data and detailed building information are not available at this point. In the perspective of the general well geothermal fluid application, the load profile of the GSC Building is introduced to estimate the scaled-down Texas A&M RELLIS Campus load. The daily CHW and HHW consumption during 2018/5/1 – 2019/4/30 are analyzed and listed in Figure 49 and Figure 50. The total building square footage of GSC is 202,467 ft^2 and the yearly total CHW energy used is 9,950 MMBtu/year. Thus, the yearly CHW energy use intensity (EUI) 49.1 $kBtu/ft^2$. Similarly, the yearly HHW energy used is 947 MMBtu/year and HHW EUI is 4.68 $kBtu/ft^2$, which is around 1/10 of the CHW EUI.

After applying the four-parameter model, the cooling and heating load are expressed as a piecewise function of OAT, as shown in Equations (121) and (122).

$$Q_{cooling}(kBtu/hour) = \begin{cases} 0.3591 \cdot T_{OA} - 1.156, & T_{OA} < 58.6°F \\ 1.106 \cdot T_{OA} - 44.92, & T_{OA} \geq 58.6°F \end{cases} \quad (121)$$

$$Q_{heating}(kBtu/hour) = \begin{cases} -0.4845 \cdot T_{OA} + 28.12, & T_{OA} < 51.7°F \\ -0.0538 \cdot T_{OA} + 5.854, & T_{OA} \geq 51.7°F \end{cases} \quad (122)$$

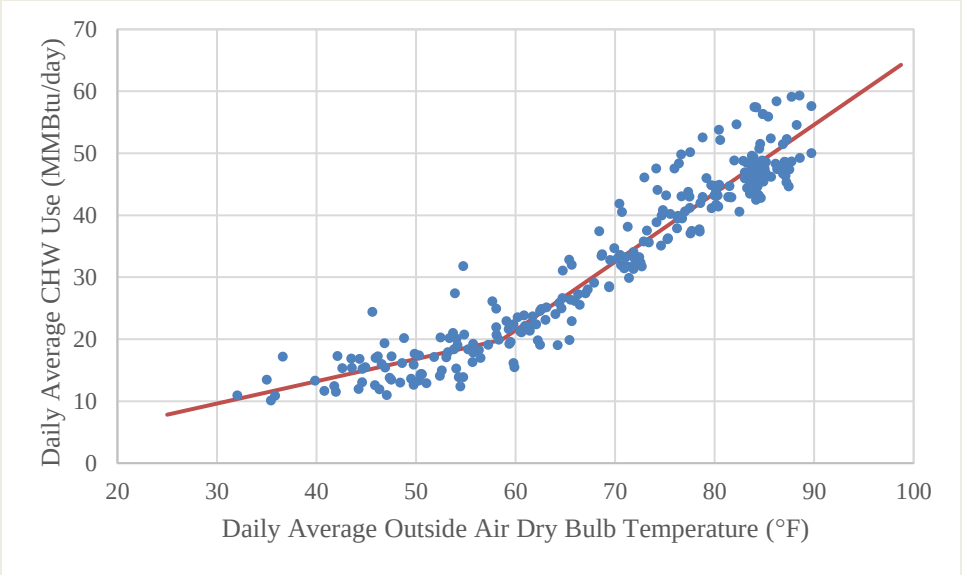

Figure 49. 4P model for daily CHW consumption of the GSC Building cooling load.

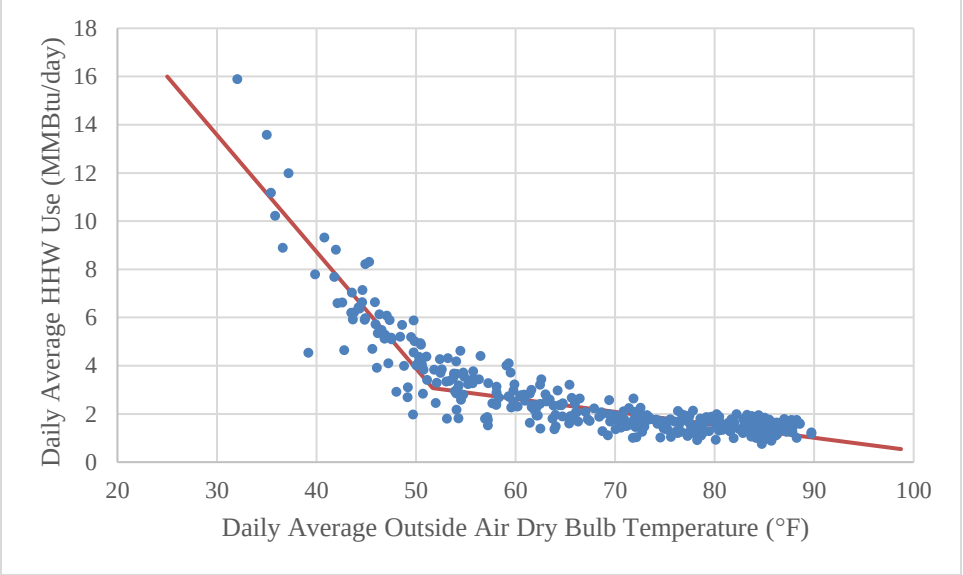

Figure 50. 4P model for daily HHW consumption of the GSC Building heating load.

The estimated total sensible load could be expressed in Equation (123), calculated as 6,460 kBtu/year while the latent load is listed in Equation (124), calculated as 3,490 kBtu/year. Thus, the latent load takes around 35.1% of the total cooling load. This percentage increases when the outside air percentage go up. For example, a SDVAV system with 100% outside air will have a larger ratio of the latent load to the zone total loads.

$$Q_{Sensible} = 0.3591 \cdot T_{OA} - 1.156, \text{for all } T_{OA} \tag{123}$$

$$Q_{Latent} = 0.01578 \cdot T_{OA} - 0.6408, T_{OA} \geq 58.6°F \tag{124}$$

Assuming that the maximum heating load occurs when OAT goes to its minimum value, 26°F, and the maximum cooling load occurs when OAT goes to its maximum value, 104°F, we have

$$PLR_{cooling} = \frac{Q_{cooling}}{Q_{cooling,max}} \tag{125}$$

$$PLR_{heating} = \frac{Q_{heating}}{Q_{heating,max}} \tag{126}$$

Combining Equations (121) - (126), the relations between PLR and OAT become

$$PLR_{cooling} = \begin{cases} 0.005122 \cdot T_{OA} - 0.01649, & T_{OA} < 58.6°F \\ 0.01578 \cdot T_{OA} - 0.6408, & T_{OA} \geq 58.6°F \end{cases} \tag{127}$$

$$PLR_{heating} = \begin{cases} -0.03121 \cdot T_{OA} + 1.812, & T_{OA} < 51.7°F \\ -0.003466 \cdot T_{OA} + 0.3771, & T_{OA} \geq 51.7°F \end{cases} \tag{128}$$

Since COP_{ABS} is a function of PLR, we can obtain COP_{ABS} as a function of OAT. The bin method is applied here to analyze loads for different outside air conditions. Table 26 lists the PLR, COP, and HWST for all three systems.

A weighted COP_{ABS} is calculated as 0.48 using Equation (129). Furthermore, if taking the economizer mode into account, free cooling is applied when OAT is lower than 65°F and the weighted COP_{ABS} would become 0.55.

Table 26. Systems PLR and COP under different outside air conditions.

Weather Bin Data			**ABS**		**DEH**	**GDHS**	
$\mathbf{N_{bin}}$	$\mathbf{T_1}$	$\boldsymbol{w_1}$	**Cooling PLR**	**Cooling COP**	$\mathbf{COP_{DW}}$	**Heating PLR**	**HWST**
163	32	0.0025	14.7%	0.296	-	0.813	168
220	37	0.0033	17.3%	0.317	-	0.657	163
350	42	0.0042	19.9%	0.337	-	0.501	158
483	47	0.0050	22.4%	0.356	-	0.345	153
577	52	0.0059	25.0%	0.375	-	0.197	148
802	57	0.0073	27.5%	0.394	0.149	0.180	143
905	62	0.0088	33.8%	0.435	0.306	0.162	138
866	67	0.0111	41.6%	0.483	0.459	0.145	135
1197	72	0.0130	49.5%	0.525	0.764	0.128	135
1402	77	0.0158	57.4%	0.560	1.119	0.110	135
779	82	0.0161	65.3%	0.590	1.277	0.093	135
446	87	0.0156	73.2%	0.614	1.412	0.076	135
408	92	0.0159	81.1%	0.631	1.705	0.058	135

Table 26 (Continued).

Weather Bin Data			ABS		DEH	GDHS	
N_{bin}	T_1	w_1	Cooling PLR	Cooling COP	COP_{DW}	Heating PLR	HWST
129	97	0.0144	89.0%	0.643	1.734	0.041	135
33	102	0.0123	96.9%	0.649	1.585	0.024	135

$$COP_{ABS} = \frac{\sum N_i COP_{ABS,i}}{\sum N_i} \quad (129)$$

Similarly, a weighted COP_{DEH} is calculated as 0.81. It is worth mentioning that when the outside air humidity ratio is lower than 0.009 lb_w/lb_{air}, the desiccant wheel should not be operated, although the desiccant wheel system can further dry the outside air. Thus, in practice, the desiccant wheel only runs when OAT is higher than 65°F in College Station. And the weighted COP_{DEH} becomes 1.01.

4.5.3 System Performance Analysis and Arrangement Optimization

In this section, all models with specific parameters are combined, and the system performances are evaluated to maximize the cooling/heating energy output and the geothermal fluid temperature difference between the geothermal fluid supply and return. As analyzed in section 4.5.2, the system COP is highly related to the PLR, therefore whether the integrated system capacity matches the building loads will result in different optimized system arrangements and performance. Two typical cases are treated in this

dissertation: the building loads are so large that the integrated system only needs to run at its full capacity, and the building loads match the system capacity well.

Integrated System Operating at Full Capacity

As discussed in section 4.13, the total geothermal energy output would be 16.99 MMBtu/day with the assumption of 50°F temperature differences. For a building with large square footage and loads, this energy output is even lower than its minimum daily energy consumption. In this ideal case, the ABS system runs at its rated COP of 0.76 with a designed geothermal fluid return of 172°F, regardless of the outside air condition. The $\mathrm{COP_{DEH}}$ still varies with OAT, and so does the geothermal supply temperature required by GDHS.

Case A: ABS only

In the ABS system, the supply geothermal fluid temperature is 191°F based on Equation (60), varying the temperature difference has an influence on the absorption chiller output $\dot{\mathrm{Q}}_{\mathrm{eva}}$. Similar to Equation (72), the absorption chiller COP correction factor $\mathrm{Correct_{ABS}}$ would be expressed as a function of geothermal fluid temperature difference $\Delta \mathrm{T_{ABS}}$ between supply and return (°F), where $\Delta \mathrm{T_{ABS}} \in (19°\mathrm{F}, 32°\mathrm{F})$.

$$\mathrm{Correct_{ABS}} = \frac{\dot{\mathrm{Q}}_{\mathrm{eva}}}{\dot{\mathrm{Q}}_{\mathrm{eva,design}}} = -0.009563 \cdot \Delta \mathrm{T_{ABS}} + 1.182 \tag{130}$$

$$\mathrm{COP_{ABS}} = \mathrm{COP_{normal}} \cdot \mathrm{Correct_{ABS}} \tag{131}$$

Thus, the absorption chiller cooling output $\dot{\mathrm{Q}}_{\mathrm{ABS}}$ becomes

$$\dot{\mathrm{Q}}_{\mathrm{ABS}} = \dot{\mathrm{Q}}_{\mathrm{gen}} \cdot \mathrm{COP_{ABS}} \tag{132}$$

Combining Equations (130) - (132), we build a relation between $\dot{Q}_{ABS}$ and ΔT_{ABS} below.

$$\dot{Q}_{ABS} = \frac{V_{HW}(gpm) \cdot \Delta T_{ABS}}{2{,}000} \cdot COP_{normal} \cdot (-0.009563 \cdot \Delta T_{ABS} + 1.182) \tag{133}$$

$\dot{Q}_{ABS}$ increases as ΔT_{ABS} increases in the range of 19 - 32°F, thus, the maximum $\dot{Q}_{ABS}$ is obtained.

$$\begin{aligned} \dot{Q}_{ABS,max} &= \frac{29.17 gpm \cdot 32°F}{2{,}000} \cdot 0.76 \cdot (-0.009563 \cdot 32°F + 1.182) \\ &= 0.311 \frac{MMBtu}{hr} (25.89 \text{ tons}) \end{aligned} \tag{134}$$

The ABS system runs all the year around for N=8,760 hours, thus, its yearly CHW output would be

$$Q_{ABS,max,year} = \dot{Q}_{ABS,max} \cdot N_{ABS} = 2{,}724 \text{ MMBtu} \tag{135}$$

Case B: DEH only

The DEH system only eliminates the latent load on cooling coils of the DOAS system and has nothing to do with PLR as long as the latent load exceeds the DEH capacity. Meanwhile, the DEH system is designed to be bypassed when the outside air humidity ratio goes below 0.009 lb_w/lb_{air} in the desired operation, so COP_{DEH} is taken as 1.014 for eliminating latent loads.

$$\dot{Q}_{DEH} = \frac{V_{HW}(gpm) \cdot \Delta T_{DEH}}{2{,}000} \cdot COP_{DEH} \tag{136}$$

Combining Equations (112) and (136), we have

$$\dot{Q}_{DEH} = \frac{29.17\text{gpm}}{2{,}000} \cdot \frac{87}{100} (T_{DEH,geo,supply} - T_{DEH,EA,in}) \cdot 1.014 \quad (137)$$

If the geothermal fluid is directly supplied to DEH with a temperature of 191°F, then ΔT_{DEH} is solved for each bin along with the maximum $\dot{Q}_{ABS}$ in Table 27. The DEH runs for $N = 5{,}260$ hours when the outside air latent loads exist, thus, its yearly CHW output would be

$$Q_{DEH,max,year} = \frac{V_{HW}(\text{gpm})}{2{,}000} \cdot \sum \frac{87}{100} \cdot \left(T_{DEH,geo,supply} - T_{DEH,EA,in,i}\right) \cdot N_i \cdot COP_{DEH,i} = 5{,}374 \text{ MMBtu} \quad (138)$$

Table 27. Geothermal fluid temperature difference between supply and return in the DEH system.

N_{bin}	T_1	w_{OA}	$T_{DEH,EA,in}$	$T_{geo,supply}$	$T_{geo,return}$	ΔT_{DEH}	COP_{DEH}	$Q_{DEH,bin}$
-	°F	lb_w/lb_{air}	°F	°F	°F	°F	-	MMBtu
163	32	0.0025	75.3	-	-	-	-	-
220	37	0.0033	79.8	-	-	-	-	-
350	42	0.0042	83.9	-	-	-	-	-
483	47	0.005	87.8	-	-	-	-	-
577	52	0.0059	91.6	-	-	-	-	-
802	57	0.0073	96	-	-	-	-	-
905	62	0.0088	100.1	-	-	-	-	-
866	67	0.0111	105	191	116.2	74.8	0.459	433.8

Table 27 (Continued).

N_{bin}	T_1	w_{OA}	$T_{DEH,EA,in}$	$T_{geo,supply}$	$T_{geo,return}$	ΔT_{DEH}	COP_{DEH}	$Q_{DEH,bin}$
-	°F	lb_w /lb_{air}	°F	°F	°F	°F	-	MMBtu
1197	72	0.013	108.9	191	119.6	71.4	0.764	952.7
1402	77	0.0158	113.5	191	123.6	67.4	1.119	1,542.8
779	82	0.0161	115.4	191	125.2	65.8	1.277	954.3
446	87	0.0156	116.5	191	126.2	64.8	1.412	595.3
408	92	0.0159	118.3	191	127.8	63.2	1.705	641.7
129	97	0.0144	118.6	191	128.0	63.0	1.734	205.5
33	102	0.0123	118.2	191	127.7	63.3	1.585	48.3

Case C: GDHS only

In the GDHS system, the energy efficiency is assumed to be a constant as 0.97. If the geothermal fluid is directly supplied to DEH with a temperature of 191°F, the corresponding ΔT_{GDHS} is solved in each bin, as listed in Table 28.

Table 28. Geothermal fluid temperature difference between supply and return in the GDHS system.

N_{bin}	T_1	$T_{GDHS,geo,supply}$	$T_{GDHS,geo,return}$	ΔT_{GDHS}	$Q_{GDHS,bin}$
-	°F	°F	°F	°F	MMBtu
163	32	191	150.2	40.8	104.5
220	37	191	146.7	44.3	153.2

Table 28 (Continued).

N_{bin}	T_1	$T_{GDHS,geo,supply}$	$T_{GDHS,geo,return}$	ΔT_{GDHS}	$Q_{GDHS,bin}$
-	°F	°F	°F	°F	MMBtu
350	42	191	143.2	47.8	263.0
483	47	191	139.7	51.3	389.5
577	52	191	136.2	54.8	497.0
802	57	191	132.7	58.3	735.0
905	62	191	129.2	61.8	879.2
866	67	191	127.1	63.9	782.9
1197	72	191	127.1	63.9	1,082.1
1402	77	191	127.1	63.9	1,267.4
779	82	191	127.1	63.9	704.2
446	87	191	127.1	63.9	403.2
408	92	191	127.1	63.9	368.8
129	97	191	127.1	63.9	116.6
33	102	191	127.1	63.9	29.8

Then the maximum yearly HHW energy output Q_{GDHS} is obtained.

$$Q_{GHDS,max,year} = \frac{V_{HW}(gpm) \cdot \eta_{GDHS}}{2{,}000} \sum N_i \Delta T_{GDHS} = 7{,}474 \text{ MMBtu} \quad (139)$$

Thus, GDHS only can produce more energy output than DEH only or ABS only. The ABS system should be excluded in the optimized arrangement because it has the lowest COP under all kinds outside air conditions.

Case D: 3 loops—each system is supplied individually and directly from the heat source

Since DEH has a higher COP value than GDHS when OAT is higher than 75°F, DEH and GDHS can be combined to obtain the maximum energy output. Specifically, GDHS is operated when OAT is less than 75°F, otherwise, DEH is operated. Figure 51 shows the optimized arrangement flow path. Table 29 lists the energy output by the optimized arrangement in the case that systems run at their full capacity. The yearly average geothermal fluid temperature drop is 60.6°F and the yearly total energy output is 8,572 MMBtu, which consists of 4,584 MMBtu heating energy and 3,988 MMBtu cooling energy saving.

Table 29. Geothermal fluid temperature analysis when the integrated system runs at full capacity.

N_{bin}	T_1	$T_{geo,supply}$	$T_{geo,return}$	System Operated	Q_{bin}
-	°F	°F	°F	-	MMBtu
163	32	191	150.2	GDHS	94.1
220	37	191	146.7	GDHS	137.9
350	42	191	143.2	GDHS	236.7
483	47	191	139.7	GDHS	350.5
577	52	191	136.2	GDHS	447.3
802	57	191	132.7	GDHS	661.5
905	62	191	129.2	GDHS	791.3
866	67	191	127.1	GDHS	782.9

Table 29 (Continued).

N_{bin}	T_1	$T_{geo,supply}$	$T_{geo,return}$	System Operated	Q_{bin}
-	°F	°F	°F	-	MMBtu
1197	72	191	127.1	GDHS	1,082.1
1402	77	191	125.2	DEH	1,542.8
779	82	191	126.2	DEH	954.3
446	87	191	127.8	DEH	595.3
408	92	191	128.0	DEH	641.7
129	97	191	127.7	DEH	205.5
33	102	191	125.2	DEH	48.3

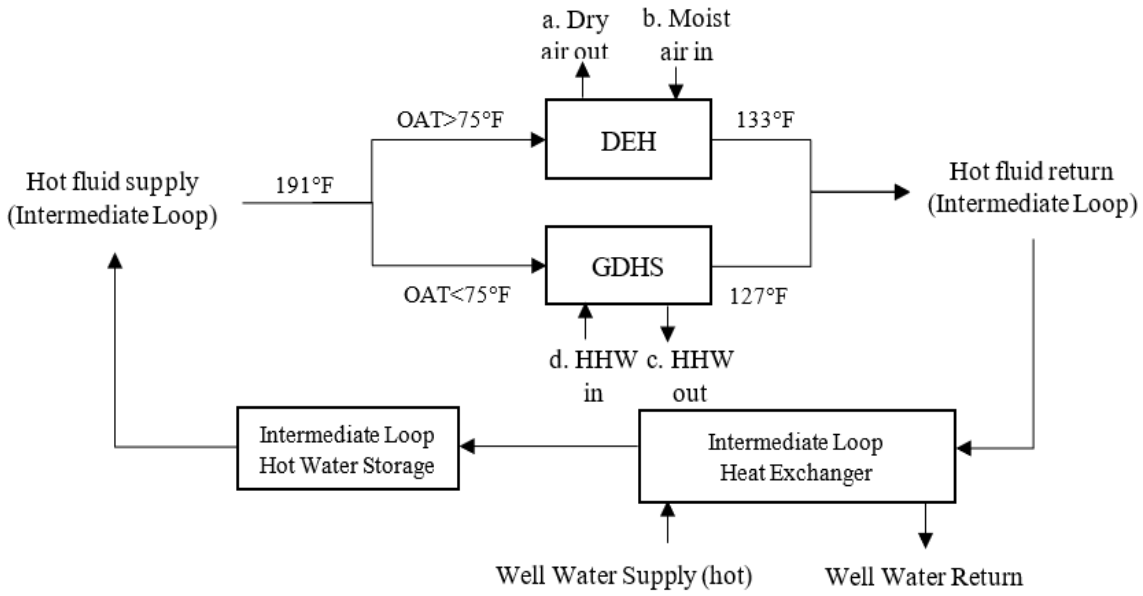

Figure 51. Optimized arrangement of a cascaded flow path when systems run at their full capacity.

Integrated System Matches the Building Loads

One of the research goals is to determine the configuration of the optimized geothermal plant for a district heating and cooling system using low-grade geothermal fluid. Assuming that the proposed geothermal well system has a considerable scale and can cover a large building or even a building campus. The ABS system has to be operated to cover the building sensible cooling loads and part of the latent load, while the DEH system eliminates most of the building latent load and the GDHS system covers the building heating load. The typical load profile of a campus office building, called GSC, is used here to determine the system arrangements and the plant configurations.

Case E: 2 loops—ABS is in series with DEH, while in parallel with GDHS

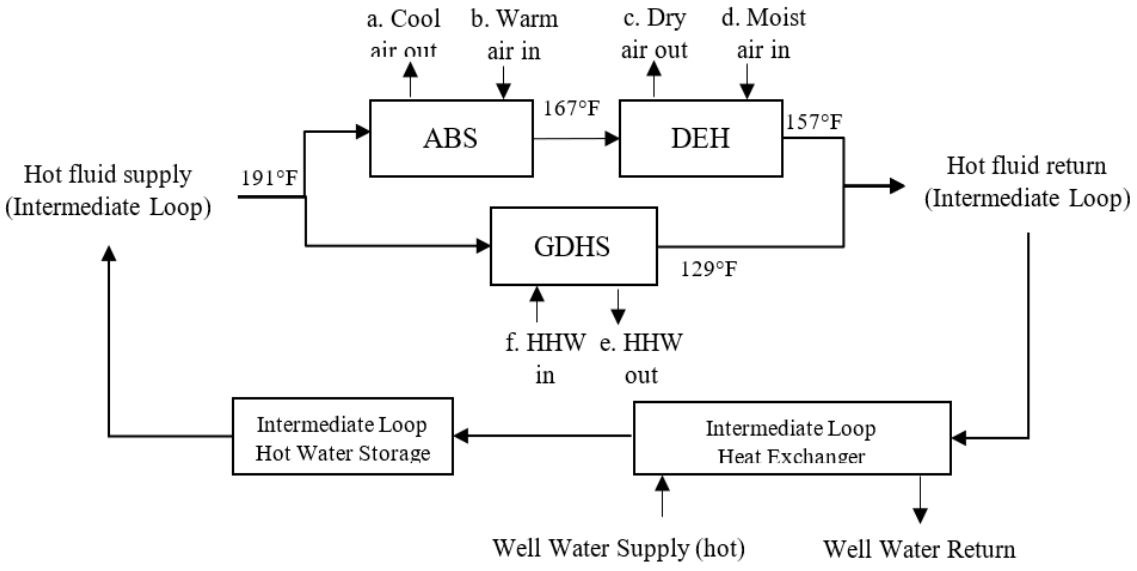

Figure 52. The cascaded flow path of case E arrangement.

Figure 52 shows the cascaded flow path for case E. Since the DEH system eliminates most of the latent load on the building DOAS system, the building peak cooling load is reduced, and the PLR is increased in each bin. And the adjusted PLR equation is calculated only based on sensible load.

$$\mathrm{PLR}_{\mathrm{cooling,adjusted}} = 0.009923 \cdot \mathrm{T}_{\mathrm{OA}} - 0.03195, \text{for all } \mathrm{T}_{\mathrm{OA}} \tag{140}$$

The maximum hourly cooling energy output from the ABS system is

$$\mathrm{Q}_{\mathrm{ABS,max,hour}} = \frac{\mathrm{V}_{\mathrm{HW},1}(\mathrm{gpm}) \cdot \Delta\mathrm{T}_{\mathrm{ABS}}}{2{,}000} \cdot \mathrm{COP}_{\mathrm{ABS}} \tag{141}$$

In the DEH system bin analysis, the ratio of the cooling load avoided by DEH to the cooling load remaining in each bin, $\mathrm{r}_{\mathrm{DEH/ABS}}$ is obtained by the enthalpy analysis in Table 30.

Table 30. Bin analysis on ratios of the cooling load avoided by the DEH system to the cooling load remaining.

$\mathbf{N_{bin}}$	$\mathbf{T_1}$	$\mathbf{h_{OA}}$	$\mathbf{h_{before\ c/c}}$	$\mathbf{h_{after\ c/c}}$	**Cooling load avoided** $\mathbf{h_{OA} - h_{before\ c/c}}$	**Cooling load remaining** $\mathbf{h_{OA} - h_{after\ c/c}}$	$\mathbf{r_{DEH/ABS}}$
-	°F	Btu/lb	Btu/lb	Btu/lb	Btu/lb	Btu/lb	-
866	67	28.2	24.3	127.1	3.9	5.1	0.771

Table 30 (Continued).

N_{bin}	T_1	h_{OA}	$h_{before\ c/c}$	$h_{after\ c/c}$	Cooling load avoided $h_{OA} - h_{before\ c/c}$	Cooling load remaining $h_{OA} - h_{after\ c/c}$	$r_{DEH/ABS}$
-	°F	Btu/lb	Btu/lb	Btu/lb	Btu/lb	Btu/lb	-
1197	72	31.5	25.7	127.1	5.8	5.3	1.091
1402	77	35.8	28.5	125.2	7.3	6.4	1.127
779	82	37.3	29.7	126.2	7.7	7.0	1.094
446	87	38.0	29.9	127.8	8.1	7.2	1.131
408	92	39.6	30.6	128.0	9.0	7.6	1.192
129	97	39.2	30.1	127.7	9.1	7.1	1.271
33	102	38.1	29.6	125.2	8.4	7.2	1.170

Then the maximum hourly latent energy that needed be avoided by the DEH system would be

$$Q_{DEH,max,hour} = Q_{ABS,max,hour} \cdot r_{DEH/ABS} \tag{142}$$

Based on the load profile described in section 4.5.2, the maximum cooling to heating load ratio, $r_{cooling/heating}$, would be

$$r_{cooling/heating} = \frac{Q_{cooling,max}}{Q_{heating,max}} = \frac{1.106 \cdot T_{OA,max} - 44.92}{-0.4845 \cdot T_{OA,min} + 28.12} = 3.7 \tag{143}$$

Then the maximum hourly heating energy output from the GDHS system would be

$$Q_{GDHS,max,hour} = \frac{Q_{ABS,max,hour} + Q_{DEH,max,hour}}{r_{cooling/heating}} \quad (144)$$

Meanwhile, $Q_{GDHS,max,hour}$ can be expressed as a function of geothermal fluid flowrate.

$$Q_{GDHS,max,hour} = \frac{V_{HW,2}(gpm) \cdot \Delta T_{GDHS}}{2{,}000} \cdot \eta_{GDHS} \quad (145)$$

In order to match the load profile well, we have

$$V_{tot}(gpm) = V_{HW,1} + V_{HW,2} = 29.17 \text{ gpm} \quad (146)$$

The geothermal fluid flowrate supplied to each system is variable, and $V_{HW,1}$ and $V_{HW,2}$ are solved with each bin's inputs by Equations (146) and (147). Since the maximum cooling load happens while the heating load reaches its minimum value and vice versa, the system output would be improved. Note that for a typical single duct variable air volume (SDVAV) system with the return air of an office building locating in College Station, the latent load takes around one-third of the building total load. The latent load avoided by the DEH system here is the upper limit value in an extreme case of an air conditioning system with 100% outside air.

$$V_{HW,1} = V_{tot} \cdot \frac{1}{1 + \frac{\frac{Q_{ABS,hour,bin} + Q_{GDHS,hour,bin}}{PLR_{cooling} \cdot r_{cooling/heating}}}{\frac{Q_{GDHS,hour,bin}}{PLR_{heating}}}} \quad (147)$$

Table 31. Geothermal fluid temperature analysis for case E with variable geothermal flowrate to each system.

N_{bin}	T_1	ΔT_{ABS}	Q_{ABS}	ΔT_{DEH}	Q_{DEH}	$T_{DEH,geo,return}$	ΔT_{GDHS}	Q_{GDHS}	$V_{HW,1}$	$V_{HW,2}$	$T_{GDHS,geo,return}$
-	°F	°F	MMBtu	°F	MMBtu	°F	°F	MMBtu	gpm	gpm	°F
163	32	22.3	14.3	-	-	168.7	38.3	28.8	19.67	9.50	152.7
220	37	21.7	22.7	-	-	169.3	40.5	31.4	21.90	7.27	150.5
350	42	21.3	41.4	-	-	169.7	42.9	38.1	23.94	5.23	148.1
483	47	21.0	64.5	-	-	170.0	45.5	36.2	25.77	3.40	145.5
577	52	21.0	85.8	-	-	170.0	48.4	24.7	27.35	1.82	142.6
802	57	21.8	131.5	-	-	169.2	53.7	31.3	27.67	1.50	137.3
905	62	22.6	162.2	-	-	168.4	61.8	29.9	28.07	1.10	129.2
866	67	23.3	168.4	22.8	129.9	144.8	63.9	14.9	28.61	0.56	127.1
1197	72	24.3	251.0	20.8	273.9	145.9	63.9	13.1	28.82	0.35	127.1
1402	77	25.3	315.4	15.7	355.6	150.0	63.9	9.8	28.95	0.22	127.1
779	82	26.5	187.1	14.2	204.7	150.3	63.9	3.8	29.01	0.16	127.1
446	87	27.7	113.9	14.1	128.9	149.2	63.9	1.5	29.06	0.11	127.1
408	92	29.0	110.5	13.0	131.6	149.0	63.9	0.9	29.10	0.07	127.1
129	97	30.4	36.9	14.4	46.9	146.2	63.9	0.2	29.13	0.04	127.1
33	102	32	9.9	15.3	11.6	143.7	63.9	0.2	29.00	0.17	127.1

Based on Table 31, the yearly cooling energy output from the ABS system is 1,716 MMBtu, the yearly latent energy avoided from the DEH system is 1,283 MMBtu, and the yearly heating energy output from the GDHS system is 265 MMBtu. It provides 3,264 MMBtu energy, which consists of 2,999 MMBtu for cooling and 265 MMBtu for heating. The average geothermal fluid return temperature is 155.5°F, obtained by

Equation (148). And the conditioned area served by the integrated geothermal plant system would be 61,082 ft^2.

$$T_{geo,return.average,variable\ flow} = \frac{\sum T_{DEH,return,i} \cdot N_i \cdot V_{HW,1,i} + \cdot \sum T_{GDHS,return,i} \cdot N_i \cdot V_{HW,2,i}}{V_{tot} \cdot \sum N_i} \quad (148)$$

Note that in each bin the flowrate distribution is not the only solution since none of the systems' maximum capacities are reached. For example, in the 32°F bin, $V_{HW,1}$ can be slightly decreased or increased and the geothermal fluid return temperature from the ABS system would be increased or decreased, respectively.

Case F: 2 loops— GDHS is in series with DEH, while in parallel with ABS

Since the cooling load is ten times more than the heating load and the allowed geothermal temperature drop of the ABS system is much less than that of the GDHS system, the geothermal fluid flowrate through the GDHS system would be much less than that through the ABS system. As a result, the geothermal energy supplied to the DEH system following the GDHS system would be limited.

Similarly, if the heating load is a few times more than the cooling load in the building profile, case F should result in more energy output than case E since the flowrate through the GDHS system would be much more than that through the ABS system.

Case G: 1 loop—ABS and GDHS is in parallel, and then in series with DEH

The DEH system can perform with a large geothermal temperature drop but the latent load takes only one-third of the total building cooling load. Thus, the DEH system

performance is conditioned to the ABS system performance. In case F, the actual latent load avoided by the DEH system takes only around 37% of its capacity. Thus, in case G, The ABS and GDHS system performances remain the same as in case E. The DEH performance will not be influenced as long as the energy output is far away from its capacity. Figure 53 shows the cascaded flow path for case G.

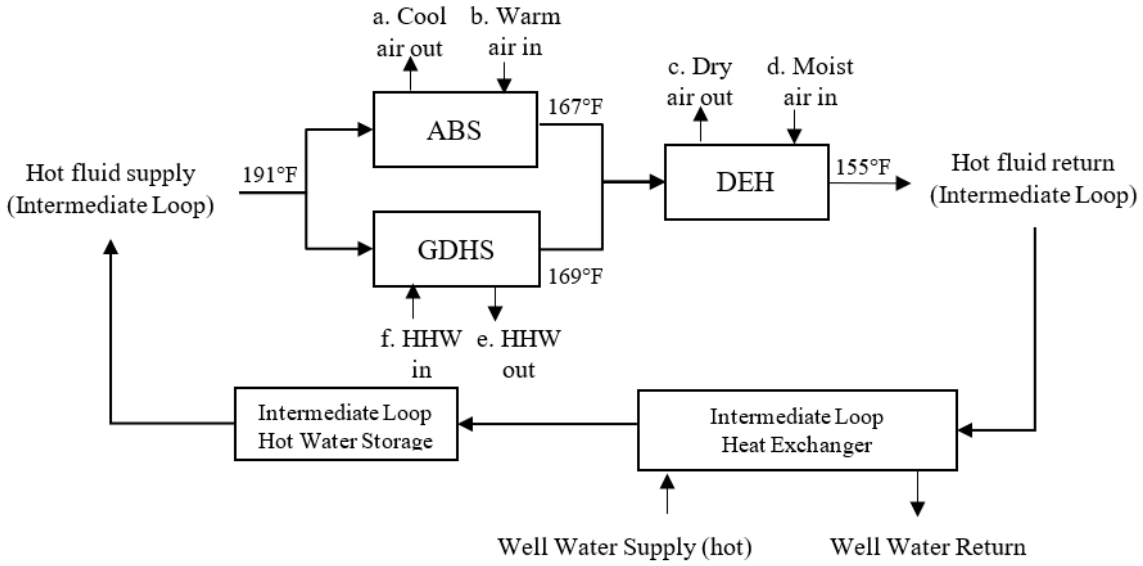

Figure 53. The cascaded flow path of case G arrangement.

It is worth mentioning that the theoretical the DEH system capacity, 3,524 MMBtu in case H is slightly higher than that of case F, 3,532 MMBtu, according to Table 32, because the geothermal fluid entering temperature is lower and the geothermal fluid leaving temperature could be lower as well. From the perspective of the system capacity, case G is better than case E. Since case E and case F are symmetrical compared to case G, it is safe to conclude that case G is also better than case F.

Table 32. The DEH system capacity comparison between case F and case G.

N_{bin}	T_1	$T_{EA,DEH,in}$	Case E			Case G		
			$V_{HW,1}$	$T_{geo,supply,DEH}$	$Q_{DEH,Capacity}$	$V_{HW,tot}$	$T_{geo,supply,DEH}$	$Q_{DEH,Capacity}$
-	°F	°F	gpm	°F	MMBtu	gpm	°F	MMBtu
866	67	105	28.61	167.7	310.1	29.17	166.9	312.2
1197	72	108.9	28.82	166.7	662.5	29.17	166.2	665.0
1402	77	113.5	28.95	165.7	1031.3	29.17	165.4	1033.0
779	82	115.4	29.01	164.5	617.0	29.17	164.3	617.7
446	87	116.5	29.06	163.3	372.6	29.17	163.2	373.0
408	92	118.3	29.10	162.0	384.9	29.17	161.9	385.1
129	97	118.6	29.13	160.6	119.1	29.17	160.6	119.2
33	102	118.2	29.01	159.0	26.9	29.17	158.8	27.0

Case H: Different arrangements during peak load and base load

Since case G is the best among all cases if the proposed geothermal plant matches the building load, any combination will not enhance the integrated system performance comparing to case G itself. In other words, case H is equivalent to case G.

4.6 LER Analysis and Comparison

The conventional energy efficiency measures are COP for equipment, like absorption chillers, energy efficiency for components, and various indices for HVAC systems based on utility bills. However, these fail to consider the effects of HVAC system type and how well the air side system matches the waterside system. Thus, the comprehensive HVAC system energy efficiency measure, LER, introduced in Section

3.4, is used to obtain an overall system performance evaluation, compared to traditional HVAC systems with chillers and boilers.

The zone load is different from the coil load since there is inefficiency in the air conditioning system, like reheating the cooling air or overheating the space. Sensible and latent load from ventilation air also contributes to the coil load in the air conditioning systems in most cases, so the zone cooling load is smaller than the actual cooling coil load. In the original setting of the LER definition, the zone load is calculated by adding up the envelope load, the load from internal gains, and the ventilation air load. However, the GSC Building studied in this dissertation is configured with SDVAV system and consumes very little reheat. For the sake of simplicity, since the air-side system is highly efficient, it is assumed that the coil load equals the zone load.

Because of the integrated system capacity covers a conditioned area of around 40,000 to 60,000 ft^2, the fan and pump sizes are scaled down to lower capacities with given VFD curves. To be specific, the capacities of the supply fan, cooling tower fan, condenser water pump, building CHW pump, building HHW pump, surface circulated HHW pump are 5hp, 2hp, 2hp, 5hp, 2 hp, and 5hp.

The energy input E_{BS} includes the air side and water side energy consumption as well as plant consumption given in Equation (149). The airside includes the energy consumption of the fan motors in the air handling units $E_{AHU,fan}$ and any return fans present. The waterside consumption includes the building cooling pump $E_{CHW\ pump}$and heating pump $E_{HHW\ pump}$ as well as the primary and secondary CHW $E_{CHW\ pump,plant}$ and HHW pumps $E_{HHW\ pump,plant}$ if applicable. The plant consumption includes the

energy consumption of the absorption chiller E_{ABS}, desiccant wheel drive E_{DEH}, the cooling tower fans $E_{CT\ fan}$, the condensing water pumps $E_{CW\ pump}$, the subsurface well pumps $E_{well\ pump}$, and the surface circulating HHW pump $E_{surface\ pump}$.

$$\begin{aligned} E_{BS} = {} & E_{AHU,fan} + E_{CHW\ pump} + E_{HHW\ pump} + E_{CHW\ pump,plant} \\ & + E_{HHW\ pump,plant} + E_{ABS} + E_{DEH} + E_{CT\ fan} + E_{CW\ pump} \\ & + E_{well\ pump} + E_{surface\ pump} \end{aligned} \quad (149)$$

The thermal compressor, usually a solution pump, in the absorption chiller is often driven by electrical motors, which consume less than 1% of the total energy output of each system and can be ignored in the calculation [150]. A typical drive motor for desiccant wheels have a nominal power of 0.25 - 0.4 kW and the motor is controlled by the frequency of the inverters [151, 152]. A nominal power of 0.3 kW for a desiccant wheel drive motor is used in the DEH system energy input calculation.

To define the LER for any building that meets its loads using more than one type of energy input requires the adoption of a convention for treating the different energy inputs. The LER is defined so any consistent convention may be used. All energy inputs may be converted to primary or source energy inputs, site energy input may be used, or all energy inputs may be converted to the predominant energy used for heating or cooling. The two typical conventions adopted in this dissertation are to convert other energy inputs to the predominant energy input in terms of both cost and site energy. This enables a straight-up comparison between a cooling system using only electricity and one using electricity plus gas reheat, as an example. These different approaches will be called heating/cooling cost LER, and heating/cooling site energy LER, respectively.

Note that the cost LER only includes the energy costs, not the capital cost or maintenance cost of the energy-using systems. Furthermore, the LER can be applied for cooling $LER_{cooling}$, separately heating $LER_{heating}$, or combing cooling and heating LER_{tot}.

$$Site\ Energy\ LER_i = \frac{Q_{BSL,i}(MMBtu)}{E_{BS,i}(kWh) \cdot \frac{0.003412\ MMBtu}{kWh}} \tag{150}$$

$$Cost\ LER_{cooling} = \frac{Q_{BSL,cooling}(MMBtu) \cdot P_{CHW}}{E_{BS,cooling}(kWh) \cdot P_{ele}} \tag{151}$$

$$Cost\ LER_{heating} = \frac{Q_{BSL,heating}(MMBtu) \cdot P_{HHW}}{E_{BS,heating}(kWh) \cdot P_{ele}} \tag{152}$$

$$Cost\ LER_{tot} = \frac{Q_{BSL,cooling}(MMBtu) \cdot P_{CHW} + Q_{BSL,heating}(MMBtu) \cdot P_{HHW}}{E_{BS,tot}(kWh) \cdot P_{ele}} \tag{153}$$

where "i" represents the scenarios of "cooling", "heating", and "tot"; P_{CHW} is the CHW energy rate; P_{HHW} is the HHW energy rate; P_{ele} is the electricity rate.

Case A: ABS only – Best configuration for eliminating sensible cooling coil load

Since the ABS system runs at full capacity the whole year, all fans and pumps are treated running at their constant maximum speeds. The energy inputs include AHU fan, CHW pump, well pump, surface circulated HHW pump, cooling tower fan, and condenser water pump. The yearly energy input is 155,263 kWh while the yearly total output is 2,724 MMBtu, thus the site energy $LER_{cooling}$ is 5.14 and the cost $LER_{cooling}$ is 3.08. Since case A only provides cooling energy, the $LER_{heating}$ is not available.

Case B: DEH only – Best configuration for eliminating latent cooling coil load

Similarly, the DEH system runs at full capacity for 5,260 hours in a year, and all fans and pumps are treated as running at constant maximum speeds during these operation hours. The DEH system avoids a portion of the cooling coil loads and the building CHW consumption, and has no energy consumption related to CHW pump or cooling tower. The energy inputs only include AHU fan, well pump, and surface circulating pump. The yearly total input is 5,9505 kWh and the yearly total output is 5,374 MMBtu, thus the site energy $LER_{cooling}$ is 26.49 and the cost $LER_{cooling}$ is 15.85. Case B only provides cooling energy, so $LER_{heating}$ is not applicable.

Case C: GDHS only – Best configuration for eliminating heating coil load

The GDHS system runs at full capacity for the whole year, and all fans and pumps are treated as running at constant maximum speeds. The energy inputs include the AHU fan, HHW pump, well pump, and the surface circulating HHW pump. The yearly total input is 109,537 kWh and the yearly total output is 7,474 MMBtu, thus the site energy $LER_{heating}$ is 20.01 and the cost $LER_{heating}$ is 11.74. Case C only provides heating energy, so $LER_{cooling}$ is not applicable.

Case D: 3 loops - each system is supplied individually and directly from the heat source – best configuration for maximum output when the integrated system is operating at full capacity

When OAT is lower than 75°F, the GDHS runs at full capacity for 5,563 hours. The heating energy input is 69,561 kWh and the heating energy output is 4,584 MMBtu. Thus, the site energy $LER_{heating}$ is 19.32 and the cost $LER_{heating}$ is 11.34. When OAT is higher than 75°F, the DEH runs at full capacity for 3,197 hours. The cooling energy

input is 36,167 kWh and the cooling energy output is 3,988 MMBtu. Thus the site energy $LER_{cooling}$ is 32.32 and the cost $LER_{cooling}$ is 19.35. Overall, the total energy input is 105,728 kWh and the total energy output is 8,752 MMBtu. Thus the site energy LER_{tot} is 23.76 and the cost LER_{tot} is 14.08.

Case G: 1 loop - ABS and GDHS is in parallel, and then in series with DEH – best configuration for maximum output when the integrated system matches the building load.

As a typical building load profile, the cooling load increases and the heating load decreases when OAT increases. CHW pump, HHW pump, and AHU fan are configured with VFDs. The energy consumption of the well pump, surface circulating pump, and AHU fan are split between cooling and heating according to the coil load fractions serving for space cooling and space heating, where an example is given in Equation (154).

$$E_{well\ pump,cooling} = \frac{Q_{BSL,cooling}}{Q_{BSL}} \cdot E_{well\ pump} \tag{154}$$

The heating energy input is 10,724 kWh and the heating energy output is 265 MMBtu. Thus, the site energy $LER_{heating}$ is 7.24 and the cost $LER_{heating}$ is 4.25. The cooling energy input is 111,531 kWh and the cooling energy output is 2,999 MMBtu. Thus, the site energy $LER_{cooling}$ is 7.89 and the cost $LER_{cooling}$ is 4.72. Overall, the total energy input is 122,255 kWh and the total energy output is 3,264 MMBtu. Thus, the site energy LER_{tot} is 7.83 and the cost LER_{tot} is 4.68.

Table 33 summarizes site energy LER and cost LER values for cooling, heating, and total analyzed in different cases. The DEH system has the highest overall COP and requires the least energy input. Besides, Case D only enables the DEH system when its overall COP is higher than 1. Therefore, case D has the highest cooling LER. Similarly, case A has the lowest cooling LER since the ABS system has the lowest COP and requires the most energy input.

LER values for the case studies of TSC and GSC served by traditional plants are also listed for comparison in Table 33 [115]. $LER_{cooling}$ for buildings served by traditional plants are around 1.5 - 2.5 while the values for case G are around 4.79 - 8.0. Basically, it demonstrates that the building served by the integrated geothermal system performs two times more cost and energy efficient than one served by traditional plants.

Table 33. LER values for buildings served by the integrated geothermal system and traditional plants.

Cases	Site Energy Conversion			Cost Conversion		
	$LER_{cooling}$	$LER_{heating}$	LER_{tot}	$LER_{cooling}$	$LER_{heating}$	LER_{tot}
Case A	5.14	-	5.14	3.08	-	3.08
Case B	26.49	-	26.49	15.85		15.85
Case C	-	20.01	20.01	-	11.74	11.74
Case D	32.32	19.32	23.76	19.35	11.34	14.08
Case G	7.89	7.24	7.83	4.72	4.25	4.68
GSC	2.46	0.04	2.35	1.99	0.06	1.90
TSC	2.28	0.46	1.51	1.44	0.59	1.08

The traditional boiler efficiency must be lower than 1. The energy input includes the energy consumption of heating hot water pumps and fans in addition to the boiler itself. The combustion efficiency is always lower than 1, so the $LER_{heating}$ values for buildings served by boiler plants are lower than 1. However, since the geothermal energy source is considered an energy source that requires only the input of well pump power consumption, the $LER_{heating}$ for buildings served by the proposed geothermal fluids can exceed 1. Thus, the $LER_{heating}$ values for buildings served by the proposed geothermal plant are at least 10 times the $LER_{heating}$ values of buildings served by boiler plants.

CHAPTER V

CONCLUSIONS AND DISCUSSION

In this dissertation, an optimized plant is developed for a district heating and cooling system using low-grade geothermal fluids.

The pressure loss and the heat loss through the subsurface well pumping system is estimated as 224.2 pisa and 29°F with an insulation thickness of 50 mm. The optimum geothermal fluid flowrate and temperature supplied to the surface end-use system is determined as 29 gpm and 191°F.

The absorption chiller, the desiccant wheel, and the geothermal district heating systems are selected for cooling, dehumidification, and heating in this geothermal application. They are modeled and simplified with relationships between the required geothermal fluid temperature and its output at different outside air conditions. Configurations of a dedicated outside air system with desiccant wheel application are studied with detailed energy performance. The desiccant wheel DOAS system with heat exchanger and condenser water cooling shows the ability to avoid the most cooling coil load and is selected for the surface integrated system. A 202,467 ft^2 (18,809 m^2) administrative office building with two major outdoor air handling units on the Texas A&M University campus which are served by a central utility plant is analyzed as a case study. The yearly CHW energy and cost savings are 2,261 MMBtu (2,385 GJ), and $34,512, with a 19.7% reduction in the building total CHW energy consumption.

The surface end-use system modeling is developed by combining these three heat-operated system models (ABS, DEH, and GDHS) with load profiles of typical campus buildings. The inlet temperature requirements and the maximum temperature drops of each system are studied and possible system arrangements are investigated based on the temperature requirements. A typical campus building, called the General Services Complex, is used to generate the load profile. The four-parameter model is adopted to obtain a piecewise expression between the building cooling and heating load and the outside air temperature separately.

A new configuration called multiple pump sizes with VFD is also studied here. A lower capacity pump with VFD is added to cover the operating hours with lower loads and maintain a constant loop differential pressure in the pumping system. It can significantly reduce pump energy consumption. A lab building and a hospital building both running for 24 hours per day 7 days per week are analyzed as case studies and results show 10.5% – 32.1% pumping power energy savings with the new configuration and 1.5 – 7.1 year simple payback.

The energy performance of all proposed system arrangements is calculated and compared using the bin method. When the building loads are large and the integrated system operates at its full capacity, the optimized arrangement is the DEH system and the GDHS operated in parallel. When the OAT is lower than 75°F, the GDHS system is operated, otherwise, the DEH system is operated. The yearly total energy output is 8,572 MMBtu, which consists of 4,584 MMBtu heating energy and 3,988 MMBtu cooling energy savings. When the integrated system matches the building loads well, the

optimized arrangement is that the ABS system and the GDHS system are in parallel, and then in series with the DEH system. In this case, the yearly total energy output is 3,264 MMBtu, which consists of 2,999 MMBtu for cooling and 265 MMBtu for heating.

To evaluate the geothermal plant energy performance and compare it with traditional plants, both the site energy LER and the cost LER are introduced and calculated for all cases. $LER_{cooling}$ values for buildings served by traditional plants are around 1.5 - 2.5 while the values for the optimized geothermal plant are around 4.72 – 7.89. $LER_{heating}$ values for buildings served by traditional plants are around 0.043 – 0.59 while the values for the optimized geothermal plant are around 4.25 – 7.24. The building served by the integrated geothermal system performs at least two times more cost and energy efficiently than one served by traditional plants.

Given that the total well capacity will only be able to supply a small portion of the buildings that will be built on the Texas A&M RELLIS Campus, it is recommended that the GDHS system and the DEH system be configured in parallel to produce the maximum output with a total LER of 14.08 – 23.76.

REFERENCES

[1] R.A. Caulk, I. Tomac, Reuse of abandoned oil and gas wells for geothermal energy production, Renewable Energy 112 (2017) 388-397.

[2] J. Tester, H. Herzog, Z. Chen, R. Potter, M. Frank, Prospects for universal geothermal energy from heat mining, Science & Global Security 5(1) (1994) 99-121.

[3] R. Weijermars, L. Zuo, I. Warren, Modeling Reservoir circulation and economic performance of the Neal Hot Springs geothermal power plant (Oregon, US): an integrated case study, Geothermics 70 (2017) 155-172.

[4] D. Westphal, R. Weijermars, Economic appraisal and scoping of geothermal energy extraction projects using depleted hydrocarbon wells, Energy Strategy Reviews 22 (2018) 348-364.

[5] R. Weijermars, D. Burnett, D. Claridge, S. Noynaert, M. Pate, D. Westphal, W. Yu, L. Zuo, Redeveloping depleted hydrocarbon wells in an enhanced geothermal system (EGS) for a university campus: Progress report of a real-asset-based feasibility study, Energy Strategy Reviews 21 (2018) 191-203.

[6] M. Waite, A. Deshmukh, V. Modi, Experimental and analytical investigation of hydronic system retrofits in an urban high-rise mixed use building, Energy and Buildings 136 (2017) 173-188.

[7] IPCC, Climate change 2014, 5th edition, IPCC, Geneva (2014).

[8] C. Rühl, Global Energy After the Crisis, Foreign Affairs, 2010, pp. 63-75.

[9] L.P. Rosa, L.L.B. Lomardo, The Brazilian energy crisis and a study to support building efficiency legislation, Energy & Buildings 36(2) (2004) 89.

[10] A. Kapur, T.E. Graedel, Industrial ecology, Encyclopedia of Energy 3 (2004) 373-382.

[11] U. EIA, Monthly Energy Review, (2017).

[12] M.I. Alhamid, Y. Daud, A. Surachman, A. Sugiyono, H. Aditya, T. Mahlia, Potential of geothermal energy for electricity generation in Indonesia: A review, Renewable and Sustainable Energy Reviews 53 (2016) 733-740.

[13] J.W. Lund, L. Bjelm, G. Bloomquist, A.K. Mortensen, Characteristics, development and utilization of geothermal resources-a Nordic perspective, Episodes 31(1) (2008) 140-147.

[14] B. Erdogmus, M. Toksoy, B. Ozerdem, N. Aksoy, Economic assessment of geothermal district heating systems: a case study of Balcova–Narlidere, Turkey, Energy and Buildings 38(9) (2006) 1053-1059.

[15] R. Staiger, A. Tanţău, Energy efficiency model for small/medium geothermal heat pump systems, Management & Marketing 10(1) (2015) 12-33.

[16] A.S. Anifantis, S. Pascuzzi, G. Scarascia-Mugnozza, Geothermal source heat pump performance for a greenhouse heating system: an experimental study, Journal of Agricultural Engineering (1974-7071) 47(3) (2016) 164-170.

[17] C. Augustine, Update to Enhanced Geothermal System Resource Potential Estimate, National Renewable Energy Lab.(NREL), Golden, CO (United States), 2016.

[18] B. Matek, Annual US & global geothermal power production report, Geothermal Energy Association Reports (2014).

[19] J.W. Lund, D.H. Freeston, T.L. Boyd, Direct utilization of geothermal energy 2010 worldwide review, Geothermics 40(3) (2011) 159-180.

[20] M. Dickson, M. Fanelli, Geothermal energy: utilization and technology: UNESCO renewable energy series, Earthscan, London 205 (2003).

[21] L. Ozgener, A. Hepbasli, I. Dincer, Exergy analysis of two geothermal district heating systems for building applications, Energy Conversion and Management 48(4) (2007) 1185-1192.

[22] C. Steins, S. Zarrouk, Assessment of the geothermal space heating system at Rotorua Hospital, New Zealand, Energy Conversion and Management 55 (2012) 60-70.

[23] E. Barbier, M. Fanelli, Non-electrical uses of geothermal energy, Progress in Energy and Combustion Science 3(2) (1977) 73-103.

[24] E. Barbier, Geothermal energy technology and current status: an overview, Renewable and Sustainable Energy Reviews 6(1-2) (2002) 3-65.

[25] W.-L. Cheng, J. Liu, Y.-L. Nian, C.-L. Wang, Enhancing geothermal power generation from abandoned oil wells with thermal reservoirs, Energy 109 (2016) 537-545.

[26] N. Wight, N. Bennett, Geothermal energy from abandoned oil and gas wells using water in combination with a closed wellbore, Applied Thermal Engineering 89 (2015) 908-915.

[27] J.W. Lund, Direct utilization of geothermal energy, Energies 3(8) (2010) 1443-1471.

[28] M. De Moel, P.M. Bach, A. Bouazza, R.M. Singh, J.O. Sun, Technological advances and applications of geothermal energy pile foundations and their feasibility in Australia, Renewable and Sustainable Energy Reviews 14(9) (2010) 2683-2696.

[29] M. Vajpayee, R.S. Martolia, K. Chanchlani, M. Mehta, A. Chauhan, A. Sodani, Generating Electricity Using Co-Produced Brine from Oil & Gas Wells Evaluating Prospect in Mehsana Asset North Cambay Basin Gujarat, International Petroleum Technology Conference, International Petroleum Technology Conference, 2016.

[30] D. Keppler, Absorption chillers as a contribution to a climate-friendly refrigeration supply regime: Factors of influence on their further diffusion, Journal of Cleaner Production 172 (2018) 1535-1544.

[31] Trane Company, Single-Stage Hot Water or Steam-Fired Absorption Water Chillers 112-465 Tons, http://www.trane.com/download/equipmentpdfs/absprc005en.pdf Accessed by February 27th, 2018 (2001).

[32] Johnson Controls, Energy-Saving-Type Absorption Chiller (EX3/EX3P series), http://www.jci-hitachi.com/products/absorption-centrigufal-chillers/absorption/enhanced-efficiency-absorption-chiller-heaters Accessed by February 3rd, 2018 (2017).

[33] J. Gordon, K.C. Ng, A general thermodynamic model for absorption chillers: theory and experiment, Heat Recovery Systems and CHP 15(1) (1995) 73-83.

[34] T. Jaruwongwittaya, G. Chen, A review: renewable energy with absorption chillers in Thailand, Renewable and Sustainable Energy Reviews 14(5) (2010) 1437-1444.

[35] F. Ziegler, H. Hellmann, C. Schweigler, An approximative method for modeling the operating characteristics of advanced absorption chillers, 29th International Congress of Refrigeration, 1999.

[36] H.-M. Hellmann, F.F. Ziegler, Simple absorption heat pump modules for system simulation programs, ASHRAE Transactions 105 (1999) 780.

[37] O. Kaynakli, M. Kilic, Theoretical study on the effect of operating conditions on performance of absorption refrigeration system, Energy Conversion and Management 48(2) (2007) 599-607.

[38] W. Wu, X. Zhang, X. Li, W. Shi, B. Wang, Comparisons of different working pairs and cycles on the performance of absorption heat pump for heating and domestic hot water in cold regions, Applied Thermal Engineering 48 (2012) 349-358.

[39] A. Sözen, E. Arcaklioğlu, M. Özalp, A new approach to thermodynamic analysis of ejector–absorption cycle: artificial neural networks, Applied Thermal Engineering 23(8) (2003) 937-952.

[40] A. Sözen, M.A. Akçayol, Modelling (using artificial neural-networks) the performance parameters of a solar-driven ejector-absorption cycle, Applied Energy 79(3) (2004) 309-325.

[41] S. Rosiek, F. Batlles, Performance study of solar-assisted air-conditioning system provided with storage tanks using artificial neural networks, International Journal of Refrigeration 34(6) (2011) 1446-1454.

[42] U. DoE, EnergyPlus engineering reference: the reference to EnergyPlus calculations, Lawrence Berkeley National Laboratory (2009).

[43] J.M. Gordon, K.C. Ng, Cool thermodynamics, Viva Books2008.

[44] A. Kühn, F. Ziegler, Operational results of a 10 kW absorption chiller and adaptation of the characteristic equation, Proc. First Int. Conference Solar Air Conditioning, Bad-Staffelstein, 2005.

[45] J. Labus, J.C. Bruno, A. Coronas, Performance analysis of small capacity absorption chillers by using different modeling methods, Applied Thermal Engineering 58(1-2) (2013) 305-313.

[46] M. Puig-Arnavat, J. López-Villada, J.C. Bruno, A. Coronas, Analysis and parameter identification for characteristic equations of single-and double-effect absorption chillers by means of multivariable regression, International Journal of Refrigeration 33(1) (2010) 70-78.

[47] Broad, http://www.broad.com/Storage/Largedownloads/fdktxxsjsc1.pdf, Accessed by March 8th, 2018.

[48] P.J. Tidwell, Low Temperature Geothermal Waste-Heat-to-Power-Report, 2014.

[49] R. DiPippo, Geothermal power plants: principles, applications, case studies and environmental impact, Butterworth-Heinemann2012.

[50] ElectricaTherm, https://electratherm.com/products/power-plus-generator-4200-up-to-35kwe/, Accessed by March 8th, 2018.

[51] H. Teng, G. Regner, C. Cowland, Waste heat recovery of heavy-duty diesel engines by organic Rankine cycle part I: hybrid energy system of diesel and Rankine engines, SAE Technical Paper, 2007.

[52] S. Song, H. Zhang, Z. Lou, F. Yang, K. Yang, H. Wang, C. Bei, Y. Chang, B. Yao, Performance analysis of exhaust waste heat recovery system for stationary CNG engine based on organic Rankine cycle, Applied Thermal Engineering 76 (2015) 301-309.

[53] Y. Yang, Y. Huo, W. Xia, X. Wang, P. Zhao, Y. Dai, Construction and preliminary test of a geothermal ORC system using geothermal resource from abandoned oil wells in the Huabei oilfield of China, Energy 140 (2017) 633-645.

[54] K. Rahbar, S. Mahmoud, R.K. Al-Dadah, N. Moazami, S.A. Mirhadizadeh, Review of organic Rankine cycle for small-scale applications, Energy Conversion and Management 134 (2017) 135-155.

[55] B.-R. Fu, Y.-R. Lee, J.-C. Hsieh, Design, construction, and preliminary results of a 250-kW organic Rankine cycle system, Applied Thermal Engineering 80 (2015) 339-346.

[56] I.K. Smith, N. Stosic, A. Kovacevic, Screw expanders increase output and decrease the cost of geothermal binary power plant systems, Transactions of Geothermal Resource Council, Reno, NV, September (2005) 25-28.

[57] T.R. Biederman, J.J. Brasz, Geothermal ORC systems using large screw expanders, Purdue University International Compressor Engineering Conference (2014).

[58] V. Minea, Power generation with ORC machines using low-grade waste heat or renewable energy, Applied Thermal Engineering 69(1-2) (2014) 143-154.

[59] A. Algieri, J. Šebo, Energetic Investigation of Organic Rankine Cycles (ORCs) for the Exploitation of Low-Temperature Geothermal Sources–A possible application in Slovakia, Procedia Computer Science 109 (2017) 833-840.

[60] P.J. Tidwell, Low Temperature Geothermal Waste-Heat-to-Power, 2014.

[61] ElectricaTherm, https://electratherm.com/products/power-plus-generator-6500-up-to-110kwe/ Accessed by May 13, 2018.

[62] T.A.M.U.U.E. Services, https://utilities.tamu.edu/2015/08/31/cost-and-fees-for-utility-services-fy2016/, Accessed by March 8th, 2018.

[63] H. Lund, B. Möller, B.V. Mathiesen, A. Dyrelund, The role of district heating in future renewable energy systems, Energy 35(3) (2010) 1381-1390.

[64] L.B. Liu, A.J. Zou, J.J. Liao, Y.F. Ma, The Case Study on Optimization of Large Scale Heating and Cooling Network, Applied Mechanics and Materials, Trans Tech Publ, 2014, pp. 611-615.

[65] P. Lei Wang PhD, Y.S. DrEng, S.J. Bowman, Commissioning an Existing Heat Recovery Chiller System at a Large District Plant, ASHRAE Transactions 124 (2018) 52-60.

[66] A. Benonysson, B. Bøhm, H.F. Ravn, Operational optimization in a district heating system, Energy Conversion and Management 36(5) (1995) 297-314.

[67] L.B. Liu, A.J. Zou, J.J. Liao, Y.M. Liu, The optimization of large scale heating and cooling network, Applied Mechanics and Materials, Trans Tech Publ, 2014, pp. 616-620.

[68] G.C. Karvountzi, N.J. Themelis, V. Modi, Maximum distance to which cogenerated heat can be economically distributed in an urban community, ASHRAE Transactions 108 (2002) 334.

[69] N. Yamankaradeniz, Thermodynamic performance assessments of a district heating system with geothermal by using advanced exergy analysis, Renewable Energy 85 (2016) 965-972.

[70] D.H.F. John W. Lund, Tonya L. Boyd, World-Wide Direct Uses of Geothermal Energy 2005 Proceedings World Geothermal Congress 2005 Antalya, Turkey, 24-29 April 2005 (2005).

[71] M. Tan, A. Keçebaş, Thermodynamic and economic evaluations of a geothermal district heating system using advanced exergy-based methods, Energy Conversion and Management 77 (2014) 504-513.

[72] L. Ozgener, A. Hepbasli, I. Dincer, Thermodynamic analysis of a geothermal district heating system, International Journal of Exergy 2(3) (2005) 231-245.

[73] L. Ozgener, A. Hepbasli, I. Dincer, A key review on performance improvement aspects of geothermal district heating systems and applications, Renewable and Sustainable Energy Reviews 11(8) (2007) 1675-1697.

[74] A. Handbook, HVAC systems and equipment, American Society of Heating, Refrigerating, and Air Conditioning Engineers, Atlanta, GA (2016) 1-10.

[75] K. Bailey, Using Plate Heat Exchangers to Increase Energy Efficiency, (1999).

[76] T.N. Aynur, Y. Hwang, R. Radermacher, Simulation comparison of VAV and VRF air conditioning systems in an existing building for the cooling season, Energy and Buildings 41(11) (2009) 1143-1150.

[77] S. El-Agouz, R. Sathyamurthy, Improvement of humidification–dehumidification desalination unit using a desiccant wheel, Chemical Engineering Research and Design (2017).

[78] L.-Z. Zhang, H.-X. Fu, Q.-R. Yang, J.-C. Xu, Performance comparisons of honeycomb-type adsorbent beds (wheels) for air dehumidification with various desiccant wall materials, Energy 65 (2014) 430-440.

[79] S. De Antonellis, C.M. Joppolo, L. Molinaroli, Simulation, performance analysis and optimization of desiccant wheels, Energy and Buildings 42(9) (2010) 1386-1393.

[80] L. Zhang, J. Niu, Indoor humidity behaviors associated with decoupled cooling in hot and humid climates, Building and Environment 38(1) (2003) 99-107.

[81] L. Zhang, Energy performance of independent air dehumidification systems with energy recovery measures, Energy 31(8-9) (2006) 1228-1242.

[82] O. Labban, T. Chen, A.F. Ghoniem, L.K. Norford, Next-generation HVAC: Prospects for and limitations of desiccant and membrane-based dehumidification and cooling, Applied Energy 200 (2017) 330-346.

[83] J. Jurinak, J. Mitchell, W. Beckman, Open-cycle desiccant air conditioning as an alternative to vapor compression cooling in residential applications, Journal of Solar Energy Engineering 106(3) (1984) 252-260.

[84] D. La, Y. Dai, Y. Li, R. Wang, T. Ge, Technical development of rotary desiccant dehumidification and air conditioning: A review, Renewable and Sustainable Energy Reviews 14(1) (2010) 130-147.

[85] G. Angrisani, C. Roselli, M. Sasso, Effect of rotational speed on the performances of a desiccant wheel, Applied Energy 104 (2013) 268-275.

[86] M. Goldsworthy, S. White, Optimisation of a desiccant cooling system design with indirect evaporative cooler, International Journal of Refrigeration 34(1) (2011) 148-158.

[87] S. Jain, P. Bansal, Performance analysis of liquid desiccant dehumidification systems, International Journal of Refrigeration 30(5) (2007) 861-872.

[88] S. Feyka, K. Vafai, An investigation of a falling film desiccant dehumidification/regeneration cooling system, Heat Transfer Engineering 28(2) (2007) 163-172.

[89] E. Kozubal, L. Herrmann, M. Deru, J. Clark, A. Lowenstein, Low-Flow Liquid Desiccant Air-Conditioning: Demonstrated Performance and Cost Implications, National Renewable Energy Laboratory (NREL), Golden, CO., 2014.

[90] Y. Yin, X. Zhang, D. Peng, X. Li, Model validation and case study on internally cooled/heated dehumidifier/regenerator of liquid desiccant systems, International Journal of Thermal Sciences 48(8) (2009) 1664-1671.

[91] S.-C. Hu, A. Shiue, Y.-S. Chiu, A. Wang, J. Chen, Simplified Heat and Mass Transfer Model for Cross-Flow and Countercurrent Flow Packed Bed Tower Dehumidifiers with a Liquid Desiccant System, Sustainability 8(12) (2016) 1264.

[92] W. Goetzler, T. Sutherland, C. Reis, Energy savings potential and opportunities for high-efficiency electric motors in residential and commercial equipment, EERE Publication and Product Library, 2013.

[93] G. Wang, Efficiency degradation detection for VFD-motor-pump systems, Science and Technology for the Built Environment (2018) 1-8.

[94] Y. Yao, Z. Lian, W. Liu, Z. Hou, M. Wu, Evaluation program for the energy-saving of variable-air-volume systems, Energy and Buildings 39(5) (2007) 558-568.

[95] M. Teitel, A. Levi, Y. Zhao, M. Barak, E. Bar-lev, D. Shmuel, Energy saving in agricultural buildings through fan motor control by variable frequency drives, Energy and Buildings 40(6) (2008) 953-960.

[96] M. Pemberton, Variable speed pumping: myths and legends, World pumps 2005(460) (2005) 22-24.

[97] U. DOE, Improving Motor and Drive System Performance: A Sourcebook for Industry, PDF, 2008.

[98] G. Wang, L.J. Song, Performance assessment of variable frequency drives in heating, ventilation, and air-conditioning systems, Science and Technology for the Built Environment 24(10) (2018) 1075-1083.

[99] L. Liu, Y. Liu, J. Liao, Issues of pumps and fans in HVAC systems, World Pumps 2015(1) (2015) 26-29.

[100] E. Andiroglu, G. Wang, L. Song, K.J. Kiamehr, Development of a virtual pump water flow meter using power derived from comprehensive energy loss analysis, Science and Technology for the Built Environment 22(2) (2016) 214-226.

[101] G. Wang, L. Song, E. Andiroglu, G.J. Shim, Investigations on a virtual airflow meter using projected motor and fan efficiencies, Science and Technology for the Built Environment 20(2) (2014) 178-187.

[102] A.L. Hjortland, J.E.J. Braun, Load-based testing methodology for fixed-speed and variable-speed unitary air conditioning equipment, Science and Technology for the Built Environment (2018) 1-12.

[103] X. Zhou, D. Yan, Influence of load feature on the water distribution system in a centralized air-conditioning system, Science and Technology for the Built Environment 23(2) (2017) 277-284.

[104] S. Treddinick, Variable Speed Pumping: How Low Can You Go, Affiliated Engineers Inc. District Energy, Third Quarter (2006).

[105] ANSI/HI, 'Centrifugal and vertical pumps for allowable operating region', ANSI/HI Standard 9.6.3 (1997).

[106] Y.-Y. Lu, J. Chen, T.-C. Liu, M.-H. Chien, Using cooling load forecast as the optimal operation scheme for a large multi-chiller system, International Journal of Refrigeration 34(8) (2011) 2050-2062.

[107] F. Yu, K. Chan, Low-energy design for air-cooled chiller plants in air-conditioned buildings, Energy and Buildings 38(4) (2006) 334-339.

[108] K.S. Dave Hacker, Variable Volume Chilled Water Pumping System Controls, http://daytonashrae.org/downloads/presentations/ASHRAE_YEA_091409.pdf, Accessed by September 10th, 2018.

[109] DOE, Room Air Conditioners, http://energy.gov/energysaver/articles/room-air-conditioners, 2012. http://energy.gov/energysaver/articles/room-air-conditioners.

[110] ANSI/ASHRAE, ANSI/ASHRAE Standard 103-2007, Method of Testing for Annual Fuel Utilization Efficiency of Residential Central Furnaces and Boilers, 2007.

[111] H. Air-conditioning, Refrigeration Institute (AHRI). AHRI Standard 550/590: Performance rating of water-chilling and heat pump water-heating packages using the vapor compression cycle, Author Press, 2011.

[112] DOE, Furnaces and Boilers, http://energy.gov/energysaver/articles/furnaces-and-boilers, 2012. http://energy.gov/energysaver/articles/furnaces-and-boilers.

[113] AHRI, Seasonal Energy Efficiency Ratio, http://www.ari.org/site/588/Homeowners/Save-Energy/Seasonal-Energy-Efficiency-Ratio, 2014. http://www.ari.org/site/588/Homeowners/Save-Energy/Seasonal-Energy-Efficiency-Ratio.

[114] J.H. Eto, I. Turiel, H. Akbari, B. Lebot, K. Heinemeier, An investigation of the use of prototypes for commercial sector EUI analysis, Proceedings of the ACEEE, 1990, p. 29.

[115] J. Liao, D. Claridge, L. Wang, Analysis of Whole-Building HVAC System Energy Efficiency, ASHRAE Transactions 124 (2018) 72-87.

[116] S.P. Kavanaugh, R. Steven Lambert, N. Devin, HVAC Power Density, (2006).

[117] S. Goel, V. Mendon, M. Rosenberg, Performance-Based Building System Evaluation for DOE Energy Asset Score, ASHRAE Transactions 120 (2014) 1II.

[118] J.F. Kreider, A. Rabl, Heating and cooling of buildings: design for efficiency McGraw-Hill, New York (1994).

[119] A.B.R. González, J.J.V. Díaz, A.J. Caamano, M.R. Wilby, Towards a universal energy efficiency index for buildings, Energy and Buildings 43(4) (2011) 980-987.

[120] T.A. Reddy, M. Liu, S. Katipamula, D.E. Claridge, E. Franconi, Extending the concept of energy delivery efficiency (EDE) of HVAC systems/Discussion, ASHRAE Transactions 104 (1998) 13.

[121] T.A. Reddy, J. Kissock, S. Katipamula, D. Claridge, An energy delivery efficiency index to evaluate simultaneous heating and cooling effects in large commercial buildings, Journal of Solar Energy Engineering 116(2) (1994) 79-87.

[122] C. Yan, S. Wang, F. Xiao, A simplified energy performance assessment method for existing buildings based on energy bill disaggregation, Energy and Buildings 55 (2012) 563-574.

[123] C. Yan, S. Wang, F. Xiao, D.-c. Gao, A multi-level energy performance diagnosis method for energy information poor buildings, Energy 83 (2015) 189-203.

[124] M.J. Economides, A.D. Hill, C. Ehlig-Economides, D. Zhu, Petroleum production systems, Pearson Education2013.

[125] S. Sukumar, R. Weijermars, I. Alves, S. Noynaert, Analysis of Pressure Communication between the Austin Chalk and Eagle Ford Reservoirs during a Zipper Fracturing Operation, Energies 12(8) (2019) 1469.

[126] J.-C. Han, Analytical heat transfer, CRC Press2016.

[127] A. Bahadori, Thermal insulation handbook for the oil, gas, and petrochemical industries, Gulf Professional Publishing2014.

[128] L. Zuo, R. Weijermars, Longevity of Enhanced Geothermal Systems with Brine Circulation in Hydraulically Fractured Hydrocarbon Wells, Fluids 4(2) (2019) 63.

[129] R. Weijermars, Claridge, D., Burnett, D., Pate, M., Noyanaert, S., Yu, W., & Zuo, L., Redeveloping Depleted Hydrocarbon Wells in an Enhanced Geothermal System (EGS) for a University Campus: Progress Report of Real-Asset-Based Feasibility Study, (2018).

[130] J. Liao, D.E. Claridge, L. Wang, Analysis of Whole-Building HVAC System Energy Efficiency, ASHRAE Transactions 124(1) (2018) 72-88.

[131] J. Labus, Modelling of small capacity absorption chillers driven by solar thermal energy or waste heat, Universitat Rovira i Virgili, 2011.

[132] C. Kettleborough, M. Ullah, D. Waugaman, Desiccant Cooling Systems-A Review, (1986).

[133] A. Handbook, Fundamentals, American Society of Heating, Refrigerating and Air Conditioning Engineers, Atlanta 111 (2001).

[134] M.-H. Kim, J.-H. Kim, A.-S. Choi, J.-W. Jeong, Experimental study on the heat exchange effectiveness of a dry coil indirect evaporation cooler under various operating conditions, Energy 36(11) (2011) 6479-6489.

[135] A. Standard, Standard 62.1-2010 (2010). ventilation for acceptable indoor air quality, atlanta, ga, American Society of Heating, Refrigerating and Air-Conditioning Engineers, Inc (2010).

[136] S. Thamilseran, J.S. Haberl, A bin method for calculating energy conservation retrofit savings in commercial buildings, (1994).

[137] M. Sengupta, Y. Xie, A. Lopez, A. Habte, G. Maclaurin, J.J.R. Shelby, S.E. Reviews, The national solar radiation data base (NSRDB), 89 (2018) 51-60.

[138] ASHRAE, ANSI/ASHRAE/IES Standard 90.1-2016 -- Energy Standard for Buildings Except Low-Rise Residential Buildings, (2016).

[139] D. Ruch, D.E. Claridge, A four-parameter change-point model for predicting energy consumption in commercial buildings, Journal of Solar Energy Engineering 114(2) (1992) 77-83.

[140] TAMU, https://utilities.tamu.edu/wp-content/uploads/2014/10/TAMU-Energy-Management-Report-November-2014.pdf. Retrieved 12/24/2018, (2014).

[141] D.E. Knebel, Simiplified energy analysis using the modified bin method, (1983).

[142] M. Liu, L. Song, G. Wei, D. Claridge, Simplified building and air handling unit model calibration and applications, ASME 2003 International Solar Energy Conference, American Society of Mechanical Engineers, 2003, pp. 15-25.

[143] D.E. Claridge, 13 Building simulation for practical operational optimization, Building Performance Simulation for Design Operation (2011) 365.

[144] https://www.engineeringtoolbox.com/affinity-laws-d_408.html, (Access by November 20th, 2018.).

[145] A.R. Simpson, A. Marchi, Evaluating the approximation of the affinity laws and improving the efficiency estimate for variable speed pumps, Journal of Hydraulic Engineering 139(12) (2013) 1314-1317.

[146] https://www.mcmaster.com/, (Accessed by March 23th 2017).

[147] M.E. Weber, Thermodynamic limitations on heat exchanger performance, Applied Energy 5(2) (1979) 159-164.

[148] J.D. Spitler, Load calculation applications manual, American Society of Heating, Refrigerating, and Air-Conditioning Engineers2010.

[149] M.F. Fels, PRISM: an introduction, Energy and Buildings 9(1-2) (1986) 5-18.

[150] A. Handbook, HVAC systems and equipment, American Society of Heating, Refrigerating, Air Conditioning Engineers, Atlanta, GA (1996) 1-10.

[151] M.A. Mandegari, H. Pahlavanzadeh, S.J.E.S. Farzad, Energy approach analysis of desiccant wheel operation, 5(3) (2014) 551-569.

[152] K. Kawamoto, W. Cho, H. Kohno, M. Koganei, R. Ooka, S. Kato, Field study on humidification performance of a desiccant air-conditioning system combined with a heat pump, Energies 9(2) (2016) 89.

[153] G.E. Phetteplace, M.J. Kryska, D.L. Carbee, Field measurements of heat losses from three types of heat distribution systems, Cold Regions Research and Engineering Lab Hanover NH, 1991.

[154] L.o.t. conductivities, (https://en.wikipedia.org/wiki/List_of_thermal_conductivities).

APPENDIX A

HOT WATER PIPELINE HEAT LOSS CALCULATION

All calculation procedures follow the 2016 ASHRAE Handbook – HVAC Systems and Equipment [74].

A.1 Pipe Sizing

The design low-temperature hot water flowrate is 200 gpm (12.6 L/s) at 200°F (93°C) ~ 220°F (104°C). Assume the maximum geothermal fluid temperature drop caused by GDHS is 60°F at the rated flowrate. Typically district heating hot water supply and return temperature difference is around 20°F with supply temperature of 135°F - 160°F and return temperature of 115°F - 140°F [65]. Thus, the maximum district heating hot water flowrate is 600 gpm (37.8 L/s).

Based on Table 6.5.4.5 Piping System Design Maximum Flow Rate in ASHRAE Standard 90.1 – 2013, chilled water and condenser water piping will be designed such that the corresponding design flowrate doesn't exceed the listed values in the table. To be consistent with a more stringent standard, these values are also applied to the low-temperature hot water piping system. Thus, a 6 inch (152 mm) nominal diameter is selected with 6.625-inch outer diameter.

A.2 Pipe Insulation

According to Table 6.8.3A Minimum Pipe Insulation Thickness Heating and Hot Water System in ASHRAE Standard 90.1 – 2013, the minimum insulation thickness for

nominal pipe sizes of 100 to 200 mm and fluid operating temperature range of 61 to 93°C is 2 inches (50 mm) for buried piping. The supply pipes are insulated with 3 inches of polyurethane foam insulation and the return pipe has 2.5 inches of polyurethane foam insulation. The polyurethane foam thermal conductivity is 0.013 $\mathrm{Btu/hr \cdot ft \cdot °F}$ at 100 °F and 0.014 $\mathrm{Btu/hr \cdot ft \cdot °F}$ at 200 °F.

Then the pipe thermal resistance is

$$R_1 = \frac{\ln(r_o/r_i)}{2\pi k_p} = \frac{\ln(6.3\mathrm{inch}/3.3\mathrm{inch})}{2\pi \cdot 0.014\mathrm{Btu/hr \cdot ft \cdot °F}} = 7.3\ \mathrm{hr \cdot ft \cdot °F/Btu} \quad (155)$$

$$R_2 = \frac{\ln(r_o/r_i)}{2\pi k_p} = \frac{\ln(5.8\mathrm{inch}/3.3\mathrm{inch})}{2\pi \cdot 0.014\mathrm{Btu/hr \cdot ft \cdot °F}} = 6.9\ \mathrm{hr \cdot ft \cdot °F/Btu} \quad (156)$$

Where R_1, R_2 are thermal resistances for supply and return pipes, $\mathrm{hr \cdot ft \cdot °F/Btu}$; r_o, r_i are the outer and inner radius of the pipe, inch or ft; k_p is the thermal conductivity of the pipe, $\mathrm{Btu/hr \cdot ft \cdot °F}$.

A.3 Trench Thermal Resistance

Figure 54 shows two pipes in buried trenches on campus. Field measurements on operating trenches indicate maximum spatial air temperature variations of about 10°F [153]. Since this level of air temperature variations does not cause significant errors for normal operating temperatures, it is assumed that the air within the trench and the inside surface of the trench are uniform in temperature. The wall of the buried trench is 6 inches thick, and the trench is 3 ft wide and 2 ft tall. The trench is constructed of medium density concrete, with thermal conductivity of 0.23 $\mathrm{Btu/hr \cdot ft \cdot °F}$ (0.4$\mathrm{W/m \cdot K}$) [154]. The centerline of the trench is 4 ft below grade and the soil temperature is

assumed to be 70°F, which is the average outside air temperature. And the soil surrounding the trench has a thermal conductivity of 0.5 $\mathrm{Btu/hr \cdot ft \cdot °F}$ [154].

The trench wall thermal resistance is

$$R_w = \frac{x_w}{2k_w(a+b)} = \frac{0.5\mathrm{ft}}{2 \cdot 0.23\mathrm{Btu/hr \cdot ft \cdot °F}(3\mathrm{ft} + 2\mathrm{ft})} = 0.217\ \mathrm{hr \cdot ft \cdot °F/Btu} \quad (157)$$

where R_w is the thermal resistance of trench walls, $\mathrm{hr \cdot ft \cdot °F/Btu}$; $x_w$is the thickness of trench walls, ft; a is the width of trench inside, ft; b is the height of trench inside, ft; and $k_w$is the thermal conductivity of trench wall material, $\mathrm{Btu/hr \cdot ft \cdot °F}$.

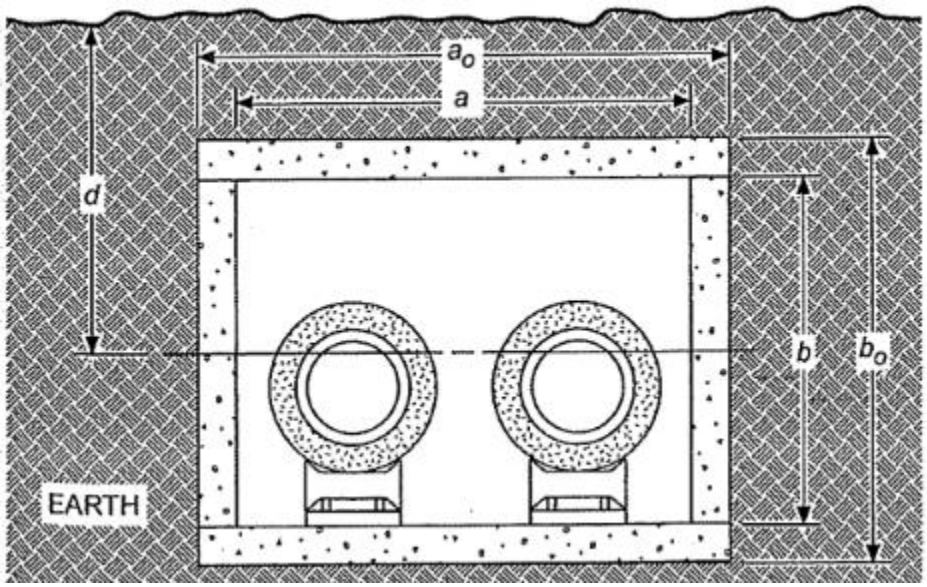

Figure 54. Two pipes in buried trenches.

The thermal resistance of the soil surrounding the trench is

$$R_{ts} = \frac{\ln[3.5d/(b_o^{0.75}a_o^{0.25})]}{k_s[(a_o/2b_o) + 5.7]} = \frac{\ln[3.5 \cdot 4ft/(3ft^{0.75}4ft^{0.25})]}{0.5Btu/hr \cdot ft \cdot °F[(4/2 \cdot 3) + 5.7]} = 0.461 \text{ hr} \cdot \text{ft} \cdot °F/Btu \quad (158)$$

where R_{ts} is the thermal resistance of soil surrounding trench, $hr \cdot ft \cdot °F/Btu$; a_o is the width of trench outside, ft; b_o is the height of trench outside, ft; d is the burial depth of trench to the centerline, ft.

Assume the thermal resistance of the air/trench wall surface is neglected; then total thermal resistance on the soil side of the air space is

$$R_{SS} = R_w + R_{ts} = (0.217 + 0.461) \text{ hr} \cdot \text{ft} \cdot °F/Btu = 0.679 \text{ hr} \cdot \text{ft} \cdot °F/Btu \quad (159)$$

A.4 Distribution Heat Loss

The total heat loss from the trench is

$$q = \frac{(t_{p1} - t_s)/R_1 + (t_{p2} - t_s)/R_2}{1 + (R_{SS}/R_1) + (R_{SS}/R_2)} = \frac{(150 - 70)/7.3 + (130 - 70)/6.9}{1 + (0.679/7.3) + (0.679/6.9)} = 16.5 \text{ Btu/hr} \cdot \text{ft} \quad (160)$$

where q is the total heat loss, t_{p1}, t_{p2}, and t_s are the temperature of fluid supply, return, and soil temperature, respectively.

APPENDIX B

MATLAB CODE

B.1 Well Pipeline Heat Transfer

```
% The code before are used to solve the ordinary
differential equation in Equation (43) with two given
boundary conditions in Equation (44) and (45).
syms y(x)
Dy = diff(y);
ode = 0.051054*diff(y,x,2)+91091.79648*diff(y)+5.7626*y == 2*42/1158*x+2*62-
2*42/1158*1219; % refer to Equation (43).
cond1 = y(-2377) == 104; % refer to Equation (44).
cond2 = Dy(-2377) == 0; % refer to Equation (45).
conds = [cond1 cond2];
ySol(x) = dsolve(ode,conds);
ySol = vpa(ySol)


ySol(x) =


0.012587870076636751293718347126342*x +
281.11401852613815889878766421557*exp(-
```

0.000063261459570286854970986116675948*x) -

192.808206296463098631873457654 88

ySol = simplify(ySol)

ySol(x) =

(70000*x)/5560909 +

(2810558229804662580 6041*exp((524288*(2449053313591397330966307839081739

3^(1/2) - 156494514726195175)*(x +

2377))/9197071015030 9325))/172041863242876715008 +

(1466123154213333181924544504876417350725*2449053313591397330966307839

0817393^(1/2)*exp((524288*(2449053313591397330966307839 0817393^(1/2) -

156494514726195175)*(x +

2377))/9197071015030 9325))/1404465650838017470924023511269074 802449892734

610178048 - exp(-(524288*(2449053313591397330966307839 0817393^(1/2) +

156494514726195175)*(x +

2377))/9197071015030 9325)*((1466123154213333181924544504876417350725*2449

053313591397330966307839 0817393^(1/2))/1404465650838017470924023511269074

802449892734610178048 - 2810558229804662580 6041/172041863242876715008) -

165855415298802327856 25/86020931621438357504

```
>> x=0;
>> 0.012587870076636751293718347126342*x +
281.11401852613815889878766421557*exp(-
0.000063261459570286854970986116675948*x) -
192.80820629646309863187345765488

ans =

88.3058
```

B.2 Desiccant Wheel with IEC-DEC

```
% Refer to Figure 22.
function F = myF(x)

b=x(1); % Temperature in state 2.
h=x(2); % Temperature in state 12.
j=x(3); % Humidity ratio in state 2.
p=x(4); % Humidity ratio in state 12.
c=x(5); % Temperature in state 4.
d=x(6); % Temperature in state 5.
s=x(7); % Humidity ratio in state 4.
m=x(8); % Humidity ratio in state 5.
```

```
w=x(9); % Wet bulb temperature in state 5.
r=x(10); % Saturation vapor pressure in state 5.
q=x(11); % Temperature in state 6.
n=x(12); % Humidity ratio in state 6.
t=x(13); % Humidity ratio corresponding to the saturation
in state 5.

global g % Temperature in state 11.
global o % Humidity ratio in state 11.
global a % Temperature in state 1.
global i % Humidity ratio in state 1.
global e % Humidity ratio in state 8.


F(1)=((-2865*b^(-1.49)+4.344*j^0.8624)-(-2865*a^(-
1.49)+4.344*i^0.8624))/((-2865*g^(-1.49)+4.344*o^0.8624)-(-
2865*a^(-1.49)+4.344*i^0.8624))-0.3; % refer to Equation
(8).
F(2)=((b^1.49/6360-1.127*j^0.07969)- (a^1.49/6360-
1.127*i^0.07969))/ ((g^1.49/6360-1.127*o^0.07969)-
(a^1.49/6360-1.127*i^0.07969))-0.85; % refer to Equation
(9).
```

```
F(3)=0.24*((a-273.15)*1.8+32)+i*(1061+0.444*((a-
273.15)*1.8+32))-(0.24*((b-
273.15)*1.8+32)+j*(1061+0.444*((b-
273.15)*1.8+32)))+(0.24*((g-
273.15)*1.8+32)+o*(1061+0.444*((g-273.15)*1.8+32)))-
(0.24*((h-273.15)*1.8+32)+p*(1061+0.444*((h-
273.15)*1.8+32))); % refer to Equation (76).
F(4)=i-j-p+o; % refer to Equation (77).
F(5)=0.15*c+0.85*e-d; % refer to Equation (80).
F(6)=0.63*(b-e)-(b-c); % refer to Equation (82).
F(7)=0.15*s+0.85*0.01-m; % refer to Equation (81).
F(8)=j-s; % refer to Equation (84).
F(9)=(2501-2.326*(w-273.15))*t-1.006*(d-w)-(2501+1.86*(d-
273.15)-4.186*(w-273.15))*m; % refer to Equation (86).
F(10)=t-0.621945*r/(101325-r); % refer to Equation (87).
F(11)=-5800.2206/w+1.3914993-
0.048640239*w+0.000041764768*w^2-
0.000000014452093*w^3+6.5459673*log(w)-log(r); % refer to
Equation (88).
F(12)=0.9*(d-w)-(d-q);
F(13)=0.9*(m-t)-(m-n);
```

```
end

global g
global o
global a
global i
global e

g=333.15;
a_s=[273.15;275.9278;278.7056;281.4833;284.2611;287.0389;28
9.8167;292.5944;295.3722;298.15;300.9278;303.7056;306.4833;
309.2611;312.0389];
e=297.039;
i_s=[0.002465;0.003347;0.004179;0.00502;0.005853;0.007302;0
.008768;0.011119;0.012967;0.015841;0.016093;0.015569;0.0158
61;0.014418;0.01228];
o_s=[0.002465;0.003347;0.004179;0.00502;0.005853;0.007302;0
.008768;0.011119;0.012967;0.015841;0.016093;0.015569;0.0158
61;0.014418;0.01228];

x_M=[];
for k = 1:15
```

```
    a=a_s(k);
    i=i_s(k);
    o=o_s(k);
    fun = @myF;
    x0 =
[300,300,0.0001,0.0001,300,300,0.0001,0.0001,280,10000,300,
0.0001,0.0001];
    x = fsolve(fun,x0);
    x_M=[x_M; x];
end

format long
xfile='ResultDEHwithIEC-DEC.csv';
xlswrite(xfile,abs(x_M))
```

B.3 Desiccant Wheel with HX

B.3.1 Code for AHU Configuration

```
% Refer to Figure 25.
function F = myF(x)

b=x(1); % Temperature in state 2.
h=x(2); % Temperature in state 13.
```

```
j=x(3); % Humidity ratio in state 2.

p=x(4); % Humidity ratio in state 13.

c=x(5); % Temperature in state 4.

f=x(6); % Temperature in state 11.

k=x(7); % Humidity ratio in state 4.


global g % Temperature in state 12.

global o % Humidity ratio in state 12.

global a % Temperature in state 1.

global i % Humidity ratio in state 1.

global e % Temperature in state 10.


F(1)=((-2865*b^(-1.49)+4.344*j^0.8624)-(-2865*a^(-

1.49)+4.344*i^0.8624))/((-2865*g^(-1.49)+4.344*o^0.8624)-(-

2865*a^(-1.49)+4.344*i^0.8624))-0.3;

F(2)=((b^1.49/6360-1.127*j^0.07969)- (a^1.49/6360-

1.127*i^0.07969))/ ((g^1.49/6360-1.127*o^0.07969)-

(a^1.49/6360-1.127*i^0.07969))-0.85;

F(3)=0.24*((a-273.15)*1.8+32)+i*(1061+0.444*((a-

273.15)*1.8+32))-(0.24*((b-

273.15)*1.8+32)+j*(1061+0.444*((b-273.15)*1.8+32)))-

(0.24*((g-273.15)*1.8+32)+o*(1061+0.444*((g-
```

```
273.15)*1.8+32)))+(0.24*((h-
273.15)*1.8+32)+p*(1061+0.444*((h-273.15)*1.8+32)));
F(4)=i-j+p-o;
F(5)=(b-c)-0.8*(b-e);
F(6)=(e-f)-0.8*(e-b);
F(7)=j-k;

end

global g
global o
global a
global i
global e

g=333.15;

a_s=[273.15;275.9278;278.7056;281.4833;284.2611;287.0389;28
9.8167;292.5944;295.3722;298.15;300.9278;303.7056;306.4833;
309.2611;312.0389];
```

```
e=[273.15;275.9278;278.7056;281.4833;284.2611;287.0389;289.
8167;292.5944;295.3722;298.15;300.9278;303.7056;306.4833;30
9.2611;312.0389];
i_s=[0.002465;0.003347;0.004179;0.00502;0.005853;0.007302;0
.008768;0.011119;0.012967;0.015841;0.016093;0.015569;0.0158
61;0.014418;0.01228];
o_s=[0.002465;0.003347;0.004179;0.00502;0.005853;0.007302;0
.008768;0.011119;0.012967;0.015841;0.016093;0.015569;0.0158
61;0.014418;0.01228];

x_M=[];
for k = 1:15
    a=a_s(k);
    i=i_s(k);
    o=o_s(k);
    e=e_s(k);
    fun = @myF;
    x0 = [300,300,0.0001,0.0001,300,300,0.0001];
    x = fsolve(fun,x0);
    x_M=[x_M; x];
end
```

```
format long

xfile='ResultDEHwithHR-AHU.csv';

xlswrite(xfile,abs(x_M))
```

B.3.2 Code for DOAS Configuration

```
% Refer to Figure 26.

function F = myF(x)


b=x(1);

h=x(2);

j=x(3);

p=x(4);

c=x(5);

f=x(6);

k=x(7);


global g

global o

global a

global i

global e
```

```
F(1)=((-2865*b^(-1.49)+4.344*j^0.8624)-(-2865*a^(-
1.49)+4.344*i^0.8624))/((-2865*g^(-1.49)+4.344*o^0.8624)-(-
2865*a^(-1.49)+4.344*i^0.8624))-0.3;
F(2)=((b^1.49/6360-1.127*j^0.07969)- (a^1.49/6360-
1.127*i^0.07969))/ ((g^1.49/6360-1.127*o^0.07969)-
(a^1.49/6360-1.127*i^0.07969))-0.85;
F(3)=0.24*((a-273.15)*1.8+32)+i*(1061+0.444*((a-
273.15)*1.8+32))-(0.24*((b-
273.15)*1.8+32)+j*(1061+0.444*((b-273.15)*1.8+32)))-
(0.24*((g-273.15)*1.8+32)+o*(1061+0.444*((g-
273.15)*1.8+32)))+(0.24*((h-
273.15)*1.8+32)+p*(1061+0.444*((h-273.15)*1.8+32)));
F(4)=i-j+p-o;
F(5)=(b-c)-0.8*(b-e); % refer to Equation (93).
F(6)=(e-f)-0.8*(e-b);
F(7)=j-k;

end

global g
global o
global a
```

```
global i
global e

g=333.15;
e=297.039;
o=0.01;

a_s=[273.15;275.9278;278.7056;281.4833;284.2611;287.0389;28
9.8167;292.5944;295.3722;298.15;300.9278;303.7056;306.4833;
309.2611;312.0389];
i_s=[0.002465;0.003347;0.004179;0.00502;0.005853;0.007302;0
.008768;0.011119;0.012967;0.015841;0.016093;0.015569;0.0158
61;0.014418;0.01228];

x_M=[];
for k = 1:15
    a=a_s(k);
    i=i_s(k);
    fun = @myF;
    x0 = [300,300,0.0001,0.0001,300,300,0.0001];
    x = fsolve(fun,x0);
    x_M=[x_M; x];
```

```
end


format long
xfile='ResultDEHwithHR-DOAS.csv';
xlswrite(xfile,abs(x_M))
```

B.4 Desiccant Wheel with CW Cooling

```
% Refer to Figure 28.
function F = myF(x)


b=x(1); % Temperature in state 2.
h=x(2); % Temperature in state 9.
j=x(3); % Humidity ratio in state 2.
p=x(4); % Humidity ratio in state 9.
c=x(5); % Temperature in state 4.
k=x(6); % Humidity ratio in state 4.


global g
global o
global a
global i
global e
```

```
F(1)=((-2865*b^(-1.49)+4.344*j^0.8624)-(-2865*a^(-
1.49)+4.344*i^0.8624))/((-2865*g^(-1.49)+4.344*o^0.8624)-(-
2865*a^(-1.49)+4.344*i^0.8624))-0.3;
F(2)=((b^1.49/6360-1.127*j^0.07969)- (a^1.49/6360-
1.127*i^0.07969))/ ((g^1.49/6360-1.127*o^0.07969)-
(a^1.49/6360-1.127*i^0.07969))-0.85;
F(3)=0.24*((a-273.15)*1.8+32)+i*(1061+0.444*((a-
273.15)*1.8+32))-(0.24*((b-
273.15)*1.8+32)+j*(1061+0.444*((b-273.15)*1.8+32)))-
(0.24*((g-273.15)*1.8+32)+o*(1061+0.444*((g-
273.15)*1.8+32)))+(0.24*((h-
273.15)*1.8+32)+p*(1061+0.444*((h-273.15)*1.8+32)));
F(4)=i-j+p-o;
F(5)=(b-c)-0.87*(b-e); % refer to Equation (96).
F(6)=j-k;

end

global g
global o
global a
global i
```

```
global e

g=333.15;
e=297.039;
o=0.01;

a_s=[273.15;275.9278;278.7056;281.4833;284.2611;287.0389;28
9.8167;292.5944;295.3722;298.15;300.9278;303.7056;306.4833;
309.2611;312.0389];
i_s=[0.002465;0.003347;0.004179;0.00502;0.005853;0.007302;0
.008768;0.011119;0.012967;0.015841;0.016093;0.015569;0.0158
61;0.014418;0.01228];
x_M=[];
for k = 1:15
    a=a_s(k);
    i=i_s(k);
    o=o_s(k);
    e=e_s(k);
    fun = @myF;
    x0 = [300,300,0.0001,0.0001,300,0.0001];
    x = fsolve(fun,x0);
    x_M=[x_M; x];
```

```
end


format long

abs(x_M)

xfile='ResultDEHwithCW DOAS.csv';

xlswrite(xfile,abs(x_M))
```

B.5 Desiccant Wheel with HX and CW Cooling

```
% Refer to Figure 30.

function F = myF(x)


b=x(1); % Temperature in state 2.

h=x(2); % Temperature in state 11.

j=x(3); % Humidity ratio in state 2.

p=x(4); % Humidity ratio in state 11.

c=x(5); % Temperature in state 4.

f=x(6); % Temperature in state 9.

k=x(7); % Humidity ratio in state 4.

d=x(8); % Temperature in state 5.

l=x(9); % Humidity ratio in state 5.


global g

global o
```

```
global a
global i
global e
global q % Temperature in state 14.

F(1)=((-2865*b^(-1.49)+4.344*j^0.8624)-(-2865*a^(-
1.49)+4.344*i^0.8624))/((-2865*g^(-1.49)+4.344*o^0.8624)-(-
2865*a^(-1.49)+4.344*i^0.8624))-0.3;
F(2)=((b^1.49/6360-1.127*j^0.07969)- (a^1.49/6360-
1.127*i^0.07969))/ ((g^1.49/6360-1.127*o^0.07969)-
(a^1.49/6360-1.127*i^0.07969))-0.85;
F(3)=0.24*((a-273.15)*1.8+32)+i*(1061+0.444*((a-
273.15)*1.8+32))-(0.24*((b-
273.15)*1.8+32)+j*(1061+0.444*((b-273.15)*1.8+32)))-
(0.24*((g-273.15)*1.8+32)+o*(1061+0.444*((g-
273.15)*1.8+32)))+(0.24*((h-
273.15)*1.8+32)+p*(1061+0.444*((h-273.15)*1.8+32)));
F(4)=i-j+p-o;
F(5)=(b-c)-0.8*(b-e);
F(6)=(e-f)-0.8*(e-b);
F(7)=j-k;
F(8)=k-l;
```

```
F(9)=(c-d)-0.87*(c-q);

end

global g
global o
global a
global i
global e
global q

g=333.15;

e=297.039;
o=0.01;

a_s=[273.15;275.9278;278.7056;281.4833;284.2611;287.0389;28
9.8167;292.5944;295.3722;298.15;300.9278;303.7056;306.4833;
309.2611;312.0389];
i_s=[0.002465;0.003347;0.004179;0.00502;0.005853;0.007302;0
.008768;0.011119;0.012967;0.015841;0.016093;0.015569;0.0158
61;0.014418;0.01228];
```

```
a_s=[273.72;276.44;279.34;281.8;284.51;287.36;290.15;293;29
5.71;298.34;301.1;303.92;306.63;309.1;311.08];
e_s=[273.72;276.44;279.34;281.8;284.51;287.36;290.15;293;29
5.71;298.34;301.1;303.92;306.63;309.1;311.08];
i_s=[0.00309;0.00352;0.00426;0.005;0.00583;0.00684;0.00915;
0.01099;0.01314;0.01587;0.01601;0.01579;0.01552;0.01546;0.0
1548];
o_s=[0.00309;0.00352;0.00426;0.005;0.00583;0.00684;0.00915;
0.01099;0.01314;0.01587;0.01601;0.01579;0.01552;0.01546;0.0
1548];
q_s=[291.4833;291.4833;291.4833;291.4833;291.4833;291.4833;
293.26;297.0458;297.5259;300.3223;301.8427;302.1856;302.053
6;301.7368;302.2537];

x_M=[];
for k = 1:15
    a=a_s(k);
    i=i_s(k);
    o=o_s(k);
    e=e_s(k);
    q=q_s(k);
```

```
    fun = @myF;
    x0 = [300,300,0.0001,0.0001,300,300,0.0001,300,0.0001];
    x = fsolve(fun,x0);
    x_M=[x_M; x];
end

format long
abs(x_M)
xfile='ResultDEHwithHXCW DOAS.csv';
xlswrite(xfile,abs(x_M))
```

APPENDIX C

ABSORPTION CHILLER OPERATIONAL DATA UNDER DIFFERENT TEMPERATURE CONDITIONS

A 12kW cooling capacity single-effect ammonia-water absorption chiller prototype was developed by Joanneum Research in cooperation with the company Pink GmbH in Austria and a comprehensive set of operational data were recorded in Dr. Jerko Labus's dissertation [131]. The detailed data sets are listed in Table 34.

Table 34. Summary of the operation for absorption chiller Pink chilli 12 under different temperature conditions.

No.	$T_{chw,in}$	$T_{chw,out}$	V_{chw}	$T_{cw,in}$	$T_{cw,out}$	V_{cw}	$T_{hw,in}$	$T_{hw,ou}$	V_{hw}	Q_{eva}	Q_{ac}	Q_{gen}	$COP_{chiller,th}$
	°C	°C	m^3/h	°C	°C	m^3/h	°C	°C	m^3/h	kW	kW	kW	kW
1	8.66	5.04	1.72	27	30.84	4.75	80.01	75	2.24	7.26	21.11	12.72	0.57
2	9.94	5.99	1.72	27	31.06	4.76	79.97	74.77	2.24	7.92	22.34	13.2	0.6
3	11.26	7.01	1.72	27.02	31.18	4.78	79.99	74.68	2.24	8.5	23.04	13.49	0.63
4	12.5	7.86	1.72	27	31.48	4.78	80	74.38	2.24	9.27	24.81	14.26	0.65
5	14.12	8.97	1.72	27.02	31.75	4.78	79.98	74.19	2.24	10.29	26.11	14.7	0.7
6	15.41	9.99	1.72	27.03	31.93	4.77	79.97	74.05	2.24	10.83	27.04	15.05	0.72
7	16.59	10.95	1.72	27.02	32.11	4.77	79.98	73.89	2.24	11.28	28.08	15.46	0.73
8	7.01	4.98	1.72	30	32.46	4.75	79.99	76.73	2.24	4.07	13.53	8.28	0.49
9	8.36	6.02	1.72	29.99	32.65	4.76	80	76.59	2.24	4.7	14.6	8.65	0.54
10	9.66	7.04	1.72	29.99	32.79	4.76	80	76.44	2.24	5.23	15.42	9.03	0.58
11	10.95	8.02	1.72	30	32.95	4.76	80	76.33	2.24	5.88	16.23	9.33	0.63
12	12.25	9.03	1.72	30	33.1	4.76	79.99	76.18	2.24	6.43	17.11	9.65	0.67
13	13.88	10.03	1.72	30	33.52	4.76	80.01	75.82	2.24	7.69	19.37	10.65	0.72
14	15.16	11.01	1.72	30.01	33.67	4.76	80	75.7	2.24	8.29	20.15	10.92	0.76
15	16.37	12.07	1.72	29.99	33.8	4.77	80	75.58	2.24	8.59	20.97	11.24	0.76
16	5.52	5	1.72	33	34.23	4.8	80	77.99	2.24	1.05	6.82	5.11	0.21

Table 34 (Continued).

No.	$T_{chw,in}$	$T_{chw,out}$	V_{chw}	$T_{cw,in}$	$T_{cw,out}$	V_{cw}	$T_{hw,in}$	$T_{hw,ou}$	V_{hw}	Q_{eva}	Q_{ac}	Q_{gen}	$COP_{chiller,th}$
	°C	°C	m^3/h	°C	°C	m^3/h	°C	°C	m^3/h	kW	kW	kW	kW
17	6.82	6.01	1.72	32.98	34.48	4.8	80.02	77.8	2.24	1.63	8.27	5.65	0.29
18	8.09	6.99	1.72	33	34.66	4.8	79.99	77.59	2.24	2.22	9.18	6.07	0.36
19	9.27	7.98	1.72	33	34.7	4.79	79.9	77.59	2.24	2.59	9.39	5.87	0.44
20	10.92	9.07	1.72	33.02	34.97	4.78	79.94	77.41	2.24	3.7	10.76	6.43	0.58
21	12.2	10.06	1.72	33.01	35.09	4.79	80	77.35	2.24	4.27	11.55	6.73	0.63
22	6.29	6.04	1.72	35	36.08	4.79	80	78.17	2.24	0.49	5.99	4.64	0.11
23	7.39	6.98	1.72	35	36.17	4.79	80.01	78.1	2.24	0.83	6.5	4.83	0.17
24	8.5	8.01	1.72	34.99	36.2	4.79	80.02	78.07	2.24	0.99	6.69	4.95	0.2
25	9.65	8.99	1.72	35	36.31	4.79	80	77.95	2.24	1.33	7.23	5.2	0.26
26	10.8	9.89	1.72	34.99	36.49	4.79	79.94	77.82	2.24	1.83	8.29	5.38	0.34
27	9.15	5	1.71	27	31.38	4.78	84.99	79.09	2.23	8.28	24.19	14.85	0.56
28	10.45	5.98	1.72	27	31.55	4.78	85	79.01	2.23	8.95	25.15	15.09	0.59
29	12.03	7.02	1.72	27	31.82	4.78	84.99	78.84	2.24	10.03	26.62	15.6	0.64
30	13.23	8	1.72	26.98	31.91	4.78	84.98	78.81	2.24	10.46	27.21	15.64	0.67
31	14.44	9.01	1.72	27.04	32.24	4.78	84.99	78.62	2.24	10.84	28.79	16.16	0.67
32	15.75	10	1.72	27.07	32.29	4.78	85.03	78.39	2.24	11.49	28.87	16.83	0.68
33	17.04	11.01	1.72	27.05	32.45	4.77	85.02	78.27	2.24	12.03	29.77	17.11	0.7
34	8	5.04	1.73	30	33.38	4.76	85.01	80.38	2.24	5.96	18.66	11.73	0.51
35	9.22	6.04	1.71	30	33.5	4.77	84.99	80.29	2.23	6.34	19.3	11.87	0.53
36	10.65	6.99	1.72	30	33.79	4.77	84.98	79.94	2.24	7.33	20.94	12.76	0.57
37	11.97	7.98	1.73	30	34.05	4.77	85.01	79.65	2.24	8.03	22.29	13.54	0.59
38	13.1	8.99	1.74	30	34.1	4.77	84.98	79.62	2.24	8.31	22.58	13.59	0.61
39	14.39	10.01	1.74	30	34.22	4.77	85.03	79.67	2.24	8.85	23.28	13.58	0.65
40	15.71	10.98	1.72	29.99	34.41	4.77	85	79.41	2.24	9.45	24.36	14.13	0.67
41	17	12	1.72	29.98	34.59	4.77	84.97	79.23	2.23	9.99	25.41	14.5	0.69
42	6.47	5.03	1.72	33	35.04	4.79	85.01	81.88	2.24	2.89	11.31	7.92	0.36
43	7.68	6.01	1.71	33	35.18	4.8	85.01	81.7	2.23	3.33	12.09	8.37	0.4
44	8.87	6.99	1.71	33.01	35.37	4.81	85.04	81.51	2.23	3.75	13.12	8.91	0.42

Table 34 (Continued).

No.	$T_{chw,in}$	$T_{chw,out}$	V_{chw}	$T_{cw,in}$	$T_{cw,out}$	V_{cw}	$T_{hw,in}$	$T_{hw,ou}$	V_{hw}	Q_{eva}	Q_{ac}	Q_{gen}	$COP_{chiller,th}$
	°C	°C	m^3/h	°C	°C	m^3/h	°C	°C	m^3/h	kW	kW	kW	kW
45	10.51	7.99	1.71	33.01	35.85	4.78	85.01	81.06	2.24	5	15.68	10	0.5
46	11.83	8.98	1.71	33	36.07	4.78	85	80.76	2.24	5.67	16.95	10.71	0.53
47	13.1	10.02	1.71	33	36.24	4.79	85.01	80.57	2.24	6.14	17.92	11.24	0.55
48	14.45	11.1	1.72	32.99	36.42	4.78	85	80.36	2.24	6.68	18.92	11.73	0.57
49	15.62	12.05	1.72	33	36.56	4.78	85	80.22	2.24	7.15	19.62	12.07	0.59
50	5.52	5.01	1.73	35	36.36	4.79	85.01	82.62	2.25	1.03	7.5	6.07	0.17
51	6.83	5.99	1.73	34.99	36.59	4.79	85.01	82.43	2.24	1.7	8.83	6.56	0.26
52	8.18	7.01	1.73	35	36.81	4.77	85	82.18	2.24	2.36	9.97	7.13	0.33
53	9.5	8.01	1.73	35	37.03	4.77	85	81.94	2.23	3	11.19	7.73	0.39
54	10.77	9.02	1.73	35	37.23	4.77	85	81.73	2.23	3.53	12.28	8.27	0.43
55	12.12	10.02	1.73	35	37.43	4.77	85	81.53	2.23	4.25	13.36	8.75	0.49
56	13.4	11.04	1.73	35	37.61	4.76	84.99	81.36	2.23	4.76	14.35	9.18	0.52
57	14.6	12.03	1.73	35	37.8	4.75	85	81.16	2.23	5.15	15.38	9.7	0.53
58	9.96	5.01	1.72	27.02	32.04	4.76	90.04	83.39	2.24	9.92	27.67	16.82	0.59
59	11.17	6.04	1.72	26.99	32.2	4.75	90.04	83.23	2.24	10.26	28.63	17.22	0.6
60	12.58	7	1.72	27	32.42	4.75	90.04	83.05	2.24	11.17	29.75	17.66	0.63
61	13.89	7.93	1.72	27.05	32.61	4.75	90.04	82.92	2.24	11.91	30.52	18.02	0.66
62	15.28	8.99	1.72	27	32.88	4.75	89.99	82.68	2.24	12.56	32.27	18.48	0.68
63	16.51	9.96	1.72	26.95	32.98	4.75	90.04	82.67	2.24	13.09	33.13	18.66	0.7
64	17.78	11.02	1.72	27.02	33.1	4.75	90.07	82.54	2.24	13.52	33.41	19.03	0.71
65	8.73	5	1.72	30	33.92	4.76	90.01	84.81	2.24	7.47	21.53	13.12	0.57
66	10.08	6.02	1.72	30	34.13	4.76	90	84.6	2.24	8.13	22.75	13.64	0.6
67	11.41	7.01	1.72	30.01	34.31	4.76	90.01	84.46	2.24	8.81	23.72	14.03	0.63
68	13.06	7.99	1.72	30.01	34.79	4.77	90	83.95	2.24	10.13	26.38	15.3	0.66
69	14.4	9	1.72	30.02	34.95	4.77	90.01	83.88	2.24	10.8	27.17	15.51	0.7
70	15.67	10.01	1.72	30.01	35.09	4.78	90.02	83.72	2.24	11.3	28.06	15.93	0.71
71	16.83	10.93	1.72	30	35.19	4.79	90.02	83.66	2.24	11.79	28.75	16.09	0.73
72	7.62	5.03	1.72	33	35.99	4.78	90	85.82	2.24	5.18	16.53	10.56	0.49

Table 34 (Continued).

No.	$T_{chw,in}$	$T_{chw,out}$	V_{chw}	$T_{cw,in}$	$T_{cw,out}$	V_{cw}	$T_{hw,in}$	$T_{hw,ou}$	V_{hw}	Q_{eva}	Q_{ac}	Q_{gen}	$COP_{chiller,th}$
	°C	°C	m^3/h	°C	°C	m^3/h	°C	°C	m^3/h	kW	kW	kW	kW
73	8.92	6.02	1.72	33	36.18	4.78	90	85.65	2.24	5.82	17.56	10.98	0.53
74	10.32	7.01	1.72	33	36.39	4.78	90	85.5	2.24	6.62	18.74	11.39	0.58
75	11.71	8.01	1.72	32.99	36.66	4.78	90	85.22	2.24	7.4	20.26	12.09	0.61
76	13.01	9.02	1.72	33.01	36.77	4.79	90	85.16	2.24	7.97	20.81	12.26	0.65
77	14.14	10.04	1.72	32.99	37.03	4.76	90	84.82	2.24	8.21	22.17	13.11	0.63
78	15.45	11.05	1.72	33	37.21	4.76	89.99	84.65	2.24	8.78	23.12	13.5	0.65
79	16.62	12.05	1.72	33	37.25	4.79	90	84.61	2.24	9.13	23.51	13.64	0.67
80	6.4	4.98	1.72	35	37.21	4.78	90	86.57	2.24	2.84	12.19	8.67	0.33
81	7.77	6.05	1.72	35	37.43	4.78	89.99	86.36	2.24	3.46	13.41	9.18	0.38
82	9.07	7	1.72	35	37.66	4.79	90.01	86.11	2.24	4.14	14.66	9.86	0.42
83	10.42	8.02	1.72	35	37.86	4.78	89.99	85.91	2.24	4.81	15.8	10.33	0.47
84	11.72	9.04	1.72	35	38.09	4.78	89.99	85.64	2.24	5.37	17.08	11	0.49
85	13.04	10.04	1.72	35	38.32	4.78	89.98	85.39	2.24	6	18.3	11.6	0.52
86	14.32	10.99	1.72	35	38.52	4.78	90	85.2	2.24	6.65	19.39	12.11	0.55
87	15.66	12.1	1.72	34.99	38.72	4.77	89.99	85.03	2.24	7.12	20.51	12.53	0.57
88	10.8	5.05	1.72	27.01	33.01	4.75	95.03	87.31	2.24	11.52	32.97	19.48	0.59
89	11.94	6.01	1.72	27.01	33.2	4.77	95.07	87.06	2.24	11.86	34.14	20.24	0.59
90	13.37	6.98	1.72	27.05	33.32	4.78	95.06	86.94	2.24	12.79	34.68	20.52	0.62
91	14.74	8.03	1.72	27.03	33.55	4.78	95.05	86.75	2.24	13.42	36.03	20.94	0.64
92	16.02	8.99	1.72	26.99	33.73	4.78	95.04	86.57	2.24	14.04	37.24	21.38	0.66
93	17.38	10.02	1.72	27.05	33.99	4.78	95.02	86.51	2.24	14.69	38.41	21.48	0.68
94	9.22	5	1.72	30	34.83	4.76	95.05	88.33	2.24	8.46	26.56	16.96	0.5
95	10.66	5.99	1.72	30.01	35.1	4.76	95.03	88.16	2.24	9.35	28	17.34	0.54
96	12.08	7.01	1.72	30.01	35.42	4.76	95.05	87.81	2.24	10.13	29.71	18.27	0.55
97	13.78	7.99	1.72	30	35.48	4.76	95.04	88.21	2.24	11.57	30.11	17.24	0.67
98	14.69	9.01	1.72	30	35.68	4.76	95.07	87.71	2.24	11.36	31.23	18.56	0.61
99	16.05	9.98	1.72	30.03	35.92	4.76	95.03	87.43	2.24	12.12	32.39	19.19	0.63
100	17.27	11.01	1.72	30.03	36.1	4.75	95.07	87.27	2.24	12.52	33.4	19.71	0.64

Table 34 (Continued).

No.	$T_{chw,in}$	$T_{chw,out}$	V_{chw}	$T_{cw,in}$	$T_{cw,out}$	V_{cw}	$T_{hw,in}$	$T_{hw,ou}$	V_{hw}	Q_{eva}	Q_{ac}	Q_{gen}	$COP_{chiller,th}$
	°C	°C	m^3/h	°C	°C	m^3/h	°C	°C	m^3/h	kW	kW	kW	kW
101	7.81	5	1.72	33	36.71	4.77	95	89.53	2.24	5.63	20.41	13.8	0.41
102	9.41	6	1.72	33	37.01	4.77	95.01	89.38	2.24	6.82	22.08	14.21	0.48
103	10.8	7	1.72	33	37.25	4.77	95	89.14	2.24	7.59	23.41	14.77	0.51
104	12.08	8	1.72	33	37.48	4.76	95.01	88.87	2.24	8.16	24.63	15.5	0.53
105	13.49	9	1.72	33.01	37.72	4.77	95.01	88.63	2.24	8.97	25.94	16.12	0.56
106	14.72	10	1.72	33	37.91	4.77	95.02	88.42	2.24	9.43	27.01	16.66	0.57
107	16.12	11	1.72	33	38.14	4.76	95.04	88.26	2.24	10.23	28.26	17.12	0.6
108	17.21	11.92	1.72	32.99	38.31	4.76	95.04	88.11	2.24	10.58	29.29	17.5	0.6
109	7.42	5.01	1.72	35	38.04	4.8	95	90.61	2.24	4.83	16.81	11.09	0.44
110	8.74	6.02	1.72	35	38.23	4.79	95.01	90.4	2.24	5.45	17.9	11.63	0.47
111	10.04	7.01	1.72	35	38.43	4.79	95	90.2	2.24	6.06	18.99	12.11	0.5
112	11.23	7.99	1.72	35	38.59	4.79	95	90.04	2.24	6.5	19.81	12.49	0.52
113	12.63	9	1.72	35.01	38.73	4.79	94.99	89.99	2.24	7.26	20.56	12.61	0.58
114	13.81	10.03	1.72	35	39.17	4.77	95.01	89.35	2.24	7.55	22.94	14.29	0.53
115	15.08	11.04	1.72	35	39.35	4.77	95	89.14	2.24	8.08	23.95	14.79	0.55
116	16.35	12.03	1.72	35	39.49	4.77	94.99	88.99	2.24	8.64	24.75	15.14	0.57
117	11.22	5.03	1.72	27.01	33.68	4.77	100.01	91.19	2.24	12.39	36.8	22.2	0.56
118	12.5	6.01	1.72	27.01	33.92	4.77	99.99	90.92	2.24	13	38.04	22.85	0.57
119	13.84	6.96	1.72	26.99	34.03	4.77	100.03	90.84	2.24	13.77	38.79	23.16	0.59
120	15.4	8.03	1.72	27.06	34.26	4.77	99.94	90.71	2.24	14.73	39.7	23.24	0.63
121	16.46	8.96	1.72	27.03	34.41	4.77	99.99	90.58	2.24	14.99	40.67	23.71	0.63
122	17.19	9.57	1.72	26.95	34.57	4.77	99.93	90.39	2.24	15.23	41.98	24.04	0.63
123	10.2	5	1.72	30	35.43	4.76	100.05	93.01	2.24	10.42	29.88	17.74	0.59
124	11.25	6	1.72	30	35.51	4.76	100.06	92.86	2.24	10.5	30.27	18.13	0.58
125	12.7	6.99	1.72	30	35.85	4.76	100.07	92.51	2.24	11.42	32.21	19.05	0.6
126	14.1	7.96	1.72	29.99	36.13	4.76	100.12	92.25	2.24	12.26	33.76	19.84	0.62
127	15.75	9.03	1.72	30.04	36.47	4.77	100.07	92.01	2.24	13.44	35.43	20.31	0.66
128	16.67	9.83	1.72	29.93	36.58	4.76	100.11	91.98	2.24	13.67	36.58	20.48	0.67

Table 34 (Continued).

No.	$T_{chw,in}$	$T_{chw,out}$	V_{chw}	$T_{cw,in}$	$T_{cw,out}$	V_{cw}	$T_{hw,in}$	$T_{hw,ou}$	V_{hw}	Q_{eva}	Q_{ac}	Q_{gen}	$COP_{chiller,th}$
	°C	°C	m^3/h	°C	°C	m^3/h	°C	°C	m^3/h	kW	kW	kW	kW
129	8.71	5.01	1.72	32.99	37.4	4.76	100.03	93.81	2.24	7.42	24.23	15.65	0.47
130	10.11	6	1.72	33	37.74	4.76	100.05	93.44	2.24	8.23	26.08	16.63	0.49
131	11.64	7.03	1.72	33	38	4.77	100.06	93.27	2.24	9.23	27.49	17.09	0.54
132	12.94	8.01	1.72	33	38.17	4.76	100.04	93.15	2.24	9.87	28.39	17.36	0.57
133	14.23	8.99	1.72	33	38.41	4.76	100.09	92.9	2.24	10.46	29.73	18.12	0.58
134	15.63	9.99	1.72	33	38.55	4.77	100.01	92.85	2.24	11.26	30.53	18.04	0.62
135	8.1	5	1.72	35	38.77	4.77	100.01	94.6	2.24	6.2	20.73	13.63	0.46
136	9.62	6.03	1.72	35	39.05	4.77	100.01	94.43	2.24	7.18	22.29	14.05	0.51
137	10.96	7.04	1.72	35	39.28	4.76	100	94.19	2.24	7.84	23.5	14.62	0.54
138	12.18	7.99	1.72	35	39.47	4.76	100.02	93.97	2.24	8.37	24.55	15.23	0.55